

Novel Anodized Metal Oxide Nanostructures on Non-Native Substrates

by

Ryan Kisslinger

A thesis submitted in partial fulfillment of the requirements for the degree of

Doctor of Philosophy

in

Microsystems and Nanodevices

Department of Electrical and Computer Engineering
University of Alberta

© Ryan Kisslinger, 2020

Abstract

Anodized metal-oxide nanostructures are of interest in a wide variety of applications, such as in solar energy harvesting, sensing, antifouling, and biomedical coatings. Anodization is a solution-processable method and presents a viable route to large-scale manufacturing of ordered nanostructures for real-world applications. Many devices require the nanostructured film to be fabricated on non-native substrates, which is typically produced by anodizing metal films deposited by vapour deposition processes; however, such configurations have received only a fraction of the attention that anodization of metal foils have. To date, studies have not sufficiently investigated the unique considerations inherent to anodizing on non-native substrates, nor fully leveraged the capabilities of anodizing to produce novel nanostructured morphologies. Thus, the purpose of this thesis is to address this knowledge gap. This is accomplished through three studies that consider TiO_2 nanotubes, NiO nanopores, and Ta_2O_5 nanodimples, respectively.

Preferentially oriented TiO_2 nanotubes are considered in the first study, and this thesis demonstrates that they may be formed on non-native substrates. It is shown that optimal electrolyte water content plays the largest role in obtaining preferential orientation of the polycrystalline grains, with an optional cation adsorption step playing a secondary role. Unlike previous reports of preferential orientation on metal foils, the roughness of the anodized substrate is found to play no role on the resulting preferential orientation; however, the material identity of the non-native substrate is found to influence preferential orientation, which may be caused by the degree of lattice mismatch between TiO_2 and the substrate. Photoconductivity characterizations and use of the preferentially oriented nanotubes in lead halide perovskite solar cells reveal that preferential orientation plays a significant role in charge trapping and charge transfer.

Nanoporous NiO is considered in the second study, and this thesis demonstrates that it may be formed on non-natives substrates after annealing the as-anodized $\text{NiO}_x(\text{OH})_y$. The relatively higher chemical etching rate of the $\text{NiO}_x(\text{OH})_y$ means that the nanostructure morphology is especially sensitive to substrate roughness, and remarkably differing morphologies are obtained across FTO-coated glass, ITO-coated glass, and Si wafer substrates. Furthermore, upon annealing, the high diffusivity between Ni and Si results in a NiSi layer. The as-produced NiO is demonstrated by electrochemical impedance spectroscopy and Mott-Schottky analysis to be p-type, with an acceptor charge carrier density of $2.85 \times 10^{18} \text{ cm}^{-3}$ and a flat band potential of 0.687 V versus Ag/AgCl.

Ta_2O_5 nanotubes formed by anodization are demonstrated in the third study, which are subsequently delaminated to leave a nanodimpled Ta surface behind. It is shown that this surface may be oxidized to form Ta_2O_5 nanodimples. The role of the key synthesis parameters including anodizing voltage and anodizing time on the pore rate, pore depth, and resultant layer thickness are investigated in-depth, as well as the effects of annealing on the nanodimpled morphology. Stable dimple formation occurs after anodization within a range of voltages from 7–40 V. The bandgap of the Ta_2O_5 is found to be 4.5 eV through EELS and UV-Vis spectroscopy. The nanodimples are demonstrated as a platform for plasmonic photocatalysis in a model reaction monitored using surface enhanced Raman spectroscopy, and an increased photooxidation rate is observed when used in tandem with Au nanoparticles. FDTD simulations indicate that a notable red-shifting of the Au nanoparticle localized surface plasmon resonance of 75 nm may be attributable to partial embedding of the Au nanoparticles in the Ta_2O_5 film.

Preface

This thesis is structured in a journal article-based format.

Chapter 2 is based off a journal article by Ryan Kisslinger, Abdelrahman M. Askar, Ujwal K. Thakur, Saralyn Riddell, Darren Dahunsi, Yun Zhang, Sheng Zeng, Ankur Goswami, and Karthik Shankar, entitled “Preferentially oriented TiO₂ nanotube arrays on non-native substrates and their improved performance as electron transporting layer in halide perovskite solar cells”, published in *Nanotechnology* **30**, 204003 (2019). I fabricated the majority of the samples, performed the majority of the experiments and characterizations, analyzed the majority of the data, and wrote the manuscript. Abdelrahman Askar performed x-ray diffraction characterizations; Ujwal K. Thakur fabricated solar cells and performed related characterizations; Saralyn Riddell and Darren Dahunsi assisted with sample fabrication; Yun Zhang, Sheng Zeng, and Ankur Goswami assisted with photoconductivity measurements; Karthik Shankar supervised the reasearch.

Chapter 3 is based off a journal article by Ryan Kisslinger, Saralyn Riddell, Spencer Savela, Piyush Kar, Ujwal K. Thakur, Sheng Zeng, and Karthik Shankar, entitled “Transparent nanoporous P-type NiO films grown directly on non-native substrates by anodization”, published in *Journal of Materials Science: Materials in Electronics* **30**, 11327-11335 (2019). I fabricated the majority of the samples, performed the majority of the experiments and characterizations, analyzed the majority of the data, and wrote the manuscript; Saralyn Riddell and Spencer Savela fabricated samples; Piyush Kar performed electrochemical impedance spectroscopy, impedance-potential measurements, and conducted related equivalent circuit modelling and data analysis; Ujwal K.

Thakur and Sheng Zeng assisted with microscopy characterizations; Karthik Shankar supervised the research.

Chapter 4 is based off a manuscript prepared for submission as a journal article with the expected author list as Ryan Kisslinger, Saralyn Riddell, Ajay Manuel, Kazi Alam, Aarat P. Kalra, Kai Cui, and Karthik Shankar, entitled “Tantalum Oxide Nanodimples Formed by Anodization as a Platform for Plasmonics”. I fabricated the majority of the samples, performed the majority of the experiments and characterizations, analyzed the majority of the data, and wrote the manuscript; Saralyn Riddell fabricated samples, and performed microscopy and characterization measurements; Kazi Alam performed Raman measurements and related photocatalytic studies; Ajay Manuel performed Lumerical simulations; Aarat P. Kalra assisted in atomic force microscopy analysis; Kai Cui collected transmission electron microscope micrographs; Karthik Shankar supervised the research.

Dedication

This thesis is dedicated to my sister Lana, whose courage and perseverance know no limits.

Acknowledgments

I would like to thank my supervisor, Dr. Karthik Shankar, whose steady mentorship crafted me from a wide-eyed undergraduate intern into the scientist I am today. I would also like to thank the members of my supervisory committee, Dr. Ken Cadien and Dr. Doug Barlage, for their helpful feedback towards the completion of this thesis.

I would like to thank the many colleagues who I worked with throughout my graduate degree and whose efforts and expertise helped make this thesis; you all make research a rich and worthwhile endeavor to do. In a loosely chronological order as we were introduced: Samira Farsinezhad, Arash Mohammadpour, Ben Wiltshire, Piyush Kar, Abdelrahman Askar, Weidi Hua, Najia Mahdi, Yun Zhang, Peng Li, Shihong Xu, Steve Launspach, Ujwal Thakur, Saralyn Riddell, Darren Dahunsi, Ankur Goswami, Sheng Zeng, Ehsan Vahidzadeh, Kai Cui, Lian Shoute, Arezoo Hosseini, Pawan Kumar, Kazi Alam, Spencer Savela, Ajay Manuel, Anqiang He, Tom Nilges, Claudia Ott, Ebru Üzer, Aarat Kalra, and many others.

I gratefully acknowledge the financial support of this work provided by the Natural Science and Engineering Research Council of Canada, Alberta Innovates Technology Futures, CMC microsystems, and the University of Alberta Faculty of Graduate Studies.

Finally, I would like to thank my many friends and family for their unwavering support through this journey. I am so grateful to have you in my life.

Table of Contents

Abstract	ii
Preface.....	iv
Dedication	vi
Acknowledgments.....	vii
Table of Contents	viii
List of Tables.....	x
List of Figures	xi
List of Symbols	xv
List of Abbreviations.....	xvii
Chapter 1: Introduction.....	1
1.1 The Energy Problem.....	2
1.2 Solar Energy Harvesting Devices	4
1.3 Nanostructured Materials	6
1.4 Metal Oxides	7
1.5 An Overview of Anodization	8
1.6 Sputtering	16
1.7 The Research Leading Up to this thesis	18
1.8 Research Questions Asked, and Thesis Organization.....	22
Chapter 2: Preferentially Oriented TiO ₂ Nanotubes.....	25
2.1 Chapter Introduction	25
2.2 Experimental Details	30
2.2.1 Sample Preparation	30
2.2.2 Material Characterization.....	31
2.2.3 Solar cell preparation and testing.....	32
2.3 Results and Discussion.....	34
2.3.1 Preferentially oriented TiO ₂ nanotube arrays on non-native substrates.....	34
2.3.2 Effect of preferred orientation on carrier transport and recombination processes in TNTAs.....	45

2.3.3	Effect of preferred orientation on the performance of halide perovskite solar cells that use TNTA electron transport layers	51
2.4	Chapter Conclusion	55
Chapter 3:	Nanoporous NiO on Non-Native Substrates.....	57
3.1	Chapter Introduction	57
3.2	Experimental Details	58
3.2.1	Sample Preparation	58
3.2.2	Characterization	60
3.3	Results and Discussion.....	61
3.3.1	Effect of Synthesis Parameters on Anodized Film Morphology	61
3.3.2	Anodized Film Characterization	66
3.3.3	Optoelectronic Characterization of NiO on FTO-Coated Glass	69
3.4	Chapter Conclusion.....	74
Chapter 4:	Ta ₂ O ₅ Nanodimples formed on non-native substrates.....	76
4.1	Chapter Introduction	76
4.2	Experimental Details.....	78
4.2.1	Sample Preparation	78
4.2.2	Characterization	79
4.3	Results and Discussion.....	82
4.3.1	Ta ₂ O ₅ Dimple Formation	82
4.3.2	Characterization of Ta ₂ O ₅ Dimples.....	91
4.3.3	Au Nanoparticle Decoration and Plasmonic Photocatalysis.....	93
4.4	Chapter Conclusion.....	101
Chapter 5:	Conclusion	103
5.1	Key Conclusions	103
5.2	Future Work	106
Bibliography.....		109

List of Tables

Table 2-1: Parameters of TNTAs obtained from steady-state and transient photoconductivity...	49
Table 2-2: Photovoltaic performance of perovskite solar cells with TNTA prepared using different electrolyte water concentrations, and with and without Zn incorporation. All parameters are shown \pm one standard deviation.	52
Table 2-3: Champion photovoltaic performance of perovskite solar cells with TNTA prepared using different electrolyte water concentrations, and with and without Zn incorporation	53

List of Figures

Figure 1-1: Global weighted average levelized cost of electricity (LCOE) from utility-scale renewable power generation technologies for 2010 and 2019.....	4
Figure 1-2: (a) A picture of an electrolytic cell used to conduct anodization, with a graphite cathode on the left and a Ti-coated piece of transparent conductive oxide-coated glass on the right. (b) A schematic of anodization.....	9
Figure 1-3: Schematic showing oxide anodization morphologies, using aluminum oxide (AAO) as an example	12
Figure 1-4: Schematic of TiO ₂ nanotube (NT) formation, and the plastic flow mechanism that leads to distinct nanotube formation as opposed to nanopores.	15
Figure 1-5: Schematic of pore formation at higher and lower voltages, where a higher voltage used leads to larger diameter pores.	16
Figure 1-6: Thornton model for sputtered metals (77).	18
Figure 2-1: Schematic diagrams of the grain structure of anodized TiO ₂ nanotubes	29
Figure 2-2: Schematic of the halide perovskite solar cell utilized in this study.	33
Figure 2-3: Macroscopic Image of TiO ₂ nanotube arrays of FTO and UV-VIS diffuse transmittance spectra	35
Figure 2-4: FESEM images of anodized TiO ₂ nanotubes.....	36
Figure 2-5: XRD patterns of TiO ₂ nanotube arrays comparing preferential orientation	40
Figure 2-6: An image of XRD system used in this study	41
Figure 2-7: Investigations comparing the relative preferential orientation of Zn-TNTA and pristine TNTA.....	42
Figure 2-8: XRD 2D frames of TiO ₂ nanotube arrays with the sample rotated at $\chi=68.3^\circ$	43

Figure 2-9: Three-dimensional AFM topographical images of sputtered Ti.....	45
Figure 2-10 (a) Experimental current-voltage curves of TNTA-1%, Zn-TNTA-1%, TNTA-4% and Zn-TNTA-4% samples under dark and 365 nm illumination and (b) Photocurrent-bias curves for the same samples.....	48
Figure 2-11: (a) Experimental current-voltage curves on Zn-TNTA-1% and TNTA-1% samples under dark and 365 nm illumination. (b) Experimental current-time curve showing photoconductive decay of Zn-TNTA-1% and TNTA-1% samples under a 2V bias.....	48
Figure 2-12: Experimental current-voltage curves of TNTA-2% and Zn-TNTA-2 % samples in the dark and in room light.....	50
Figure 2-13: Experimental current–voltage characteristics under AM1.5 G one sun illumination of perovskite solar cells.....	52
Figure 2-14: (a) Action spectra showing the external quantum efficiency (EQE) of halide perovskite solar cells constructed using TNTA-1 % samples and Zn-TNTA-1% samples as the electron transport layers and (b) Percent difference spectra of the average EQE of solar cells made using Zn-TNTA-1 % ETLs compared to the average EQE of solar cells made using TNTA-1 % ETLs.....	54
Figure 3-1: SEM images of nanoporous NiO film compared across substrates.....	64
Figure 3-2: SEM images of nanoporous NiO films on FTO Glass using alternate anodization parameters.....	65
Figure 3-3: : Three-dimensional AFM Topographical Images of sputtered Ni.....	65
Figure 3-4: XRD patterns of anodized Ni films.....	67
Figure 3-5: XPS spectra showing the Ni 2p region of anodized Ni films	68
Figure 3-6: XPS spectra showing the O 1s region of anodized Ni films.....	69

Figure 3-7: UV-Vis Spectra of NiO films on FTO-coated glass.	70
Figure 3-8: (a) Nyquist plot and (b) Bode phase plot of the NiO film on FTO. (c) is the equivalent circuit representing the Nyquist and Bode plots in (a) and (b). (d) Mott-Schottky plot of the NiO film showing the VFB and straight-line fit that was used to calculate V_{FB} and N_A	73
Figure 4-1: Schematic Illustration of the Growth of Ta ₂ O ₅ nanodimples on a quartz substrate... ..	79
Figure 4-2: SEM Images of delaminated Ta ₂ O ₅ nanotubes laying on top of Ta Dimples.....	83
Figure 4-3: SEM images of disordered porous oxides.....	83
Figure 4-4: Typical current density-time plot of Ta ₂ O ₅ nanotube anodization.	84
Figure 4-5: Ta film thicknesses as a function of anodizing time.....	86
Figure 4-6: SEM Images of Ta nanodimples. Insets shows 2D-FFT	87
Figure 4-7: (a) Compact layer anodization to convert Ta dimples to Ta ₂ O ₅ (b) Ta ₂ O ₅ as obtained by double anodization.	89
Figure 4-8: Characteristic 2D AFM Images of (a) Ta nanodimples and (b) Ta ₂ O ₅ nanodimples.	90
Figure 4-9: (a) shows the pore diameter while (b) shows the pore depth of nanodimples as a function of anodization voltage, before and after annealing.....	90
Figure 4-10: XRD patterns of (a) Ta nanodimples and (b) Ta ₂ O ₅ nanodimples. The pattern in (a) is also representative of the sputtered Ta film before further processing	91
Figure 4-11: (a) HRTEM Image of Ta ₂ O ₅ nanodimples., (b) EELS spectrum, inset showing O-K edge range	93
Figure 4-12: (a) HIM Image of Au nanoparticles on Ta ₂ O ₅ nanodimples. (b) UV-Vis spectra of bare Ta ₂ O ₅ nanodimples (black dashed line) and Ta ₂ O ₅ nanodimples decorated with Au nanoparticles (red solid line). Inset shows Tauc plot of bare Ta ₂ O ₅ nanodimples.	94

Figure 4-13: Extraction of peak-width and quality factors for gold nanoparticles on Ta ₂ O ₅ nanodimple array (a) and on glass substrate (b)	94
Figure 4-14: Simulated absorption spectrum of various dimple sizes.....	95
Figure 4-15: Simulated optical properties of possible Au nanoparticle/Ta ₂ O ₅ nanodimple configurations.	97
Figure 4-16: Photooxidative Raman spectra of Ta ₂ O ₅ nanodimples	100
Figure 4-17: A schematic of the proposed mechanism for hot electron extraction from Au nanoparticles to Ta ₂ O ₅	101

List of Symbols

α	absorption coefficient
β	material-dependent constant
ϵ_0	vacuum permittivity
ϵ_r	dielectric constant
θ	angle between incident beam and crystallographic reflecting plane
κ	dielectric constant
μ	drift mobility
ρ	density
σ	conductivity
τ	charge lifetime
Φ	quantum efficiency
ϕ_B	Schottky barrier height
χ	goniometer angle
C	capacitance
E	electric field strength
E_F	Fermi level
E_G	band gap energy
E_{CB}	conduction band energy
E_{VB}	valence band energy
e	elementary charge
f	frequency
G_{ph}	photoconductive gain
h	Planck's constant
I	relative intensity of an XRD peak
I	intensity of light
i	current

i_o	material-dependent constant
J	current density
J_{SC}	short-circuit current density
k	Boltzmann constant
L	depletion layer width
l	length
M	atomic mass
N_A	acceptor charge carrier concentration
n	constant denoted for the transition type across band gap
n_{atoms}	number of atoms
n_x	constant phase element coefficient
Q	quality factor
Q	constant phase element
R	resistance
S_q	root-mean-square roughness
T	temperature
T_m	melting temperature
t	time
t_{layer}	thickness of a layer
ΔU	voltage drop
V_{FB}	flat band voltage
V	voltage
V_{OC}	open-circuit voltage
V_m	molar volume
ν	frequency
Z	impedance

List of Abbreviations

AAO	anodized aluminium oxide
AFM	atomic force microscopy
at. %	atomic percent
CVD	chemical vapour deposition
DC	direct current
DEG	diethylene glycol
DI	deionized
DMAB	p,p'-dimercaptoazobenzene
EDX	energy-dispersive x-ray spectroscopy
EELS	electron energy loss spectroscopy
EG	ethylene glycol
EIS	electrochemical impedance spectroscopy
ETL	electron transport layer
FDTD	finite-difference time-domain
FESEM	field emission scanning electron microscope
FF	fill factor
FFT	fast Fourier transform
FTO	fluorine-doped tin oxide
HRTEM	high resolution transmission electron microscopy
HTL	hole transport layer
ISO	International Organization for Standardization
ITO	indium tin oxide
LED	light-emitting diode
LCOE	levelized cost of energy
LSPR	localized surface plasmon resonance
NHE	normal hydrogen electrode

NT	nanotube
PATP	para-aminothiophenol
PBR	Pillings-Bedworth ratio
PCE	power conversion efficiency
RIE	reactive ion etch
SAM	self-assembled monolayer
SERS	surface-enhanced Raman spectroscopy
TEM	transmission electron microscopy
TNTA	titanium oxide nanotube array
UV	ultraviolet
UV-Vis	ultraviolet-visible
wt. %	weight percent
XRD	X-ray diffraction
XPS	X-ray photoelectron spectroscopy
Zn-TNTA	Zn-doped titanium oxide nanotube array

Chapter 1: Introduction

That ordered metal-oxide nanostructures may be spontaneously formed as part of an electrolytic cell is a surprise to many people when they first see the extreme geometries attainable. That this so-called anodizing technique is cost-effective and has already been demonstrated to be suitable for mass-production by a nearly a century of industrial effort only adds to their potential. The sheer versatility of metal-oxide nanostructures is astounding; they can be applied to nearly any application that a metal-oxide can, and as is so often the case in the field of nanotechnology, the functional properties they gain when nanostructured extends their usefulness. Metal-oxide nanostructures have been utilized in topics as far-ranging as dye-sensitized and solid-state heterojunction solar cells, superhydrophobic coatings, as resilient mechanical coatings, as filtration membranes, in photocatalytic reactions such as water splitting, CO₂ photoreduction, and dye degradation, batteries, as gas sensors, biosensors, and in drug delivery and biomedical implants (1-11). However, the largest application focus of metal oxide nanostructures—outside of alumina coatings for wear and corrosion resistance— has been renewable energy harvesting. My research projects have generally been oriented in that direction, demonstrating model devices in photovoltaics and photocatalysis. Thus, although the materials that are developed herein can be applied to almost any of the applications listed above, this thesis begins with a focus on renewable energy.

The remainder of this introduction is organized by topic, loosely from least specific to most specific. Put another way, it begins with an overview of the widest possible aspects of this research—the primary societal problems this research aims to contribute to—and narrows in focus each subsection as it introduces the underlying concepts that guide the thesis research.

Finally, the introduction concludes with the existing gap in knowledge and the resulting thesis question.

1.1 The Energy Problem

The general importance of the development of new and improved renewable energy technologies needs little elaboration; society's over-reliance upon fossil fuels has caused significant pollution and changes to Earth's climate (12, 13). Coupled together with the inevitable exhaustion of fossil fuels, the need for a sustainable supply of energy is a problem that will not rest until a solution is found.

For renewable energy to overtake and replace fossil fuels, they must be able to meet society's demand for energy in terms of cost and capacity. The real cost of energy generation is best considered as the levelized cost of energy (LCOE), which in its simplest form is the sum of costs over the lifetime of a power plant divided by the power plant's total electrical energy produced. The advancements of the last decade have been favourable to renewable energy; in particular, the cost of solar photovoltaic energy has plummeted due to increased manufacturing scale, optimized manufacturing processes, and efficiency gains associated with increased adoption of newer cell architectures. This dramatic cost decrease in LCOE over the last 10 years is shown in Figure 1-1 (14). Furthermore, solar energy is the largest exploitable energy source with more energy striking the Earth's surface in one hour than is consumed by all humankind in a year (15), meaning solar energy has the theoretical capacity to meet society's needs. However, major challenges still exist for solar energy. Photovoltaics are still not consistently the cheaper energy source compared to fossil fuels; further work is needed to increase device performance and decrease the cost of device fabrication. Also, the storage problem for renewable energy is still

unsolved—that is, when the sky is dark, solar-based technologies cannot produce energy (similarly, wind energy cannot be utilized when the wind is still). Much ongoing research is dedicated to improved energy storage methods, including chemical, electrochemical, battery, thermal, thermochemical, flywheel, compressed air, and pumped hydro systems (16). A detailed look at the many possibilities for renewable energy storage is beyond the scope of this thesis and suffice it to say that suitable technologies do not exist yet. One interesting potential solution that does concern this thesis is the splitting of water in to produce its component hydrogen and oxygen, with hydrogen available able to be used as a storable fuel and thus driving an economy built on the delivery, storage, and use of hydrogen (17).

With the larger problems that motivate this thesis research in mind, we now turn to the operating principles of the solar energy harvesting devices that this thesis research is concerned with.

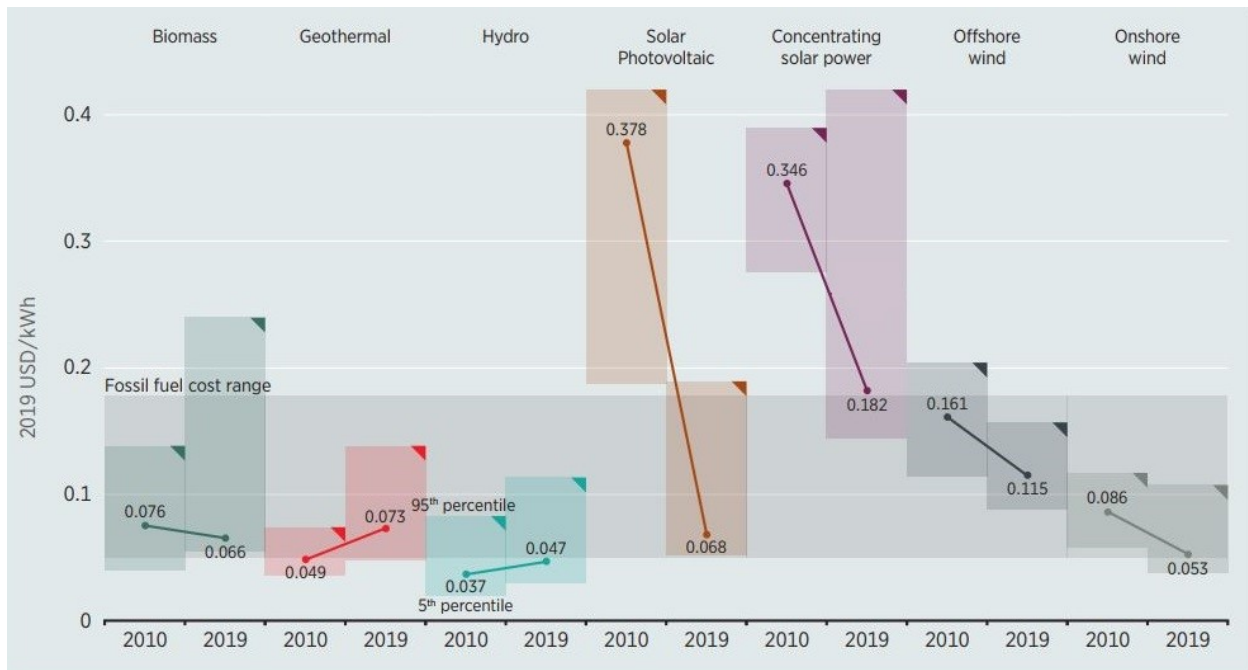


Figure 1-1: Global weighted average levelized cost of electricity (LCOE) from utility-scale renewable power generation technologies for 2010 and 2019.

This graph shows the changing cost of each energy technology over the last decade. The coloured data points for each technology linked by an identically coloured line between 2010 and 2019, which indicates a relative increase or decrease in the cost of that energy technology. The boxes surrounding the data points show the range of costs accumulated from individual power plants between the 5th and 95th percentile. The light grey rectangle stretching across the graph indicates the range of costs associated with fossil fuels between 2010 and 2019, to allow for cost comparison to renewable energy technologies. Adapted from (14). Copyright IRENA 2020.

1.2 Solar Energy Harvesting Devices

Photovoltaics, photocatalysis, and solar thermal technologies are the main topics of focus in solar energy research, although for the sake of brevity I limit my discussion to the first two. The performance of a solar energy harvesting device is dictated by the properties of the materials it is comprised of and the spatial arrangement of those materials. First and foremost, at least one material in such a device must absorb sunlight, which is primarily comprised of ultraviolet (UV), visible, and infrared components. To do useful work with this light, we are usually looking for photoexcitation to occur, where a photon is absorbed and an electron is excited to a higher state,

followed by transfer of this gained energy to do useful work. The key parameter in this process—which controls what wavelength of light is absorbed—is the semiconducting material's band gap (E_g), usually defined as the energy difference between the top of the valence band and the bottom of the conduction band. Photovoltaics and photocatalytic/photoelectrochemical systems both utilize photoexcitation in their initial stages of the mechanism, although afterwards they diverge in some ways. In photovoltaics, photoexcitation means the separation of the electron and the hole left behind in its absence—and their collection at opposite electrodes in the device—to generate a potential difference and produce a current to drive a load. In photocatalysis and photoelectrochemistry, the electron and hole participate in reduction–oxidation reaction(s), and light is used to drive chemical reactions. In all of these systems, the relative band potentials with respect to other components involved in the process must be considered. The desired band potentials are usually contextual and depend on the rest of the system; however, in the case of the ever-interesting water splitting reaction, desired band potentials can be defined. The bottom of the conduction band, E_{CB} , should be more negative than the redox potential of H^+/H_2O (at standard conditions, 0V vs. NHE, -4.4V vs. vacuum). Meanwhile, the top of the valence band, E_{VB} , should be more positive than the redox potential of O_2/OH^- (at standard conditions, 1.23V vs. NHE, -5.6 eV vs. vacuum). In reality, however a band gap of around 1.6 eV–2.4 eV with suitable band positions is needed to account for losses and overpotentials during charger transfer and transport. In general, parasitic processes can also occur in solar energy harvesting devices, decreasing the efficiency of the desired activity. Such processes are numerous, but include chemical side reactions, electron-hole recombination, and free carrier absorption. The extent of the role that these processes play is in turn influenced by factors such as reactivity, fundamental material parameters such as the mobility and lifetime of charge carriers, and device architecture considerations. As

concerns this thesis, many of the problems mentioned here may be addressed by considering nanostructured materials.

1.3 Nanostructured Materials

Paraphrasing definitions given by the International Organization for Standardization (ISO), nanostructures are a composition of inter-related parts, in which at least one of these parts has a dimension on the nanoscale (a length range between approximately 1 nm to 100 nm); by extension, nanotechnology is the manipulation and control over matter in the nanoscale to make use of resultant functional properties (18). The unique properties of nanostructures take many forms, although the most obvious is the greater surface to volume ratio that occurs because of nanostructured materials' small size, the benefits of which include improved contact between materials (such as in solar cells) and an increased number of active sites (such as in photocatalysis and sensors). The basic properties of nanostructured materials are sometimes comparable to bulk materials but may differ quite extraordinarily. For example, the localized surface plasmon resonance (LSPR) exhibited by noble metal nanoparticles—occurring due to collective oscillations of electrons at a specific wavelength of light—causes absorption to be increased at that wavelength of light (19). Gold nanospheres dispersed in solution are a classic and visually striking example of LSPR, they appear as a deep red instead of the shiny yellow we normally expect from gold. This colour shift is far from a mere novelty; LSPR allows for new possibilities in harvesting and detecting light through transfers of so-called hot electrons or hot holes (20-22). Low dimensional materials can have other benefits as well. One-dimensional nanostructures such as nanotubes, nanorods, or nanowires and systems constituted from them present significant advantages over planar, mesoporous, or nanoparticle-based systems. For example, in most structures, charge transport occurs via a “random walk”, where charges do not move in a direct vectoral path, but

rather take a slower, meandering path through the material (23). The increased distance they travel means that losses such as charge carrier recombination become much more likely to occur due to the increased travel time and the increased number of grain boundaries that charges must cross (24). The vectorial charge transport that occurs in one-dimensional structures can help minimize this (25). A further advantage of one-dimensional nanostructures is that the orthogonalization of light absorption and charge collection, meaning photon absorption can be increased without also increasing the diffusion length charges must travel (26). All the points in this subsection taken together, it is for good reason that nanostructured materials are of such widespread research interest. For the purposes of this thesis, I consider metal-oxide semiconductors, which may be nanostructured by simple and efficient methods (27).

1.4 Metal Oxides

Metal oxide materials have seen continual interest at the forefront of renewable energy research and are the material of focus of this thesis. Many of them are cheap, Earth-abundant, able to be produced in large volumes, and are generally chemically and mechanically stable. Metal-oxide semiconductors widely used commercially deployment and across a wide variety of applications, such as coatings and paints, biomedical implants, electronic passivation layers, carrier transport layers and gas sensors (28-31). They have also achieved notable results in renewable energy; for example, the photocatalyst industry is dominated by metal-oxide semiconductors, with TiO_2 being by far the most prevalent (32). Common photocatalytic applications for TiO_2 include self-cleaning glass and degradation of toxic organic compounds in air and water, as TiO_2 can photo-oxidize many organic materials under ultraviolet illumination. However, the “holy grail” of photocatalysis—the splitting of water into hydrogen and oxygen to produce fuel—is still far away from being economically feasible, with most hydrogen production

still occurring via steam reformation of natural gas (33). Similarly, the photovoltaic industry is still largely silicon-based, with silicon-based solar cells occupying over 90% market share as of 2015 (34). Significant issues need to be addressed before metal-oxide semiconductors are ready for wider industrial use in renewable energy applications. As is mentioned above, one technique to improve the properties of metal oxides is by nanostructuring. Many metal oxides can be produced in a nanostructured morphology via the simple and cheap process of anodization.

1.5 An Overview of Anodization

Anodization is, first and foremost, a surface treatment that produces a coating. In ancient times, such coatings were used for the purposes of decoration (and to make an object appear to be of higher value). With the development of electrochemistry, it was realized that the surface oxidation of metals could be controlled, and by the early 20th century the engineering value of anodized coatings was well understood. A dramatic increase in technology utilizing anodizing occurred during World War I as a method to increase the wear and corrosion resistance of aluminium in the aircraft and marine industries. By the end of World War II, the anodizing industry had more-or-less matured, although early models of the mechanism of anodization would remain incomplete until the advancements in materials characterization brought about the mid-20th century (4). Today, anodizing is an integral part of worldwide industry; as a sense of scale, the global market of anodized alumina was 4.65 million metric tons in 2015 (35).

Fundamentally, anodization is driven by applying an anodic voltage to a metal in an electrochemical configuration. In doing so, the natural oxide layer present on the metals (ordinarily a few nanometers) is increased in thickness. After a sufficient time, the electrical circuit is disconnected and the anodized substrate removed from the electrolyte, and then the substrate is

typically rinsed to remove electrolyte residue. A picture and schematic of a typical electrolytic cell used to conduct anodization is shown in Figure 1-2.

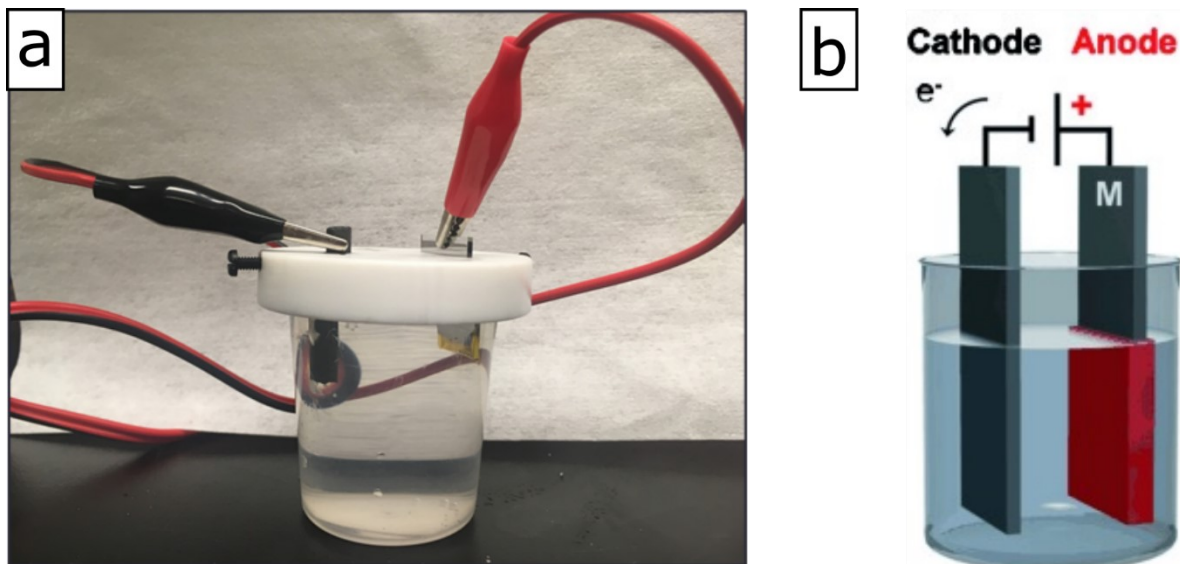


Figure 1-2: (a) A picture of an electrolytic cell used to conduct anodization, with a graphite cathode on the left and a Ti-coated piece of transparent conductive oxide-coated glass on the right. (b) A schematic of anodization.. (b) is reproduced with permission. Copyright 2011 WILEY-VCH Verlag GmbH & Co. KGaA, Weinheim (36)

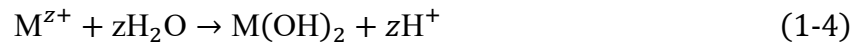
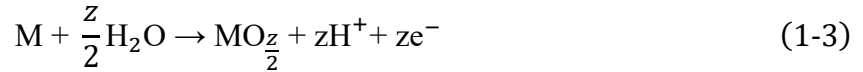
In anodization, hydrogen is produced at the cathode and oxygen produced as a side-reaction at the anode. The oxidation reaction of interest that occurs at the anode is described as:



Where M is the metal to be oxidized. Meanwhile the reduction reaction at the cathode is described as:



The reaction that the M^{z+} ions partake in depends on the anodization parameters, especially the electrolyte contents. Three situations exist: (i) The M^{z+} ions solvitize in the electrolyte, and the metal is dissolved, (ii) the M^{z+} ions react with O^{2-} and a compact oxide is formed, or (iii) a competition between solvation and oxide formation occurs. In the latter two reactions, oxide formation takes place according to the following:



These reactions primarily take place at the metal-oxide interface, with ion migration through the oxide occurring due to the electric field applied. In the case of situation (ii), oxide formation can be described by:

$$E = \frac{\Delta U}{t_{layer}} \quad (1-6)$$

where E is the electric field strength, ΔU is the applied potential and t_{layer} is the oxide layer thickness. As the oxide layer grows thicker, the field strength decreases until ion migration cannot occur, meaning that there is a practical maximum oxide thickness that can be reached (around a few hundred nanometers). The current is described by the high field equation:

$$i = i_0 e^{(\beta E)} \quad (1-7)$$

Where i is the oxide formation current and i_0 and β are material constants. However, in situation (iii) mentioned above, where a competition between solvation and oxide formation occurs, pores are formed in the oxide. These pores, which initiate at local imperfections within the oxide, are induced by adding an appropriate amount of media capable of dissolving oxide, such as fluorides.

In this case, as pores etch away oxide, more metal may be oxidized, and the pores thus “burrow” through the metal, up to hundreds of micrometers. Differences in morphology between a compact layer (also referred to as barrier-type) anodization and a porous-type anodization is shown in Figure 1-3, as well as typical current-time characteristics observed when anodizing to form the two morphologies. The current observed in an anodization has an ionic component and electronic component; however, due to the growth of the oxide layer, the electronic component is quickly diminished and the rate-determining step of the anodization process depends on the movement of ions. In Figure 1-3a, an exponential drop in current is observed when compact oxides are formed, while in Figure 1-3b, three stages are observed when porous oxides are formed. In the first stage, current decreases as initial oxide formation occurs. In the second stage, the current increases as pore formation in the oxide initiates. Finally, in the third stage the current drops again and reaches steady state, as pores elongate through the oxide layer as diffusional effects in the electrolyte take on a more important role. Porous anodization can also be performed using galvanostatic conditions, but they are usually performed using potentiation conditions as they offer better control over structure morphology and higher growth efficiencies (37, 38).

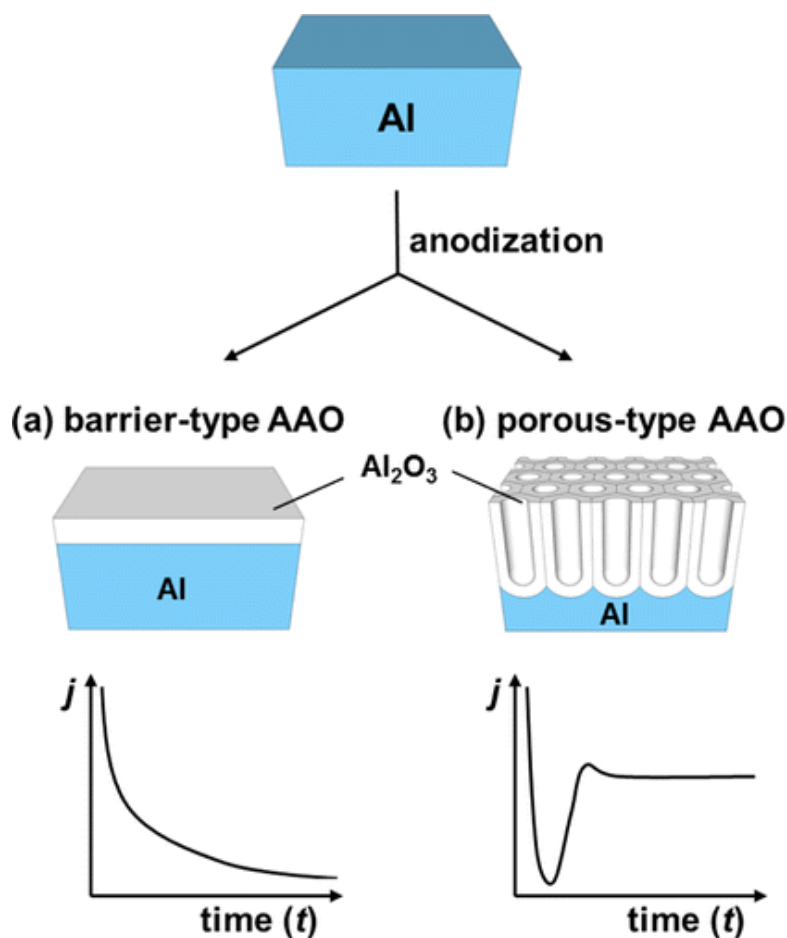


Figure 1-3: Schematic showing oxide anodization morphologies, using aluminum oxide (AAO) as an example (a) compact oxide, also known as barrier-type (b) porous-type anodization. Below each is typical current (j)-time(t) transient curves obtained using potentiostatic anodization.

Reprinted with permission from (39). Copyright 2014 American Chemical Society.

Many different metals have been successfully anodized to form porous and/or tubular structures, including Al, Ti, V, Fe, Co, Ni, Cu, Zn, Ga, Zr, Nb, Sn, Hf, Ta, W, and related alloys (40-57). There is no unified model to describe their formation, but studies concentrated especially on Al and Ti suggest some of the formation mechanisms can be at least partly generalized across all of them. Broadly, two primary mechanisms have been proposed, which are compatible with one another. Considering the older of the two: for decades, the development of pores was attributed to field-assisted dissolution processes causing local etching at the bottom of a pore, which was

balanced by the growth of oxide (58). This selective etching at the bottom of pores has been suggested to occur there as they are areas of high electric field, which ensure weakened polarized M-O bonds (chemical assisted dissolution) (59), and a high concentration of etching species that compete with O^{2-} migration through the oxide layer (60). The pH of the electrolyte, etchant species concentration, and composition of the electrolyte (especially availability of oxygen ions and by extension water content) all play a significant role in in this model. A lower pH or higher etchant species concentration lead to higher etching rates, while oxygen ion availability has a complex effect on the process, increasing the rate of oxide formation and dissolution processes. However, in recent years a field-assisted flow mechanism has gained traction, where the oxide undergoes compressive stresses due to electrostriction and volume expansion (58, 61). Thus, the plasticity of the oxide and the force from the electric field causes the oxide to flow from the barrier layer near the metal-oxide interface towards the pore walls. This model has been validated by tracer studies using species such as oxygen isotopes, nanolayers of Ti-W alloys, and arsenic (62-64). It is observed that the tracer species migrate up the pore walls, lending validity to the field-assisted flow model. However, it should be stated that anodization is by no means fully understood. There are merits to both mechanisms, and both are useful in describing observed experimental phenomena.

Before beginning a discussion of the origins of nanostructuring from anodization, it should be emphasized that there is no fundamental difference between “nanotubular” and “nanoporous” structures; they are qualitative descriptions used interchangeably in the earlier works in the literature. Through this thesis, I consider the distinction between the two terms to be analogous to how all squares are rectangles but not all rectangles are squares; similarly, all nanotubes are nanoporous but not all nanopores are nanotubular. The key difference that is observed between

nanopores and nanotubes is a secondary spacing in between the pores that defines a distinct tube. Several models exist to explain this spacing, although it is my opinion that the most plausible explanation is the formation of water-soluble species in between primary pitting formations, which is supported by field-assisted flow model as discussed above. Considering the case of TiO_2 nanotubes as an example, this is generally done by the action of F^- ions migrating through the oxide layer, as is shown in Figure 1-4. A fluoride rich layer can be shown to exist at the TiO_2/Ti interface; this fluoride rich layer is displaced by plastic flow along the cell walls, and are eventually dissolved (65). As the fluoride rich layer is chemically dissolved by water, by extension the water content also plays a critical role for nanotube formation in the case of TiO_2 ; at very low water contents a nanoporous morphology occurs instead of a nanotubular (66).

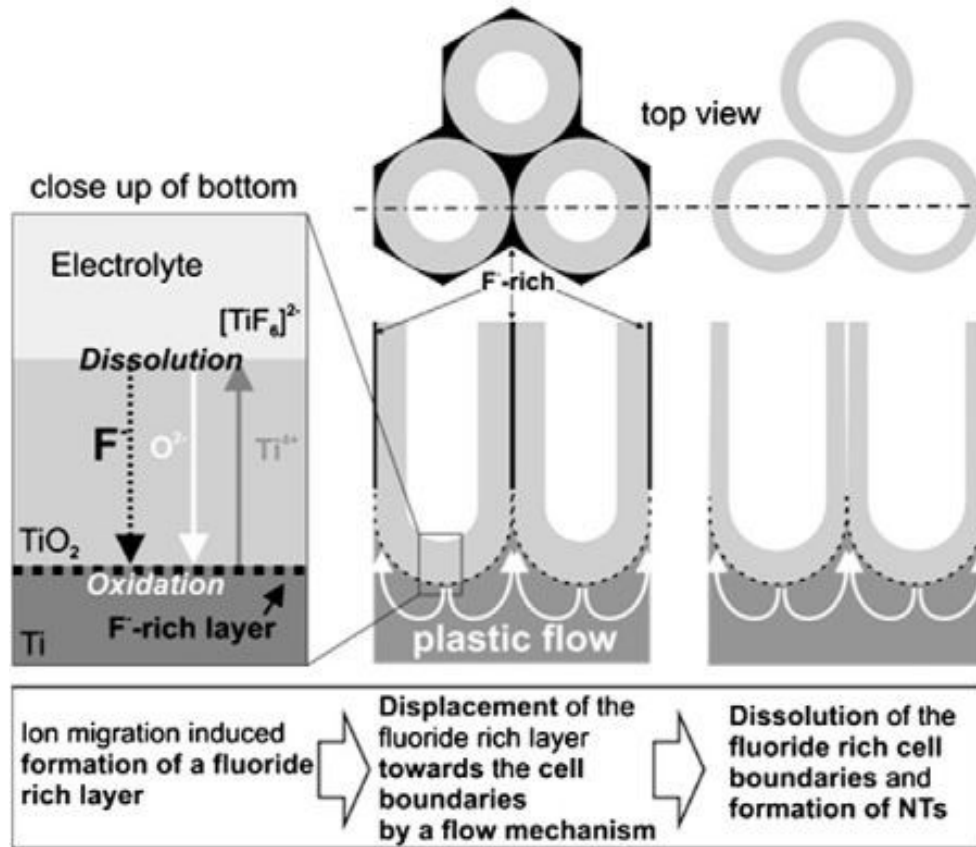


Figure 1-4: Schematic of TiO₂ nanotube (NT) formation, and the plastic flow mechanism that leads to distinct nanotube formation as opposed to nanopores.

Reprinted from (65) with permission from Elsevier.

The anodizing voltage used during the anodizing process plays a major role in the resulting morphology of the anodized films. Within a range of parameters, the diameter of the formed pores displays linear dependence on voltage, where higher voltages result in larger pore diameters. This linear dependence is related to the oxide growth rate of the film itself, as thicker oxide layers are formed along the side walls of the pores, which can be chemically dissolved and thus a wider pore may be formed as shown in Figure 1-5. The anodizing voltage has also been strongly linked to the self-ordering of the porous array (67); this self-ordering is prominently visible when looking down at nanoporous and nanotubular structures. As a simple explanation of existing models (68), the potential influences the compressive oxide stresses between pores, and within a certain parameter

window, self-ordering is optimized. However, it should be noted that the mechanism for self-ordering is still a controversial topic, and that other factors such as interfacial diffusion, field-dependent oxide conductivity, and ion migration have also been suggested to influence porous self-ordering and should not be ignored (69-71).

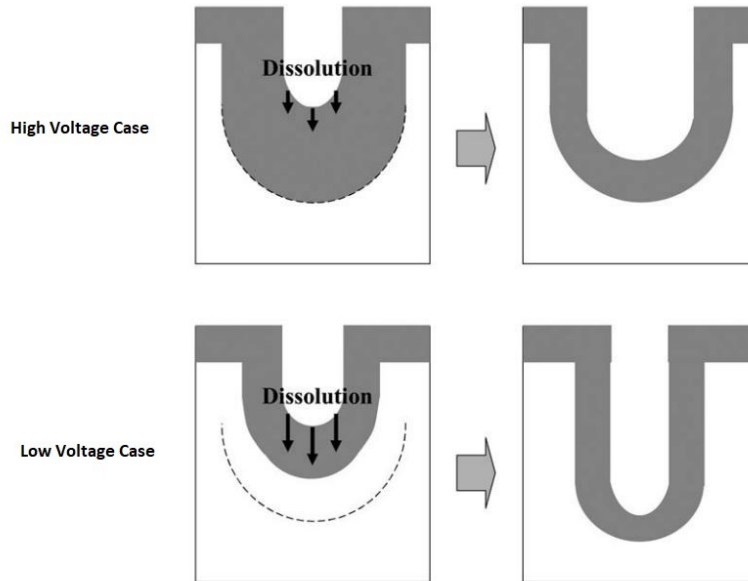


Figure 1-5: Schematic of pore formation at higher and lower voltages, where a higher voltage used leads to larger diameter pores.

Adapted with permission from IOP Publishing (72).

1.6 Sputtering

Throughout this thesis, anodization is conducted on thin metal films deposited by direct current (DC) magnetron sputter deposition. By bombarding a target material with ionized gas molecules, vaporized atoms are ejected. These atoms travel across a chamber to adsorb on a target substrate, possibly undergo further diffusion on the surface, and form a thin film. The morphology of the formed film is heavily dependent on deposition parameters such as target current, voltage, pressure, substrate-target distance, temperature, working gas, sputtered material, and the substrate

(73). So-called structure zone diagrams are used to represent trends in film microstructure versus deposition parameters. The classic Thornton model (74), shown in Figure 1-6, shows changing film morphology versus sputtering pressure (a proxy for kinetic energy effects of incoming particles), and substrate temperature (a proxy for film temperature which is much more difficult to measure). Substrate temperature is presented as T [K] as a fraction of melting temperature T_m [K]. According to the model, common morphologies occurring within windows of sputtering pressures and temperatures can be described as Zone 1, Zone 2, and Zone 3, and a transition zone called Zone T that occurs between Zone 1 and 2. Zone 1 is composed of a tapered, porous structure separated by voids, Zone 2 is composed of a dense, columnar structure, Zone 3 is composed of a recrystallized grain structure, and Zone T occurs as a hybrid of Zone 1 and 2 and is composed of densely packed fibrous grain.

In the context of sputtering to form a metal film to be anodized, it is understood that a denser metal substrate leads to a more well-defined and ordered nanotube morphology (75, 76). This means that Zone 1 is to be avoided to ensure a superior nanostructure upon anodization. Furthermore, increasing substrate temperature, T [K], to a higher fraction of its melting temperature, T_m [K] as per Figure 1-6, is not always practical due to possible undesired substrate interactions, not to mention that heating is an energy-intensive process that increases fabrication costs. Decreasing sputtering pressure can help ensure that denser Zone T microstructures are formed instead of Zone 1, but the pressure being too low mean that the plasma that is essential to the sputtering process to extinguish, as not enough ion collisions occur to sustain the plasma. Thus, sputtering pressure and temperature must be carefully controlled to ensure a satisfactory porous metal oxide product.

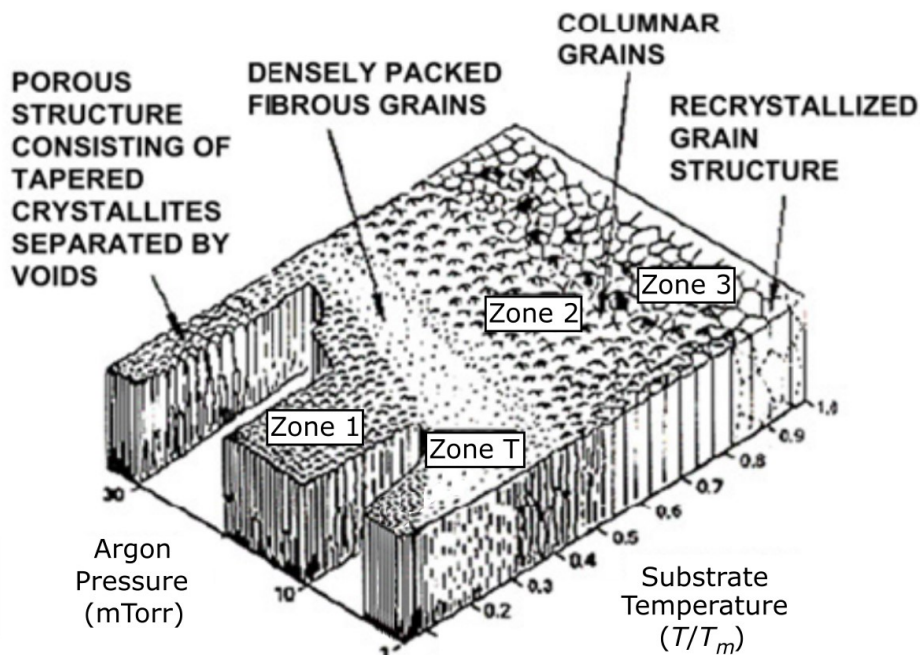


Figure 1-6: Thornton model for sputtered metals (77).

Adapted with permission under Creative Commons Attribution-Noncommercial License 3.0 from (78)

1.7 The Research Leading Up to this thesis

Throughout the development of anodization progress has been led by experimentation, with theoretical attempts to explain the phenomena coming afterward. Nanoporous alumina is the most studied material, being first produced sometime in the 19th century with observations of the porous structure and commercial applications occurring at the dawn of the 20th century (4). For the bulk of the 20th century, nanoporous alumina was largely limited for use in corrosion and wear resistance; however, in the 1980's, interest in the engineering possibilities of nanotechnology began to build and the anodization process took on new significance. Over the next two decades, several landmark discoveries were made. In 1984, the first example of nanoporous TiO₂ was demonstrated (41). In 1989, Furneaux et al. demonstrated a method by which porous alumina could be detached from the underlying aluminum to form a free-standing membrane—a technology that

went on to become Anopore membranes, now widely available commercially (79). In 1995, Masuda and Fukuda demonstrated very highly ordered pores of alumina, and showed that they could be used as templates to form metallic nanostructures (40). In 1999 and 2001 respectively, Zwilling et al. and Gong et al. demonstrated the anodic growth of TiO₂ nanotubes, two very highly cited studies that can be said to be the seminal works on modern anodizing as it relates to nanotechnology (42, 80). It can also be noted from a survey of the literature that most of the studies concerning nanostructured metal-oxides formed by anodization are on Al₂O₃ and TiO₂, although as mentioned above, the technique has also been extended to other material systems.

Over the last two decades, anodization techniques to produce porous morphologies have been refined, especially with regards to TiO₂. TiO₂ nanotubes were initially confined to only a few hundred nanometers in length owing to the aggressiveness of the HF-based electrolyte used (42, 80). In 2005, Cai et al. and Macak et al. demonstrated that by using fluoride salts instead of HF, nanotube lengths could be increased to several microns (81, 82), and in 2006 and 2007, the Craig Grimes research group demonstrated in a series of papers that by using organic-based electrolytes, nanotubes many hundreds of microns long could be made; this also shifted the tube morphology from having rippled to smooth sidewalls (5, 9, 83, 84). This marked a point of maturity in TiO₂ nanotube research. Since then, the functionality of anodized nanostructures has been extended by techniques such as doping, decoration by self-assembled monolayers (SAMs) and nanoparticles, integration with novel materials, and novel anodization techniques such as voltage stepping to form periodically modulated nanotubes (3, 85-88). Furthermore, as listed at the beginning of this chapter, such nanotubes have been demonstrated in an extraordinarily diverse array of applications. Most recently, studies have turned to tailoring the properties of anodized nanostructured metal-oxides, establish structure-property relationships, and leverage the simplicity

of anodization to produce novel nanoscale morphologies inaccessible by any other fabrication method.

The connection between the starting metal substrate and resultant nanostructured anodized films is not fully understood, although the principle variables can be established from the body of work done on anodized Al_2O_3 ; broadly speaking, the microstructure, surface roughness, and impurities of the substrate have been identified as influencing the final film (89). Considering the case of native substrates, as in metal foils, only a few studies working have attempted to link the properties of the starting substrate to the resultant nanostructures outside of anodized Al_2O_3 . Of note, in 2014, Leonardi et al. demonstrated a connection between grain orientation and nanotube growth speed (90), and between 2016 and 2018 the Macak group published three studies comparing TiO_2 nanotubes made with Ti foils possessing differing microstructures, concluding that impurities in the Ti had the largest impact on resultant nanotubes (91-93). A few more studies published between 2015 and 2017 by Chappanda et al., Choudhury et al., and Farsinezhad et al. considered the influence of sputtered films (76, 94, 95). These papers demonstrate some of the differences between conventional foils and deposited films as they relate to anodizing. Conventional foils are made by hot rolling, a process that produces a dramatically different microstructures compared to sputtered ones: metal foils typically possess grain sizes of the order of tens or hundreds of microns, while sputtered films possess grain sizes on the order of tens to hundreds of nanometers. The surface roughness of conventional foils as-fabricated by hot rolling is relatively high, although post-fabrication treatments such as chemical or mechanical smoothing may be done; meanwhile, the roughness of deposited films is influenced by deposition parameters and the roughness of the underlying substrate.

To date, most of the research on anodized nanostructures uses native substrates such as metal foils as the starting material. The major reason native substrates are used so often is rooted in practicality: metal foils are relatively cheap and can be purchased directly from manufacturers. Also, metal foils are hundreds of microns to many millimeters in thickness, meaning there no risk of over-anodizing nanotubes owing to complete consumption of material. However, metal foils do not allow for anodized structures to be utilized in many device configurations, such as in photovoltaics, optical sensors, and displays which rely on transparent substrates and the electronic and photonic systems that are built on silicon wafers. Thus, deposition of thin metallic films by thermal evaporation or sputtering on so-called non-native substrates is a much more desirable configuration. That deposited thin films can be anodized to form nanostructured morphologies has been known for some time now; thin films of Ta were anodized on a glass slide for interferometric sensing as early as 1973 (96) and transparent TiO₂ nanotubes on glass, silicon, and alumina were demonstrated in 2005 (97). However, much of the novel experimentation that has been demonstrated on anodized metal foils in recent years has not yet been attempted on deposited metal films. The results of the experiments on metal foils are claimed to improve desirable properties and/or diminish undesired ones for relevant device applications, as indicated by observations such as the morphology by microscopy and crystal structure characterizations, and results such as increased photovoltaic current density and photon-to-current conversion efficiencies; this means that potentially harnessing these improved properties is of scientific interest. Furthermore, the (claimed to be) improved nanostructured materials have not been adequately characterized, partly owing to the limited sample architecture; meanwhile, the use of non-native substrates enables certain characterizations, such as those relying on optically transmitted light, to be possible. The innate differences of deposited films compared to foils also allows an opportunity to test the

validity of proposed models that describe the factors that cause the unique functionalities observed in anodized nanostructures. Finally, the differing material geometry of thin films of metal on non-native substrates also enables new classes of nanostructures formed via anodization.

1.8 Research Questions Asked, and Thesis Organization

The major research question that this thesis asks is “*What are the effects of conducting novel anodization techniques on sputtered non-native substrates?*”. This question is answered for three anodizable metals through Chapters 2–4, each of which concerns a self-contained research project, with Chapter 5 serving as an overall conclusion. Each of these chapters uses its respective material to answer sub-questions that together answer the major research question of this thesis. Generally speaking, this is accomplished by monitoring the anodization process during synthesis, by characterizing the resultant materials, and by fabrication and testing of devices made using these materials. In all cases, to the very best of my knowledge, no one has previously fabricated, much less investigated or utilized, these systems when anodized from sputtered films.

The specific relevant background for each project is introduced as an introductory subsection within each chapter; however, below is a road map that outlines Chapters 2–4 and the research sub-questions that were asked during completion of this thesis. Within each chapter, the sub-questions as listed were asked in an approximately chronological order as the research progressed, so that a positive answer to the first question naturally led to the latter questions.

Sub-questions of Chapter 2, which considers preferentially oriented nanotubular TiO₂:

1. Can preferential orientation of TiO₂ nanotubes on non-native substrates be obtained?
2. How do required or optimal synthesis conditions compare to foil when attempting to obtain preferentially oriented nanotubes on non-native substrates?
3. How do the properties of preferentially oriented nanotubes compare to conventional randomly oriented ones?

Sub-questions of Chapter 3, which considers nanoporous NiO:

1. Can nanoporous NiO be formed on non-native substrates?
2. How does substrate surface texture and material of choice impact resultant morphology?
3. What are the properties of nanoporous NiO on non-native substrates?

Sub-questions of Chapter 4, which considers nanodimpled Ta₂O₅ formed from nanotubular Ta₂O₅:

1. Can Ta₂O₅ nanotubes be formed on non-native substrates, and delaminated to leave behind Ta dimples?
2. Can Ta dimples be oxidized to produce a similarly nanodimpled Ta₂O₅?
3. How do synthesis parameters control Ta anodization and the resultant morphology of both Ta and Ta₂O₅ nanodimples?
4. How does nanodimpled Ta₂O₅ perform as a platform for plasmonic photocatalysis?

Some final notes on style: while all the text in this thesis was written by myself, the use of the pronoun “we” is kept intact from the original manuscripts prepared for publication throughout Chapters 2–4. Also, on occasion and especially in the introductions, fundamental information is repeated between chapters as each chapter was originally prepared as a standalone manuscript. The original wording is left intact so as to preserve the flow of the text and serve as a reminder of important concepts to the reader.

Chapter 2: Preferentially Oriented TiO₂ Nanotubes

The work presented in this chapter is based off a published journal article. Reproduced with permission from IOP Publishing (98).

2.1 Chapter Introduction

TiO₂ nanotube arrays (TNTAs) are a vertically oriented and self-organized nanomaterial platform with a high degree of order that may be synthesized using electrochemical anodization (36, 58, 99, 100). As the sidewall of each nanotube can be considered nearly one dimensional, they offer the potential for more directional electron transport (101-103) with the mobility in single nanotubes measured to be $3.6 \text{ cm}^2 \text{ V}^{-1} \text{ s}^{-1}$ along the tube axis (104). TNTAs are used in a variety of optoelectronic applications such as the electron transport layer (ETL) in perovskite solar cells (2), as the photoanode in dye sensitized solar cells and sunlight-driven water-splitting (1, 105-108), as the sensing electrode/scaffold in photoelectrochemical and photoluminescence biosensors (109-111), and as a photocatalyst for both oxidation and reduction reactions (112-114).

As-fabricated by the anodization method, the TiO₂ nanotubes are amorphous: while the nanotubes have a fully formed morphology, they are non-crystalline. To take advantage of TiO₂'s properties as a wide-bandgap semiconductor and utilize them in electronic applications, TNTAs should be annealed to a crystalline phase: either anatase, rutile, or a mixture of both (108, 115). Annealed nanotubes are polycrystalline, with the grains comprising them randomly oriented under most conditions (116). The grain boundaries in polycrystalline materials are a source of traps for diffusing electrons, hindering charge transport (117). This poorer charge transport at grain boundaries has been demonstrated to have negative effects on devices used in areas such as solar energy generation, catalysis, sensing, and electronics (118). Special care can be taken to ensure

that upon annealing these grains exhibit a preferred orientation—meaning that each crystallite is oriented in the similar direction relative to one another—which is expected to decrease recombination at grain boundaries and help alleviate performance losses. This can be expected owing to a decrease in perturbation of the electrostatic potential at grain boundaries coinciding with the decrease in grain boundary energy. Considering that charge carrier mobilities in bulk single crystal TiO_2 are around 3-6 orders of magnitude greater than that of polycrystalline nanostructured materials (*119*), there clearly exists tremendous potential to improve every TNTA-based device by superior control of crystal texture.

Throughout this work, we allude to several prior studies on the TNTAs anodized on a native Ti foil, which served as inspiration for some of the parameters tested in this study. Before beginning a discussion of prior work, it should be emphasized that in all studies, including this one, the grains in the preferentially oriented nanotubes have been oriented such that the [001] direction is parallel to the growth direction of the nanotubes, as shown in Figure 2-1. We focus our study on three factors that have been suggested to contribute to textured TiO_2 nanotube formation: (i) a suitable water content of the anodizing electrolyte, (ii) a sufficiently smooth Ti surface prior to anodization, and (iii) incorporation of zinc into the as-grown nanotubes prior to annealing (*120-123*). Park et al. suggested that a suitable water content in the ethylene glycol-based electrolyte (~ 2 vol %) enhances preferred orientation by controlling the amount of hydroxyl groups incorporated into the amorphous nanotubes during anodization, where a higher water content is associated with a higher hydroxyl group content (*116*). A proper hydroxyl group content would mean crystallization starts at the fluoride-rich outer nanotube surface during annealing, and as crystallization propagates through the nanotube to the inner surface, preferred orientation results. Too low a hydroxyl content would lead to a low O/Ti ratio and stoichiometric TiO_2 would not

form; too high a hydroxyl content means crystallization starts at sites throughout a nanotube, resulting in randomly oriented nanotube grains. The same research group, this time in a paper authored by Seong et al., later demonstrated that another prerequisite for preferentially oriented TNTAs is a sufficiently smooth Ti surface prior to anodization; suitable hydroxyl content is again suggested as the mechanism (122). They suggest that a rougher surface causes a weaker local electric field across the barrier oxide layer during anodization due to irregular pore formation, which in turn leads to an increase in hydroxyl groups in the nanotubes. Finally, John et al. demonstrated a method of further increasing the preferential orientation of TNTAs (123). By using a cathodic voltage to the nanotubes in a 1 M zinc sulphate electrolyte after nanotube growth but prior to annealing, Zn is doped into the amorphous TiO₂. They propose that during annealing, Zn is preferentially adsorbed onto {001} facets, reducing their surface energy and increasing their area allowing for the stacking of crystallites connecting these facets, ultimately leading to increased preferred orientation (123). Taken together, this suggests that careful selection of synthesis parameters is essential to obtain a preferential orientation, and the work on obtaining preferentially oriented nanotubes may be contrasted with the wide bulk on anodized nanotube literature where little to no regard is given to crystalline orientation. To obtain preferential orientation, regard to crystal nucleation and propagation must be given during nanotube synthesis. However, to date, all previous studies have investigated TNTAs many microns long, fabricated on anodized titanium foil. Herein, we report on the engineering of much shorter preferentially oriented TNTAs hundreds of nanometers long on fluorine-doped tin oxide (FTO)-coated glass and Si wafer substrates, a configuration more relevant for device applications.

It is important to note that all previous reports on preferentially textured TiO₂ nanotubes used TNTAs on Ti foil substrates; crystallographically oriented TNTAs on transparent

and more technologically relevant non-native substrates are yet to be demonstrated. Furthermore, previous studies have utilized TNTAs many tens of microns in length, whereas many device applications demand much shorter TNTAs. We note that very little optoelectronic characterization has been reported for textured nanotubes, thus making it challenging to construct structure-property relationships. In this study, we form sub-micron length preferentially textured nanotubes on FTO-coated glass and silicon wafer substrates. We have investigated the relative importance of synthesis conditions that may cause preferential orientation of such TNTAs and attempted to provide insights into the differences and similarities between TNTAs formed from Ti foil versus sputtered Ti on a substrate. In addition, we have reported for the first time the performance of halide perovskite solar cells containing Zn-doped nanotubes prepared by electrochemical reduction as the ETL. We conclude by measuring the steady-state and transient photoconductivity response of untextured and textured nanotubes to gain deeper insights into carrier trapping and recombination phenomena.

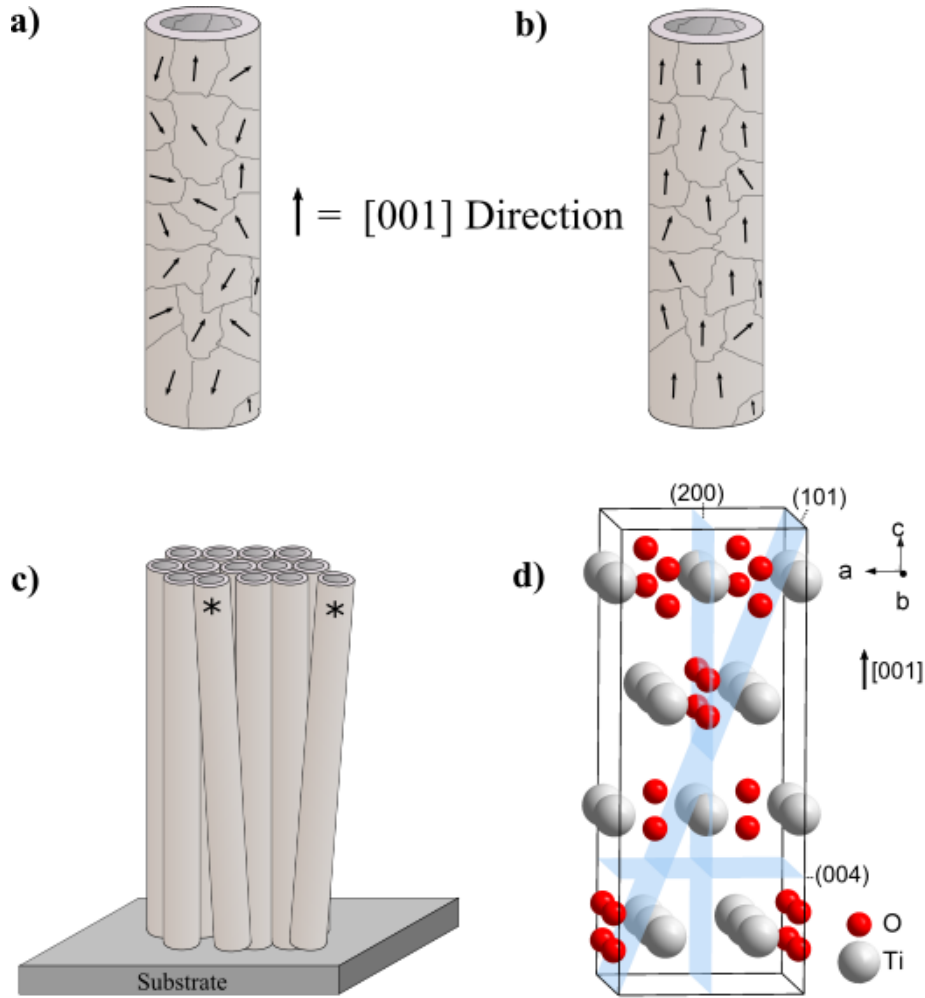


Figure 2-1: Schematic diagrams of the grain structure of anodized TiO_2 nanotubes
 (a) A nanotube comprised of randomly oriented grains, depicting the $[001]$ direction of each grain in random directions. (b) A nanotube comprised of preferentially oriented grains, depicting the $[001]$ direction of each grain oriented preferentially along the length of the nanotube. (c) TiO_2 nanotube arrays grown orthogonally on a substrate. Two nanotubes have been marked with a $[\ast]$, to show that some nanotubes may exist at a skew angle with respect to the substrate. It should be noted that preferentially oriented skewed nanotubes would still show their preferential $[001]$ direction aligned with the length of the nanotube. (d) The crystal structure of anatase TiO_2 (124).

2.2 Experimental Details

2.2.1 Sample Preparation

The FTO-coated glass substrates were cleaned by ultrasonication for 10 minutes in deionized water, acetone, and then methanol. The silicon wafers were cleaned of organic residues by immersion for 15 minutes in a piranha solution comprised of a 3:1 mixture of sulfuric acid and hydrogen peroxide. The substrates were then loaded into a DC magnetron sputtering system. After evacuating the sputtering chamber to around 10^{-6} Torr, argon was used to fill the chamber at a rate of 50 ccm to bring the pressure back up to 1 mTorr. A 99.99% pure Ti target was used at a power of 300 W to deposit 500 nm Ti films on the substrates while at room temperature; this process took 1 hour. Before anodization, the Ti-coated substrates were partially covered with Kapton tape to limit the exposed area to *ca.* 2 cm². This was done to limit high current densities at the edges of the substrate.

The samples were then anodized at room temperature in a well-mixed ethylene glycol-based electrolyte containing 0 to 4 vol.% deionized water and 0.3 wt.% NH₄F. Anodization was conducted using a variable DC power supply at 40 V using a 6-mm diameter graphite rod as the counter electrode; the anode and cathode were spaced 3 cm apart and the electrolyte was not stirred during anodization. The anodization was stopped the moment the current began to rise after an initial decrease; this took about ten minutes. The anodically formed nanotube samples were rinsed with methanol and dried under nitrogen after synthesis. To remove a mesoporous top layer that is commonly left at the top of TiO₂ nanotubes after synthesis and to further clean the samples of any debris formed after anodization, an Oxford PlasmaPro NGP80 Reactive Ion Etcher (RIE) was used. The etching process used the working gas SF₆ at a pressure of 20mTorr and a forward power of

250 W for 200 seconds. This was followed by an RIE clean using O₂ gas at a pressure of 150mTorr and a forward power of 225 W for 10 minutes.

The zinc incorporation process was done following an electrochemical process described by John et al. (123). Briefly, a cathodic voltage of 2.5 V was applied to the nanotube samples using graphite as the anode. For all samples where it is not otherwise noted, this was done in an aqueous 0.1 M ZnSO₄ electrolyte for 10 seconds on FTO substrates and 7 seconds for Si substrates. All samples were then annealed at 475 °C for 3 hours. Samples incorporated with Zn (Zn-TNTA) and pristine TNTA were then placed in a 1 M HCl solution in order to remove ZnO grown on the tops of the Zn-TNTA and to ensure any mesoporous top layer on the TNTA was completely removed.

2.2.2 Material Characterization

A Zeiss Sigma Field Emission Scanning Electron Microscope (FESEM) equipped with an Oxford energy-dispersive x-ray spectrometer was used to image the TNTA and conduct elemental analysis. The surface roughness of the sputtered Ti films was measured using a Bruker Dimension Edge atomic force microscope (AFM) in tapping mode. Ultraviolet-visible (UV-Vis) spectroscopy was carried out using a Perkin Elymer Lambda 1050 Spectrophotometer equipped with a 100 mm integrating sphere accessory. X-ray Diffraction (XRD) patterns were collected with a Bruker D8 Advance Diffractometer equipped with a VANTEC-500 2D detector using a Cu-K α source.

To conduct photoconductivity measurements, metal contacts were deposited via e-beam evaporation onto the TNTA through a shadow mask. The substrate was held at an angle of 80° with respect to the normal to the direction of the flux of evaporant to minimize the depth of penetration of the metal into the nanotubes. The current–voltage characteristics of the samples were measured at room temperature using a Keithley 4200 semiconductor parameter analyzer

connected to the metal contact and to exposed FTO (the FTO contact was set as the ground). Measurements were taken under dark conditions and under the illumination of a 365 nm light-emitting diode (LED) incident on the glass side of the substrate from held 6.5 cm away. At this distance, the LED had a measured intensity of $143 \mu\text{W cm}^{-2}$. A bias of 2 V was applied during transient photoconductivity measurements.

2.2.3 Solar cell preparation and testing

For solar cell fabrication, the TNTAs were first immersed in a 70 °C, 40 mM aqueous solution of TiCl_4 for 60 minutes, and subsequently dried, and then annealed at 500 °C for 30 minutes. This TiCl_4 treatment is used to improve the charge transport and reduce the interfacial recombination by passivating defect sites on the surface of TNTAs (125-128). The perovskite precursor solution was prepared by dissolving 1 M formamidinium iodide (FAI), 1.1 M PbI_2 , 0.2 methylammonium bromide (MABr) and 0.2 M PbBr_2 in a 4:1 mixture of dimethylformamide: dimethyl sulfoxide (DMF: DMSO). The obtained precursor solution was then stirred at 70 °C for 2 hours and then deposited onto 300 nm long TNTA grown on FTO-coated glass (“the substrate”). This was done as follows: first, around 200 μL precursor solution was dropped onto the TNTA. Next, the substrate was spun at 1000 rpm for 10 seconds and then 4000 rpm for 20 seconds, with no pause in between the two spinning steps. During the 4000 rpm spinning step, 100 μL of chlorobenzene was dropped on the substrate at the 15-second mark for rapid crystallization (129); please note that this equates to the 25-second mark if referring to the entire 30 second spinning process. The substrates were then annealed at 100 °C for 30 minutes. After that, a solution was prepared to be spin-coated as an approximately 300 nm thick hole transporting layer (HTL). 72 mg Spiro-MeOTAD was first dissolved in 17.5 μL of a stock solution comprised of 520 mg mL^{-1} of bis(trifluoromethanesulfonyl)-imide in acetonitrile. Separately, 28.8 μL of 4-*tert*-butylpyridine

was dissolved in 1 mL of chlorobenzene and then added to the previous solution. 50 μL of the solution was then dropped onto the substrate and spun at 1000 rpm for 10 seconds. Finally, a 70 nm thick layer of gold with a 0.3 cm^2 area was deposited using e-beam evaporation to complete the device; 4 devices were fabricated on each substrate. A schematic of our solar cells may be viewed in Figure 2-2. The current-voltage characteristics of the samples were measured using a Keithley 4200 Semiconductor Parameter Analyzer. Solar cell testing was conducted using one sun AM 1.5G illumination from a Newport Instruments collimated Class A solar simulator.

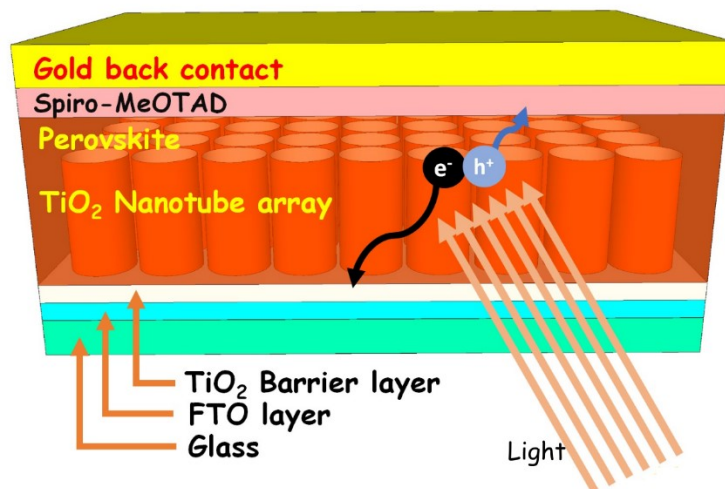


Figure 2-2: Schematic of the halide perovskite solar cell utilized in this study.

Incoming light is absorbed by the perovskite layer and created excitons (electron-hole pairs). Electrons move through the TiO_2 nanotube arrays before being collected at the FTO layer. Holes move through Spiro-MeOTAD before being collected at the gold back contact.

2.3 Results and Discussion

2.3.1 Preferentially oriented TiO₂ nanotube arrays on non-native substrates

We begin by investigating the three synthesis conditions identified in the previous section that are suggested to lead to preferential orientation as they pertain to TNTAs grown from sputtered Ti films on non-native substrates. Observations during the synthesis of TNTAs were invaluable to obtaining a well-aligned, tubular morphology; as-formed, nanotubes were characterized by FESEM and EDX. As noted in the Experimental section, anodization of the Ti films on non-native substrates was carried out until the moment the current began to rise. The rise in current corresponded with the formation of visible spots in the titanium oxide layer. As we observed during FESEM investigations, these spots were areas where the TiO₂ began to etch completely through to the underlying substrate. The exact length of time this took varied slightly with each substrate, in part owing to slight differences in surface area and titanium film morphology. Macroscopically, the samples were visibly transparent; an image of a sample and transmittance spectra are shown in Figure 2-3. FESEM was used to image the TiO₂ nanotubes after fabrication. ZnO flakes could be noted on Zn-TiO₂, as described by John et al.; following that work, these nanoflakes were removed by a soak in HCl after annealing (123). Some Zn remained in the TNTAs after HCl soaking, however, having been doped into the lattice of TiO₂, as verified by EDX. The nanotubes were on top of a thin compact TiO₂ layer of about 100 nm thickness; this compact layer occurs because of the formation of an electrochemical barrier layer during anodization (84, 130, 131) and also because a very thin layer of Ti is left over after anodization and becomes oxidized during the annealing step. The nanotube morphology varied with the water content of the electrolyte, although the lengths of the nanotubes stayed relatively constant at about 800 nm (with deviations occurring partly due to inhomogeneities in sputtering thickness). The morphology of the nanotubes was

influenced by the underlying substrate and the water content of the electrolyte, as shown in Figure 2-4. TNTAs on Si were observed qualitatively to be more ordered and more close-packed than TNTAs on FTO; similarly, TNTAs grown with higher electrolyte water contents were more ordered and more close-packed than TNTA grown with lower electrolyte water contents. These results agree with previous work done on TNTA grown on non-native substrates (75).

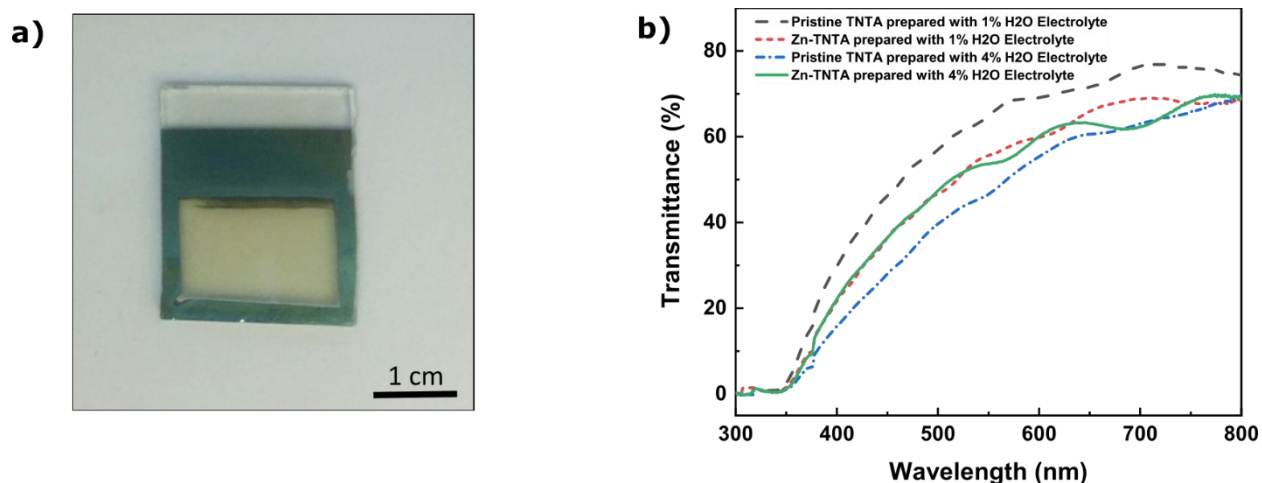


Figure 2-3: Macroscopic Image of TiO_2 nanotube arrays of FTO and UV-VIS diffuse transmittance spectra

(a) Camera image of Zn-TNTA on FTO. Note that the transparent area in the middle is the TNTA; surrounding it is titanium. FTO glass was left exposed to allow for electrical contact during anodization. The area of the TNTA shown is 1.8 cm^2 (b) UV-Vis diffuse transmittance spectrum of TNTA fabricated on FTO Glass

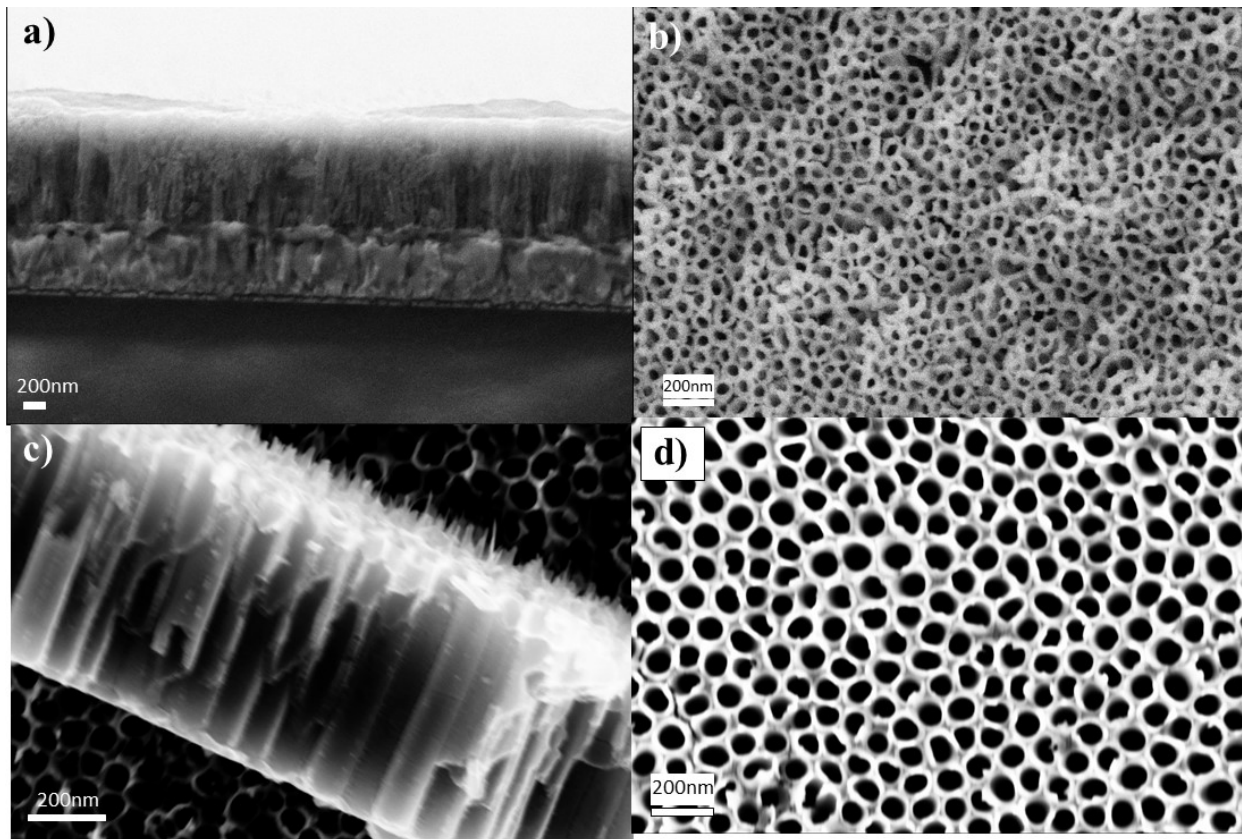


Figure 2-4: FESEM images of anodized TiO_2 nanotubes.

(a) the cross section of nanotubes grown on FTO glass, (b) the tops of nanotubes grown on FTO glass using 1 % water-containing electrolyte (c) a cross section of nanotubes grown on Si that were found on their side on top of the ordered TNTA, having delaminated during handling, and (d) the tops of nanotubes grown on Si using a 4 % water-containing electrolyte.

Preferred orientation was semiquantitatively evaluated by comparing intensity ratios of the XRD peaks of the anatase TiO_2 nanotubes using a $\theta - 2\theta$ scan; this is shown in Figure 2-5a-b. This semiquantitative approach allowed for quick feedback of the degree of preferential orientation by comparing relative peak intensity. It should be noted here that this method does not take into account the effects of anisotropic grain size of the crystallites that occur in 1D nanostructures, nor the effects of nanotubes grown at a slight skew angle relative to the substrate (121, 132); however, the technique is suitable as a relative comparison between TNTA sample. The (101), (004), and (200) peaks—located at $2\theta \approx 25^\circ$, 38° , and 48° respectively—are particularly useful for this

comparison. A preferred orientation is correlated with a decrease in the (101) and (200) peaks, and an increase in the (004) peaks. In fact, when superior preferred orientation is achieved, the (200) peak can disappear entirely; consequently, the intensity ratio of the (004) and (101) peaks (or $I_{(004)}/I_{(101)}$) is considered. An important note must be made for Figure 2-5a, however—the (200) peak of the underlying FTO very closely overlaps with the (004) peak of anatase. Thus, the intensity ratio cannot be used for comparing TNTAs grown on FTO, and only the relative intensities of the (101) and (200) peaks of TiO_2 can be considered.

The importance of water content of the anodizing electrolyte and the effect of the zinc electroreduction process was investigated. Figure 2-5c compares peak intensity ratios across both the water content of the electrolyte, and nanotubes annealed with and without zinc incorporation on a silicon wafer; a 7-second Zn doping process was used for the samples investigated here. Too high a electrolyte water content led to a decrease in preferential orientation, as shown by the low $I_{(004)}/I_{(101)}$ value of 0.3 when using 4 vol % water content; this intensity peak ratio is identical to one obtained when analyzing powder anatase. A maximum $I_{(004)}/I_{(101)}$ of 4 is observed when using a 1 vol% water content; however, any lower a water content and the morphology of the TNTA is severely impacted. Preferred orientation is universally increased when zinc is incorporated into the nanotubes, although at 4 vol % the intensity ratio method cannot differentiate between Pristine TNTA and Zn-TNTA (we describe a more precise method later). That samples made with 1 vol % water are more preferentially oriented than samples made with 1.5 or 2 vol % is somewhat surprising, given that 2 vol % was demonstrated to be superior when anodizing titanium foil (120). However, we note that our anodizations were conducted in ambient conditions rather than a glovebox; given the hygroscopic nature of ethylene glycol and ammonium fluoride, it is possible that our actual water content was slightly higher than we measure. It is also worth noting that it is

possible that the doping of Zn into the TNTA is presumably helped by the more irregular, non-close packed TNTA morphology occurring when a very low electrolyte water content is used. Because the nanotubes are not as close packed, Zn may be doped into the outer walls of the nanotubes more easily. This may allow for increased preferred orientation of grains throughout both the inner and outer surfaces of the nanotubes. Considering the morphology on TNTAs in general are quite tunable (diameter, wall thickness, tube packing, intertube spacing, and tube length) (36), it is worth giving attention to the nanotube morphology when performing electroreduction strategies to induce a preferential orientation.

Further insights into the effects of the Zn electroreduction process are gathered by an approximation of the Zn doping concentration by EDX analysis of TNTAs on Si after removal of ZnO flakes by HCl soaking. The approximate Zn doping in the TiO₂ is calculated by comparing the measured wt.% of Zn to the wt.% of Ti, assuming all measured Ti signal is obtained from stoichiometric TiO₂ and Zn is contained only within TiO₂; different Zn doping is obtained by changing the electroreduction process time. These results are shown in Figure 2-5d; as electroreduction process time is increased, Zn doping content increases to a point. The optimum level of Zn to obtain the best preferential orientation, achieving an $I_{(004)}/I_{(101)}$ of 12 at 1.5 wt.% Zn. That 1.5 wt.% is an optimal Zn content to achieve maximum preferred orientation agrees with previous literature (123). That a further increase in Zn content decreases preferential orientation probably occurs because Zn saturates the crystal facets it preferentially adsorbs to, which prevents optimal preferential orientation from being obtained. Furthermore, it is noted that from Figure 2-5c that the Zn electroreduction process only causes a dramatic increase in preferential orientation with nanotubes made using lower water electrolyte concentrations. This suggests that a proper hydroxyl ion content with the nanotubes is essential for the crystallization process to allow for a preferential

orientation, as it is in this step that crystallization is propagated through the nanotube; preferential growth of surface facets caused by the Zn process is thus secondary.

To gain an increased understanding of the effect of the Zn-incorporation on the preferred orientation of the TNTAs, we compared the XRD results collected by a 2D detector of Zn-TNTAs and pristine TNTAs on Si substrate with a consistent 4 vol. % H₂O electrolyte content; at this water content, the relative peak intensity method did not clearly resolve which TNTA state had greater preferred orientation, so it is chosen for further study. Figure 2-6 shows the setup used to acquire the XRD 2D frames, with angles defined on the figure and the relative orientation of the TNTA with respect to the XRD source and detector. The main advantage of the 2D detector used here over 0D/1D detectors is the simultaneous acquisition of diffractions at a wide range of χ ($\sim 60^\circ$) in one single frame, which provides a wealth of information on the texture of the sample under investigation (133).

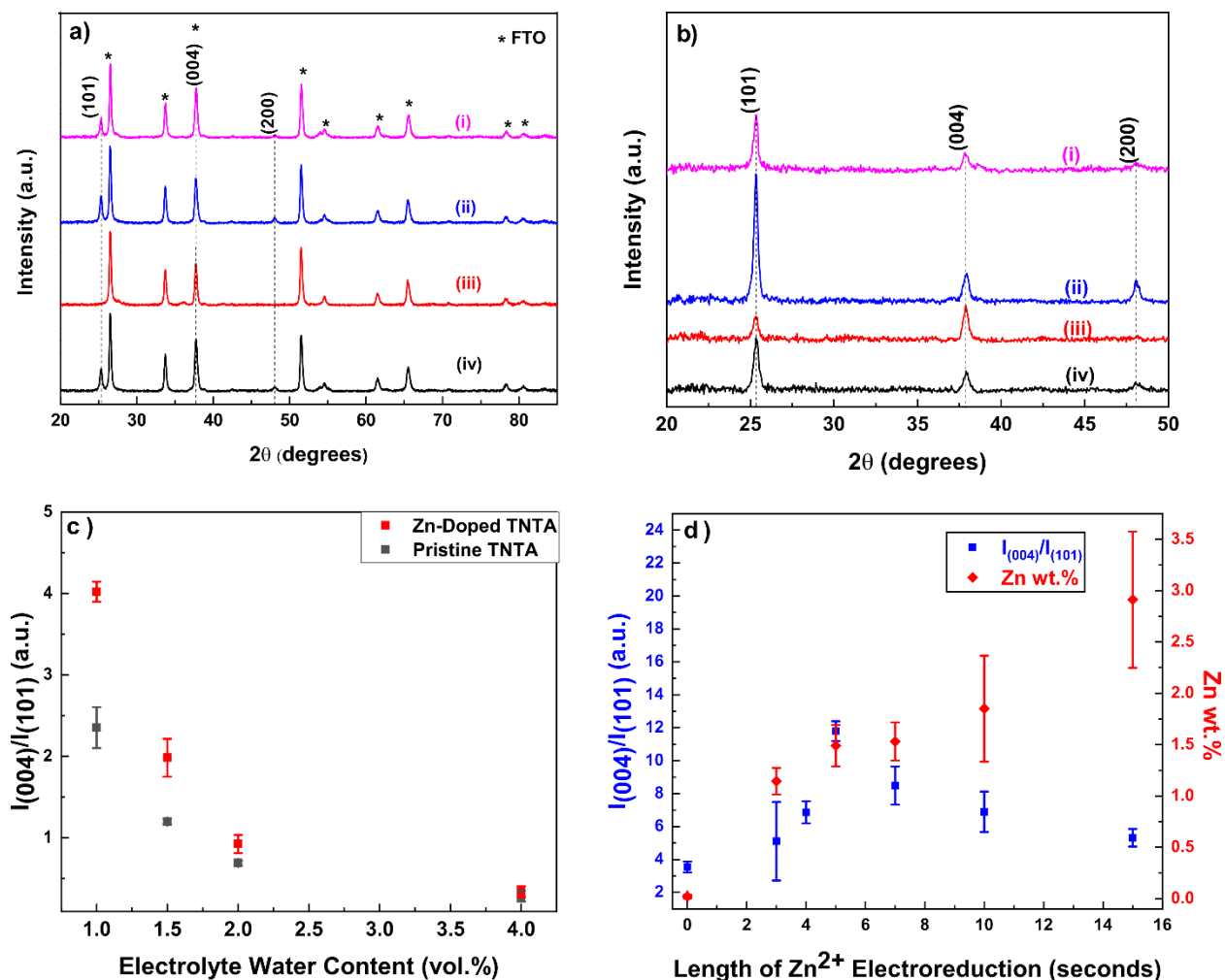


Figure 2-5: XRD patterns of TiO₂ nanotube arrays comparing preferential orientation

(a) FTO: glass and (b) Silicon in different electrolytes: (i) and (ii) using ethylene glycol with 4 vol % H₂O and 0.3 wt. % NH₄F; (iii) and (iv) using ethylene glycol with 1 vol % H₂O and 0.3 wt. % NH₄F. (i) and (iii) were doped with Zn prior to annealing, while (ii) and (iv) were pristine. All samples were subjected to 1 M HCl after annealing; (c) shows the intensity ratios on the y-axis obtained by dividing the intensity of the (004) plane by the intensity of the (101) plane for the Zn-TNTA and TNTA samples on silicon. The x-axis shows the utilized electrolyte water content. Data points are taken as the average of 3 samples, with error bars representing one standard deviation. (d) shows the intensity ratios of TNTA samples on the left y-axis as a function of the length of the Zn²⁺ electroreduction process used; the right y-axis displays the measured Zn wt.% content using EDX. Data points are each taken as the average of 3 spots across one sample, and error bars represent one standard deviation.

Figure 2-7a-b shows the 2D frames obtained via XRD, while Figure 2-7c depicts the intensity profile of the (004) diffraction peak ($2\theta = 37.7^\circ$) along χ . Figure 2-7d-e depicts the

intensities as a function of 2θ directly, obtained by integrating the intensities of these 2D frames over the 2θ range $22^\circ - 80^\circ$. A constant θ_{source} of 25° was used. These figures, taken together, support the hypothesis of the Zn incorporation increasing texture. As expected, most peaks disappeared in the 2θ scan for the Zn-TNTA, with a clear increase in the (004) peak; meanwhile, the 2θ scan for pristine TNTA more closely resembles that of randomly oriented powder anatase. The increased localized intensity distribution along χ that Zn-TNTA display is another signature for texture.

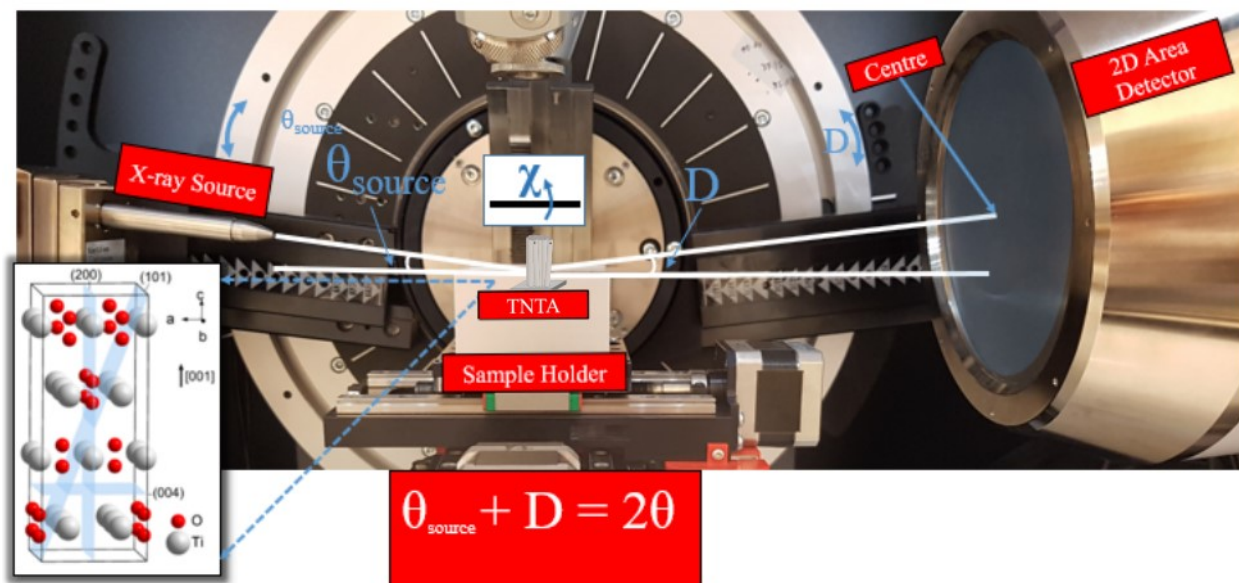


Figure 2-6: An image of XRD system used in this study

Labelled in the image are the angles referred to in the text and showing the relative orientation of the nanotubes with respect to the source and detector. Please note that χ as it is depicted here is rotated about an axis running from left to right on the page; a χ of 0° is would be pointed towards the top of the page, and the nanotubes would also point upwards with χ of 0° .

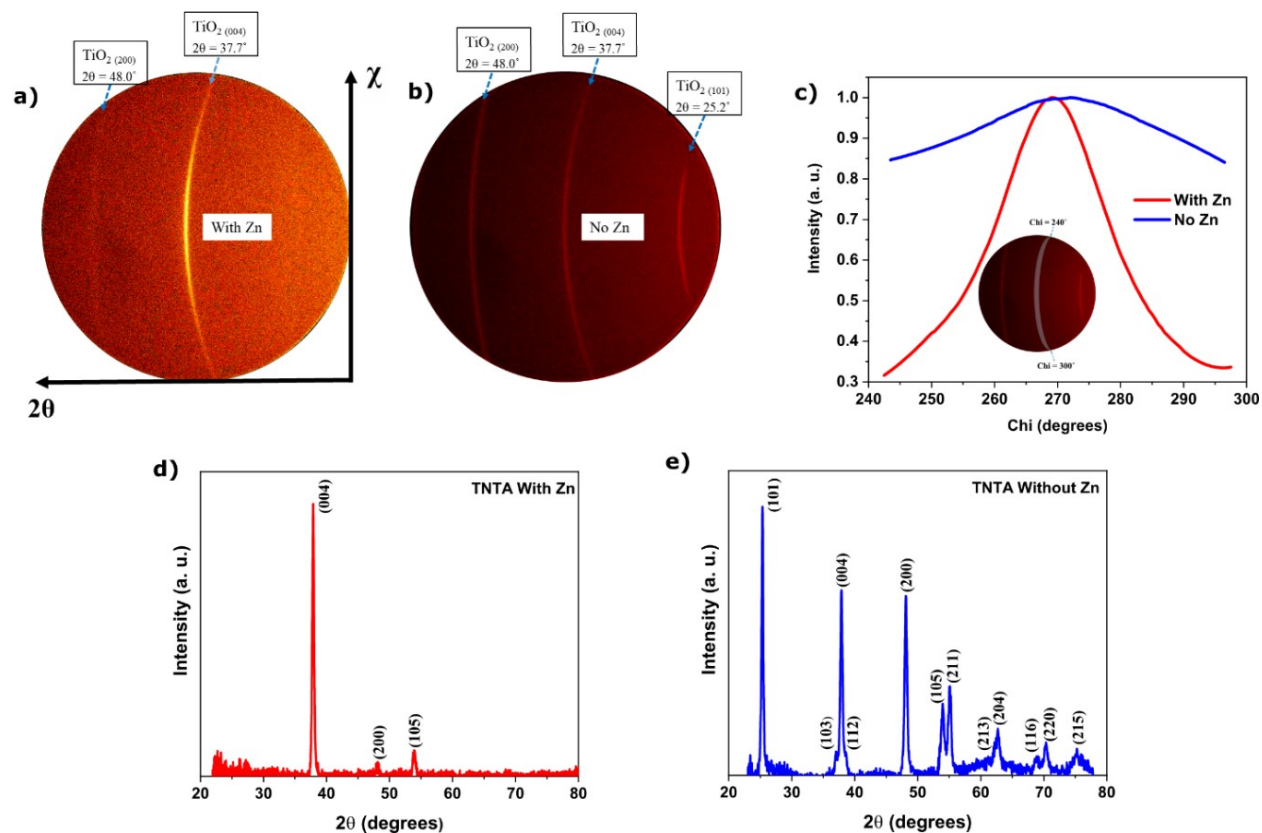


Figure 2-7: Investigations comparing the relative preferential orientation of Zn-TNTA and pristine TNTA. (a) XRD 2D frames of Zn-TNTA, showing the relative coordinate axes for XRD 2D frames used throughout this study. (b) XRD 2D frames of pristine TNTA. (c) Integrated intensity of the 2D frames at $2\theta = 37.7^\circ$ across χ for Zn-TNTA and pristine TNTA. The inset shows the area this was considered from (a) and (b). The integrated intensity of all 2D frames across 2θ is shown for (d) Zn-TNTA and (e) Pristine TNTA.

To confirm the texture achieved with Zn process, we acquired 2D frames while tilting samples at $\chi = 68.3^\circ$, which is the angle between the (004) and (101) planes, as shown in Figure 2-8. Assuming c -axis oriented TNTA, the (101) plane would now be in the position to satisfy Bragg's diffractions, and thus appear more strongly. As expected, the (004) diffraction peak disappeared completely in the Zn-TNTAs, while the (101) plane showed a markedly higher intensity; however, in the pristine TNTAs, the (004) could still be faintly seen while the (101) peak showed a lessened intensity. Thus, we conclude that the Zn process we utilized does indeed produce an increased preferred orientation.

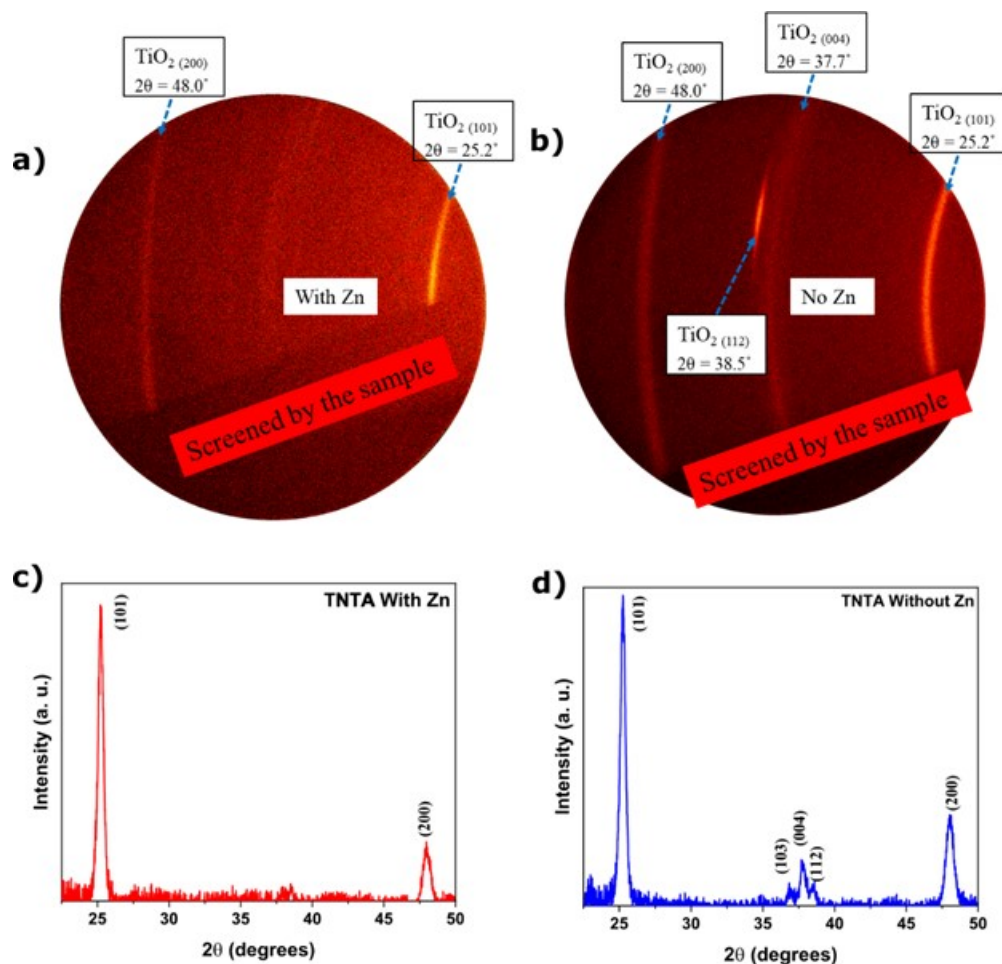


Figure 2-8: XRD 2D frames of TiO_2 nanotube arrays with the sample rotated at $\chi = 68.3^\circ$

(a) Zn-TNTA and (b) Pristine TNTA. Integrated intensities across the entire 2θ range are shown for (c) Zn-TNTA and (d) Pristine TNTA.

The impact of initial titanium roughness on the resultant preferred oriented nanotubes was investigated through AFM. As noted earlier, Seong et al. (122) demonstrated that when anodizing Ti foil substrates, preferred orientation is partly dependent on roughness, where a smoother foil meant greater preferred orientation. We were thus interested in the relevance of this idea to TNTAs grown on the non-native substrates, namely FTO: glass slides and Si wafers. The topography for both is shown in Figure 2-9. The Ti film on FTO glass was indeed rougher than the Ti film on the Si wafer, with root-mean-square roughness (S_q) values of 39.1 nm and 5.9 nm, respectively. This

difference is caused by the underlying substrates themselves, as FTO glass is much rougher compared to a Si wafer. However, it is also worth noting that the roughness of the formed nanotube arrays on each substrate were much closer in value, with an S_q value of 45.3 nm for Ti on FTO Glass and 41.1 nm for Ti on Si; the roughness of the tops of the nanotubes is influenced by anodization and post-anodization etching. For TNTAs on FTO, when optimal 1 vol % water content electrolyte and Zn incorporation is performed, not only does the (200) peak disappear from the XRD pattern, but the (101) peak is diminished to the point that anatase cannot be directly seen from the XRD pattern. Assuming that preferred orientation of TNTA on non-native substrates is dictated by the same principles as TNTAs grown directly on Ti, the increased preferred orientation of TNTAs on FTO versus Si is surprising given that a rougher Ti film is deposited on FTO glass. We offer two possible theories for this result. First, it is important to recognize that it is expected that a rougher surface leads to less preferential orientation ultimately because of weaker local electric fields caused by irregular pore formation. However, in the case of our sputtered Ti films, pore formation begins at the interface between sputtered grains. As films on both substrates were sputtered at the same conditions, we can expect that pore formation, and thus local electric fields, would be relatively similar for both substrates. Second, there exists more lattice mismatch between the TiO_2 and Si compared to TiO_2 and FTO. The lattice constant of Si (5.43 Å) is considerably higher than spray deposited FTO on glass ($a \approx 4.79$ Å, $c \approx 3.39$ Å) (134, 135). While anatase TiO_2 has 2 lattice constants ($a = 3.78$ Å and $c = 9.51$ Å), if the TiO_2 was perfectly preferentially oriented so that the [001] axis is perpendicular to the substrate, it would follow that only the former lattice constant is considered. There is a less than 12 % lattice mismatch between a in anatase and c in FTO: glass. More strain would occur between the TiO_2 and the underlying Si wafer substrate due to increased lattice mismatch—it is then less favorable for a grain at or near the TiO_2 -substrate

interface to be preferentially oriented. This effect may propagate through the grains in the TiO_2 barrier layer and into the nanotubes themselves.

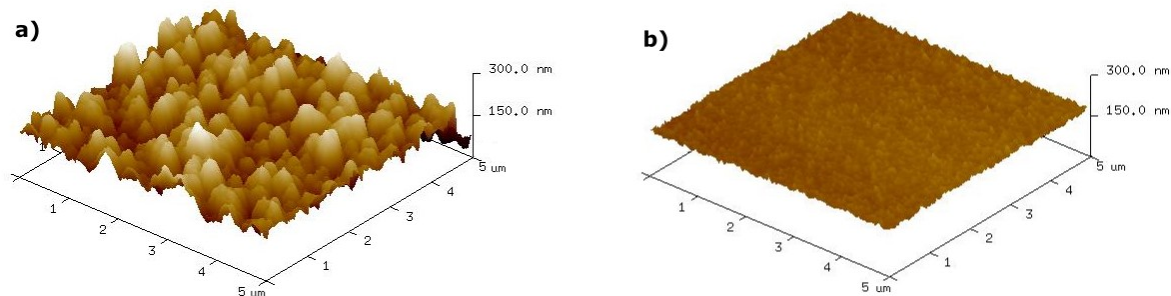


Figure 2-9: Three-dimensional AFM topographical images of sputtered Ti (a) on FTO Glass and (b) on an Si wafer

2.3.2 Effect of preferred orientation on carrier transport and recombination processes in TNTAs

In this report, we have shown that a post-anodization zinc treatment enhances preferential [004] orientation of TiO_2 nanotubes but also leaves remnant zinc atoms in the TiO_2 nanotube walls that are not completely removed by a hydrochloric acid treatment. We thus have utilized steady-state and transient photoconductivity measurements to understand the effect of zinc doping and film texturing on the optoelectronic properties of anodic TiO_2 nanotube arrays to establish a further benchmark for how they may be utilized in future device applications; we also demonstrate Zn-doped TNTAs in halide perovskite solar cells in the next section. The current-voltage plots and steady-state photoconductivity behavior of four types of TNTAs under bandgap illumination are shown in Figure 2-10. All the samples display conductivity and photoconductivity plots that are symmetric about the $V = 0$ axis, indicating that the electrode contacts are ohmic. Somewhat unexpectedly, the less textured TNTA-4% sample (black curve in Figure 2-10a) is more conductive than the highly textured TNTA-1% sample (green curve in Figure 2-10a), with the

TNTA-4% sample exhibiting a dark current that is nearly 5 times that obtained using the TNTA-1% sample. Following the incorporation of Zn atoms through the post-anodization zinc treatment, the dark conductivity of both the textured and non-textured samples improves substantially as seen by the increased conduction shown by the Zn-TNTA-1% (purple curve in Figure 2-10a) and Zn-TNTA-4% (sky blue curve in Figure 2-10a) samples. Figure 2-10b shows a linear increase in the photocurrent vs applied bias for the TNTA-4 %, Zn-TNTA-1% and Zn-TNTA-4% samples, which is typical of secondary photoconductivity. In secondary photoconductivity, the quantum efficiency (more commonly known as the photoconductive gain G_{ph}) can be significantly higher than unity since the photogenerated majority carrier can make several round trips between the contact electrodes in the time taken by the photogenerated minority carrier to be extracted by the contact electrodes (136). At applied bias values of roughly 5 V, the photocurrents for the TNTA-4 % and Zn-TNTA-4 % plateau; such saturation is a signature of complete minority carrier extraction (“sweep-out”) which results when the minority carrier transit time becomes lesser than or equal to the minority carrier lifetime. In this saturation regime, the photoconductive gain G_{ph} becomes a constant dependent only on the ratio of the mobilities of majority and minority carriers (137). In the steady-state plot shown in Figure 2-11a, the region encompassing 0.01–0.7 V is clearly ohmic as the slope of the $J-V$ log-log plot is 1; here, there is a low concentration of mobile charge carriers with the remainder being trapped. At higher applied voltages, the slopes increase to $\sim 1.5-3$ as traps begin to fill. From the ohmic region, by knowing the approximate length of the nanotubes (~ 800 nm) the conductivities for each sample can be calculated according to:

$$J = \frac{\sigma V}{l} \quad (2-1)$$

Where J is the current density, σ is the conductivity, V is the applied voltage, and l is the length of the nanotubes. An estimate of the mobility-lifetime product can be obtained from:

$$\Delta\sigma = \frac{eI\alpha\phi}{h\nu}(\mu_n\tau_n + \mu_p\tau_p) \quad (2-2)$$

Where $\Delta\sigma$ is the change in conductivity from dark to light conditions, e is the elementary charge, I is intensity of the incoming light, α is the absorption coefficient of the material, ν is the frequency of incident photons, ϕ is the quantum efficiency of the carrier generation process (assumed to be unity in the absence of excitonic effects), $\mu_{n,p}$ is the average drift mobilities of electrons or holes, and $\tau_{n,p}$ is the average lifetime of electrons or holes. Together, the term $(\mu_n\tau_n + \mu_p\tau_p)$ describes the mobility-lifetime product, which describes the sensitivity to photoexcitation and is considered a key figure of merit for photoconductors (138). Based on the absorption coefficient of anatase TiO₂ of 6090 cm⁻¹ (139), and the conductivity of the ohmic region in the steady-state photoconductivity plots, the mobility-lifetime products of the samples were calculated and are listed in Table 2-1. It is seen that the μ - τ product is correlated with the dark conductivity of the TNTA samples – that photoconductivity decreases as the dark Fermi level moves deeper into the bandgap has also been reported for other photoconductors (138). From the transient plots shown in Figure 2-11b, the time-dependent photoconductivity was fitted to a biexponential decay to yield time constants τ_1 and τ_2 (140). Parameters obtained from Figure 2-10 are reported in Table 2-1. Using the data in Figure 2-10, the responsivity of TNTA-4% for ultraviolet photodetection was determined to 523 A/W at a bias of 2 V, which is an order of magnitude higher than the UV responsivity of TNTA-1% (36.5 A/W) and the responsivity of 13.6 A/W reported by Marzari et al. (141) and almost two orders of magnitude higher than the UV responsivity of ~ 6 A/W reported

by Jacobsen et al. (142) at similar bias values, placing it among the highest photodetection performance values reported to date for stand-alone TNTAs.

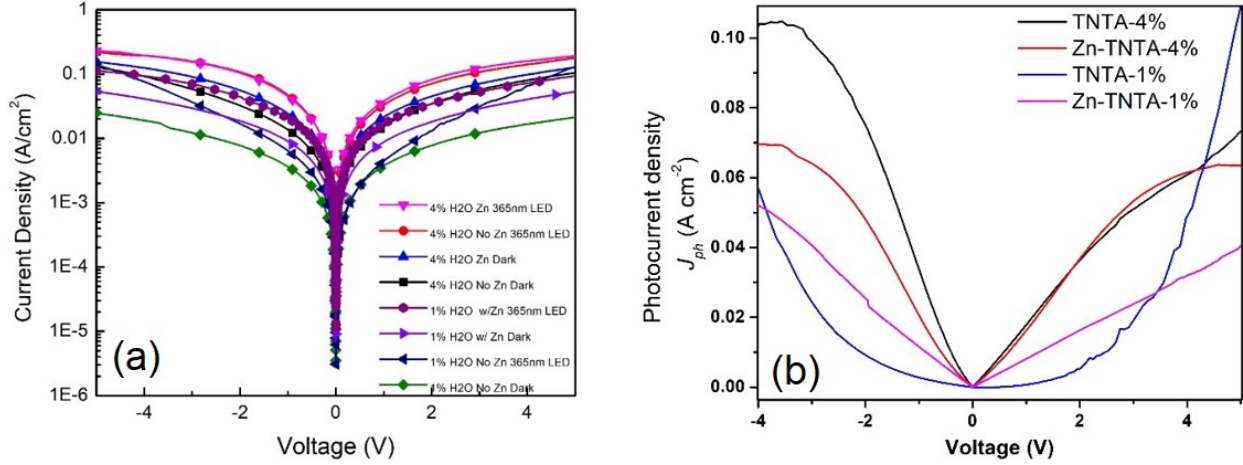


Figure 2-10 (a) Experimental current-voltage curves of TNTA-1%, Zn-TNTA-1%, TNTA-4% and Zn-TNTA-4% samples under dark and 365 nm illumination and (b) Photocurrent-bias curves for the same samples.

All curves are constructed of a minimum of 200 data points.

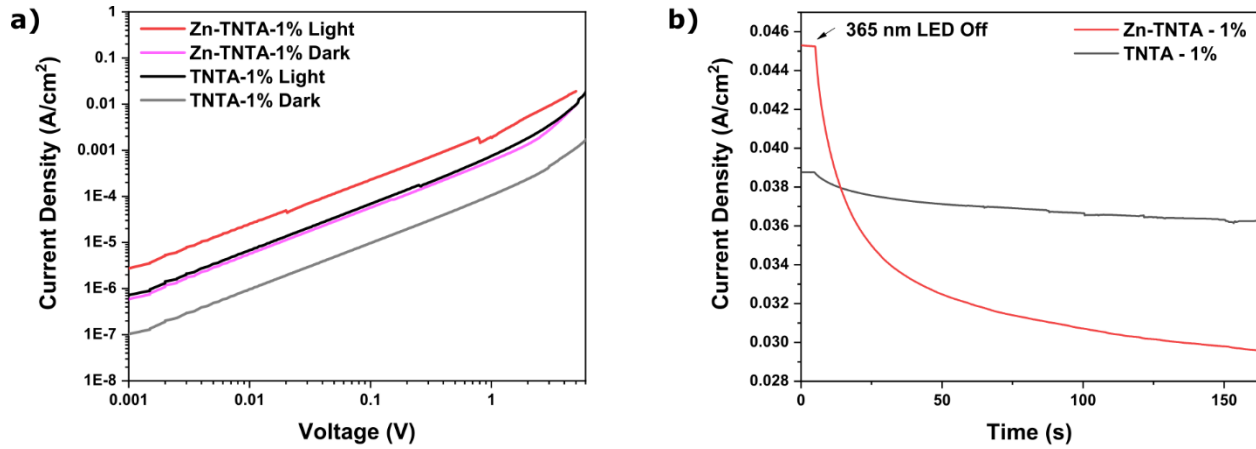


Figure 2-11: (a) Experimental current-voltage curves on Zn-TNTA-1% and TNTA-1% samples under dark and 365 nm illumination. (b) Experimental current-time curve showing photoconductive decay of Zn-TNTA-1% and TNTA-1% samples under a 2V bias.

All curves are constructed of a minimum of 500 data points.

Table 2-1: Parameters of TNTAs obtained from steady-state and transient photoconductivity

Sample	σ_{dark} (S cm ⁻¹)	σ_{light} (S cm ⁻¹)	$\Delta\sigma$ (S cm ⁻¹)	Mobility-lifetime product (cm ² V ⁻¹)	τ_1 (s)	τ_2 (s)
TNTA-1%	8.0×10^{-9}	5.5×10^{-8}	4.7×10^{-8}	2.1×10^{-7}	11.0	551.0
Zn-TNTA-1%	1.1×10^{-6}	1.8×10^{-6}	6.4×10^{-7}	2.5×10^{-6}	8.0	55.1
TNTA-4%	2.1×10^{-6}	5.5×10^{-6}	3.4×10^{-6}	1.3×10^{-5}	6.4	44.2
Zn-TNTA-4%	2.7×10^{-6}	4.9×10^{-6}	2.2×10^{-6}	8.6×10^{-6}	2.8	55.0

Further insight into the Zn doping process and effects of preferential orientation may be gleaned from Figure 2-10 and Figure 2-11 with respect through their photoconductivity lifetimes, as given quantitatively in Table 2-1. It is seen that all the TNTA samples exhibit a lifetime component of ~2 - 11 s. We note that these nanotubes, annealed at 500 ° C for 3 hours, nevertheless all display lifetimes much lower than those reported that were annealed at 350° C, which still have amorphous regions in the nanotubes which act as a source of traps and thus exhibit lifetime components of 100-200 s, 1000-3000 s and 20,000-100,000 s respectively in their photoconductivity decay following bandgap illumination (143, 144). The TNTAs studied in this report, having been annealed at 500 ° C for 3 hours, which is generally agreed to significantly reduce the amount of any uncrystallized TiO₂. In addition, the Zn-TNTA-1%, TNTA-4% and Zn-TNTA-4% samples also exhibit a lifetime component of ~ 50 s in their photoconductivity decays, while the TNTA-1% samples alone displayed an anomalously low dark conductivity as well as a longer lifetime component of ~ 550 s, not seen in the other samples. Our results resemble those of Rodriguez et al. (145), who observed two decay constants of 2 s and 78 s, respectively in the photoconductivity decay of anodically formed TiO₂ nanopores on Si wafer substrates annealed at 550 °C. Rodriguez et al. (145) attributed their photoconductivity data to the formation of Schottky barriers between adjacent crystallites due to the depletion of electrons close to the grain surface by molecular oxygen in air. Our results indicate that the TNTA-1% samples experience the greatest

depletion of majority carriers due to oxygen molecules adsorbed on the surface (resulting in steep inter-grain potential barriers), thus causing the TNTA-1% samples to have the lowest conductivity among the samples studied. Due to their strong [001] preferred orientation, the TNTA-1% samples have far fewer exposed {001} facets compared to the other samples, which leads to the key insight that the adsorption of molecular oxygen concomitant with electron trapping is weakest on {001} facets. We would also like to note that Figure 2-12 shows that the zinc-doped TNTA samples exhibit a pronounced photoresponse under visible light illumination. Zinc doping of TiO_2 has been reported to narrow the bandgap of titania, and increase its visible light photoresponse and also improve photocatalytic activity (146-148). There is even some theoretical support for bandgap narrowing in TiO_2 due to zinc doping (149).

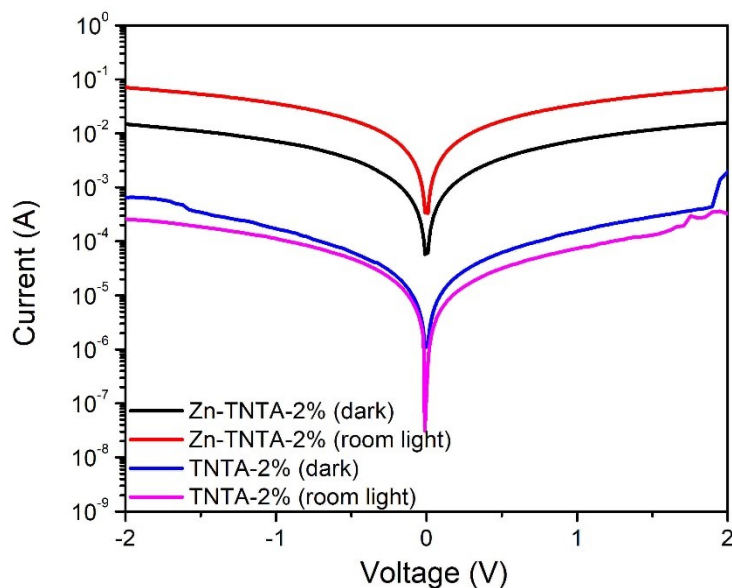


Figure 2-12: Experimental current-voltage curves of TNTA-2% and Zn-TNTA-2 % samples in the dark and in room light.

2.3.3 Effect of preferred orientation on the performance of halide perovskite solar cells that use TNTA electron transport layers

With the ability to produce these preferentially oriented TNTAs on non-native substrates, we sought to test this configuration in photovoltaics. Using 300 nm long TNTAs synthesized on FTO-coated glass as the electron transporting layer, we fabricated halide perovskite solar cells. We considered both pristine TNTA and Zn-TNTAs made using 1, 2 and 4 % electrolyte water content; the current voltage characteristics of champion solar cells are shown in Figure 2-13, while the average open-circuit voltage (V_{oc}), short-circuit current density (J_{sc}), fill factor (FF), and power-conversion efficiency (PCE) of each are shown in Table 2-2; the champion solar cell performance of each type is shown in Table 2-3. The averages were calculated from measurements of 6 solar cells for each of the 6 sample types, with the exception of the Zn-TNTA-4% sample, which experienced a number of failed cells and only the average of 3 measurements is considered. Two key observations should be apparent: (i) as electrolyte water content is lowered and preferential orientation increases, PCE increases and (ii) that doping of Zn into the lattice of TiO_2 uniformly decreased PCE. That lowering electrolyte water content increases PCE makes sense, as there is an increased preferential orientation that is expected to improve electron transport and charge extraction from the solar cell while the lower carrier concentration in the TNTA-1% samples is expected to suppress recombination between electrons in TiO_2 and holes in perovskite.

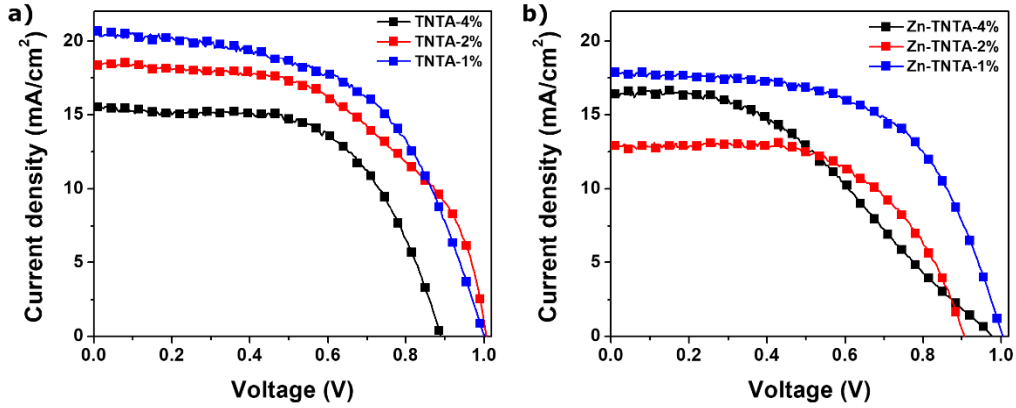


Figure 2-13: Experimental current–voltage characteristics under AM1.5 G one sun illumination of perovskite solar cells

Based on (a) pristine TNTAs and (b) Zn-TNTAs anodized with different electrolyte water concentrations.

Table 2-2: Photovoltaic performance of perovskite solar cells with TNTA prepared using different electrolyte water concentrations, and with and without Zn incorporation. All parameters are shown \pm one standard deviation.

Sample–Electrolyte Water Content	V_{oc} (V)	J_{sc} (mA/cm ²)	FF	PCE (%)
TNTA–1%	0.96 ± 0.03	20.4 ± 0.5	0.54 ± 0.02	10.5 ± 0.6
Zn-TNTA–1%	0.96 ± 0.02	17.3 ± 0.5	0.54 ± 0.04	9.0 ± 0.1
TNTA–2%	0.91 ± 0.04	17.4 ± 3.0	0.57 ± 0.06	9.0 ± 1.2
Zn-TNTA–2%	0.88 ± 0.03	11.0 ± 2.1	0.58 ± 0.03	5.7 ± 1.3
TNTA–4%	0.88 ± 0.02	12.4 ± 2.8	0.56 ± 0.05	6.1 ± 1.5
Zn-TNTA–4%	0.97 ± 0.01	15.4 ± 1.9	0.38 ± 0.04	5.7 ± 1.4

Table 2-3: Champion photovoltaic performance of perovskite solar cells with TNTA prepared using different electrolyte water concentrations, and with and without Zn incorporation

Sample–Electrolyte Water Content	V_{oc} (V)	J_{sc} (mA/cm ²)	FF	PCE (%)
TNTA–1%	1.00	20.7	0.55	11.39
Zn-TNTA–1%	1.00	17.7	0.59	10.50
TNTA–2%	1.01	18.5	0.54	10.04
Zn-TNTA–2%	0.91	13.2	0.59	6.97
TNTA–4%	0.89	15.4	0.61	8.24
Zn-TNTA–4%	0.98	16.5	0.40	6.50

That Zn-TNTA decreases PCE is would be unexpected if the only effect taking place is the increased preferential orientation of crystallites. However, the Zn²⁺ doped into the TiO₂ lattice is also expected a role in increasing the amount of visible light absorbed. The absorption of visible light by Zn-doped TiO₂ samples is parasitic; photogenerated holes in Zn-doped TiO₂ are likely to be trapped or else experience geminate recombination (in TiO₂) or bimolecular recombination (in the perovskite) on their way to the gold electrode. Furthermore, the photons absorbed by TiO₂ are not absorbed in the perovskite layer and result in a decreased separation between the quasi-Fermi levels in the perovskite active layer. This behavior is evident in the action spectra of the solar cells, in Figure 2-14. Figure 2-14a shows that three different solar cells made using Zn-TNTA-1% samples each exhibit lower external quantum efficiencies (EQEs) for visible photons than solar cells made using TNTA-1% samples as the ETL. Figure 2-14b plots the difference in quantum yield of the solar cells made using Zn-TNTA-1% and TNTA-1% as the ETLs.

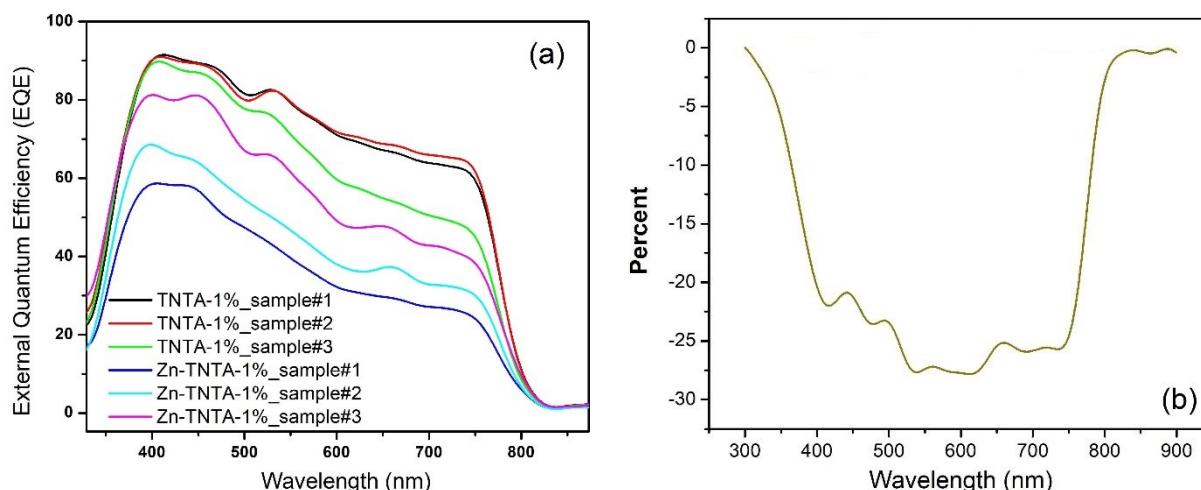


Figure 2-14: (a) Action spectra showing the external quantum efficiency (EQE) of halide perovskite solar cells constructed using TNTA-1% samples and Zn-TNTA-1% samples as the electron transport layers and (b) Percent difference spectra of the average EQE of solar cells made using Zn-TNTA-1% ETLs compared to the average EQE of solar cells made using TNTA-1% ETLs.

It is conceivable that an optimum Zn doping concentration exists to maximize device performance. Wu et al. reported an improved J_{sc} and PCE using Zn-doped TiO_2 as the electron transporting layer in a perovskite solar cell when Zn dopant is below 7 at.%, with the increased performance attributed to improved electrical conductivity and charge separation efficiency (150). However, Huang et al. reported an improvement in efficiency of a dye-sensitized solar cell using Zn-doped TiO_2 when Zn concentrations were below 1 at.%, with decreases in efficiency at higher Zn concentrations attributed to increased electron-hole recombination (151). While a more precise quantification of the optimized Zn doping concentration of transparent TNTA for solar cell performance via the electrochemical reduction method was not attempted in this study, it stands to reason that precise control of primary factors such as the length of the electrochemical reduction process and ZnSO_4 concentration in the electrolyte are critical, alongside secondary factors such as surface area of the anode/cathode, distance between the anode/cathode, and underlying conductivity of the substrate (123). We would also like to note that other elements may be able to

induce the preferential orientation effect; for example, Sierra-Uribe et al. has recently demonstrated a preferred orientation using Na instead of Zn (152). Clearly, there is room for further work in the area of electroreduction of TNTA to induce preferential orientation.

2.4 Chapter Conclusion

Here again are the research sub-questions asked in this chapter, which contribute to the major research question, “What are the effects of conducting novel anodization techniques on sputtered non-native substrates?”:

1. Can preferential orientation of TiO₂ nanotubes on non-native substrates be obtained?
2. How do required or optimal synthesis conditions compare to foil when attempting to obtain preferentially oriented nanotubes on non-native substrates?
3. How do the properties of preferentially oriented nanotubes compare to conventional randomly oriented ones?

We have demonstrated that preferential orientation can be initiated in TNTAs fabricated from sputtered Ti films in a similar, but not identical, manner to TNTAs grown on native Ti foils and that electrolyte water content, a possible electroreduction process, surface roughness, and the quality of the sputtered Ti film must be taken into consideration. A maximum preferential orientation, evaluated as a $I_{(004)}/I_{(101)}$ value of 12, is observed when using an electrolyte water content of 1 vol % and a obtaining a Zn doping content of 1.5 wt.%. For pristine TNTAs a decrease in electrolyte water content increases the preferential orientation, and we observed an increase in halide perovskite solar cell performance when using the TNTA as an electron transport layer. A 1

vol % water electrolyte corresponding to TNTAs with a $I_{(004)}/I_{(101)}$ of 2.3 led to an average PCE of 10.5% PCE, while a 4 vol% water electrolyte corresponding to TNTAs with a $I_{(004)}/I_{(101)}$ of 0.3 led to an average PCE of 6.1% PCE. Zn-doped TNTAs uniformly exhibited a poorer solar cell performance compared to undoped TNTA samples when used as the electron transport layer in halide perovskite solar cells; for example, using a 1 vol.% water electrolyte, a Zn-TNTA corresponding to a $I_{(004)}/I_{(101)}$ of 7 only achieved an average PCE of 9.0%. Thus, we conclude that the electrochemical reduction method used to instigate Zn-doping presents a powerful method to control preferential orientation but needs to be carefully controlled lest device performance be negatively affected by the doping material itself. Based on the remarkably diminished (101) and (200) peaks in XRD for TNTAs produced on the relatively rough FTO compared to the still-present peaks for TNTAs produced on the smooth Si surface, surface roughness appears to be less important for preferential orientation in TNTAs fabricated on non-native substrates, but instead the material the substrate is comprised of is of importance. In addition to our characterizations and solar cell fabrication, we also measured the photoconductivity behavior of TiO₂ nanotube array samples as a function of electrolyte water content and Zn doping. Somewhat unexpectedly, the least oriented TNTA samples grown using a high electrolyte water content with weaker preferential orientation exhibited the strongest photoconductive response, which attributed to Zn serving as recombination centers and {001} facets adsorbing ambient oxygen, increasing the number of recombination centers. The values of the mobility-lifetime product (as high as $1.3 \times 10^5 \text{ cm}^2 \text{ V}^{-1}$) and photodetection responsivity for ultraviolet photons (as high as 523 A/W at a bias of 2 V) reported in this work are among the highest ever reported for TiO₂ nanotube arrays.

Chapter 3: Nanoporous NiO on Non-Native Substrates

The work presented in this chapter is based on a published journal article. Reprinted with permission from Springer Nature Customer Service Centre GmbH: Springer Nature (153).

3.1 Chapter Introduction

Transparent semiconducting oxides are an important class of compounds for use in electronic applications such as solar cells, photocatalysis, transistors, sensors, and displays (154-158). However, owing to the electronic configuration of oxides, the majority of available transparent semiconducting oxides are n-type as opposed to p-type; furthermore, available n-type transparent oxides are higher performing owing in part to their generally higher charge mobilities (159). Nanostructuring the oxide layer is particularly important in photodetectors, photocatalyst, and photoelectrochemical sensors to obtain high surface area electronic heterojunctions and to overcome the trade-off between light absorption and charge separation in light harvesting devices (160, 161). Surface traps in nanostructured metal oxides are another important factor; while traditionally viewed negatively, they have also been shown to be beneficial in photodetection, photocatalysis, and sensing (144, 162, 163). In n-type semiconducting oxides such as ZnO, TiO₂, Fe₂O₃, Ta₂O₅, Nb₂O₅ and WO₃, electrochemical anodization and solvothermal growth techniques have been used to achieve nanotube, nanopore, and nanorod arrays with a high degree of control over the morphology of the metal oxide (2, 108, 164-172). For p-type metal oxides, a similar degree of morphological control has been lacking. This has meant that many potential applications and device architectures are currently unfeasible or impractical, and there is a need for new and improved p-type materials. One possibility is NiO, which is a p-type oxide semiconductor that has been especially investigated for use in areas such as a transparent photocathode for

photoelectrochemical systems (173) and as a hole transporting layer for solar cells (174). Conventional methods to prepare NiO include evaporation, direct magnetron sputtering sol-gel techniques, and electrodeposition (175, 176). However, anodization of Ni to form nanostructured NiO remains largely unexplored, with only two previous reports on the topic (46, 177). In each case, nanoporous NiO was investigated for use as a p-type photocathode with the goal of conducting water splitting. Besides contributing to the generation of photocurrent, it is also hoped that NiO or similar p-type materials could replace the expensive platinum and gold counter electrodes that are typically used in photocatalytic systems.

Both previous studies resulted in a nanoporous nickel oxide, after anodization and annealing of a Ni foil. However, to the best of our knowledge there are no studies exploring the anodization of thin films of Ni on non-native substrates. This configuration is critical to the formation of a wide variety of real-world devices because such a substrate may either be a platform for integrating devices (e.g. silicon wafers), or may need to be transparent to allow for light to pass through for the function of optoelectronic devices (such as the case for glass coated with a transparent conductive oxide). Therefore, in this study, we have conducted anodization on sputtered Ni films, which has resulted in nanoporous NiO. We further provide insight on the critical synthesis parameters during the sputtering and anodization processes and performed material characterization to quantify some of the properties of the anodized films.

3.2 Experimental Details

3.2.1 Sample Preparation

The substrates of FTO (fluorine-doped tin oxide)-coated glass, ITO (indium tin oxide)-coated glass, and <100> crystal axis, n⁺-type, As-doped silicon wafers were used as-purchased

from Hartford Glass Co., Guluo Glass and Kunshan Sino Silicon Technology Co. respectively. The FTO-coated glass had a sheet resistance of 8.2 ohms per square, the ITO-coated glass had a sheet resistance of 6.5 ohms per square, and the silicon wafer had a sheet resistance of 0.060 ohms per square. All pieces were cut to be approximately square with an area of about 5 cm² (referred to hereafter in this section as a “sample”). FTO-coated glass and ITO-coated glass were cleaned by a ultrasonication in acetone, methanol, and then deionized water 10 minutes each before drying under a nitrogen stream. Silicon wafers were immersed for in a piranha solution comprised of a 3:1 mixture of sulfuric acid and hydrogen peroxide for 15 minutes, immersed in a buffered oxide etch comprised of a 10:1 mixture of ammonium fluoride and hydrofluoric acid, and then rinsed with deionized water. A section of FTO and ITO samples around 0.8 cm² was covered using Kapton tape to prevent metal deposition in this spot and allow for direct electrical contact to the substrate during anodization; the same was not done for Si wafers, and electrical contact was made directly to the nickel. Sputtering of nickel was conducted for 10 minutes on all substrates in argon, with a power of 300 W, a deposition pressure of 4.5 mTorr, and substrate heating of 175°C to result in a film thickness of around 100 nm on top of the FTO or ITO coating. The Kapton tape was removed, and the exposed transparent conductive oxide attached via an affixed copper wire to a DC power supply. The sample was connected as the anode in an electrical circuit, with a 5mm diameter graphite rod as the cathode. The anode and cathode were spaced 3 cm apart in a 30 mL beaker filled with the electrolyte; the electrolyte compositions used, the applied current/voltage, and the length of anodization time are discussed in a later section. After anodization, each sample was removed, soaked in methanol, and then deionized water for 1 minute each, and dried under a nitrogen stream.

3.2.2 Characterization

Imaging of the anodized films was conducted using a Zeiss Sigma Field Emission Scanning Electron Microscope (FESEM). Pore size was determined from FESEM images by manually counting the diameter of 100 pores and is reported as the mean value \pm one standard deviation. X-ray Diffraction (XRD) patterns were collected using a Rigaku Ultima IV equipped with a Cu-K α source. Ultraviolet-visible (UV-Vis) spectroscopy was carried out using a Perkin Elymer Lambda 1050 Spectrophotometer equipped with a 100 mm integrating sphere. The sample was placed at the opposite end of the sphere from incoming light in front of a highly reflective Spectralon coating and diffuse reflectance was measured; with transmittance a non-factor as a result, sample absorption could be obtained. X-ray photoelectron spectroscopy was conducted using an Axis-Ultra (Kratos Analytical) instrument equipped with a monochromatic Al-K α source (15 kV, 50 W) under ultrahigh vacuum ($\sim 10^{-8}$ Torr). To adjust for charge correction, the spectra was adjusted so that the binding energy of the C 1s core level of adventitious hydrocarbons matched the standard binding energy value of 284.8 eV.

Electrochemical impedance spectroscopy (EIS) was performed using a three-electrode configuration at an applied voltage of -0.4 V vs the reference electrode Ag/AgCl in a pH 7, 0.1 M phosphate buffer solution comprised of 1 M K₂HPO₄ and 1 M KH₂PO₄ mixed together in a 61.5:38.5 volume ratio. Mott-Schottky plots were collected from impedance-potential measurements in the same 0.1 M phosphate buffer in the -0.6 to $+1.6$ V voltage range at 100 kHz frequency.

3.3 Results and Discussion

3.3.1 Effect of Synthesis Parameters on Anodized Film Morphology

The first step towards anodizing Ni thin films was the deposition of the film by sputtering. The key synthesis parameters selected here were inspired by prior studies conducted on anodizing Ti to form TiO₂ nanotubes, particularly on non-native substrates (75, 110, 178-186). For example, it is understood that a denser metal substrate leads to a more well-defined and ordered porous morphology when anodizing Ti (76, 94). In the context of DC magnetron sputtering, film density is primarily controlled by the sputtering gas pressure and substrate temperature as is well-understood by the Thornton model (74), where higher substrate temperatures and lower deposition pressures generally lead to a denser film. The sputtering system utilized here has a maximum achievable substrate temperature of 175°C, so that was selected. The lowest possible argon gas pressure of 0.6 Pa was utilized; we note that after experimentation with the sputtering system, it was found that any lower pressure would cause the plasma that is essential to the sputtering process to extinguish, as not enough collisions occur between gaseous particles to sustain the plasma.

The sputtered nickel thin films were anodized to result in a nanoporous nickel oxide film after annealing. This was accomplished by simultaneous oxide growth and oxide etching process that occur during anodization. While etching processes are desired to allow for a porous structure, too fast of an etching process would lead to complete removal of the films. An electrolyte comprised of 97 vol.% diethylene glycol (DEG), 3 vol.% deionized water, 0.15 M KOH, and 0.1 M NH₄F was found to produce the best porous structure; this is a modification of the recipe reported by Sapi et al. (177), although we used DEG instead of ethylene glycol (EG). The importance of each component in the electrolyte is described as follows: first, in an anodization

process to produce nanostructures, the electrolyte is often primarily based off an organic liquid with a small amount of water. While organic electrolytes donate fewer O^{2-} ions at the electrolyte/oxide interface, thus leading to slower oxide growth, the etching of the oxide is also decreased, allowing for thicker fully formed nanostructures (83). Thus, a small water content to supply some readily available O^{2-} ions is best. DEG increased the pore size from around 2-3 nm when using ethylene glycol (EG) to tens of nanometers—as can be directly compared between Figure 3-1a and Figure 3-2a which show the resultant morphology of EG and DEG-based anodization electrolytes respectively. The reason for the difference can be explained based on work conducted on large-diameter, widely spaced TiO_2 nanotubes using DEG-based electrolytes (187). Due the higher viscosity and lower ionic mobility in DEG, DEG-based electrolytes possess a lower conductivity than EG-based electrolytes for similar concentrations of water and fluoride ions. Consequently, the much higher potential drop across the electrolyte results in low electric field conditions across the barrier layer and at the barrier layer-electrolyte interface, leading to a low population of nucleation sites. In addition, field-assisted reactions responsible for oxide formation and etching are weaker, while chemical etching remains relatively constant. Since chemical etching is more isotropic than field assisted reactions, etching occurs more isotropically in DEG electrolytes, thus resulting in wider pores. In the case of nickel anodization, the resultant anodized material etches away too quickly in purely acidic solution to form a substantially thick nanostructured layer. The inclusion of KOH slows this process, to allow the morphology formed by the etching process to remain intact during anodization. We found that the temperature of the electrolyte is crucial this anodization process. Too high a temperature leads to a higher etching rate; as the etching process is itself exothermic, this can cause an avalanche effect and rampant etch rates, and a nanoporous structure did not result (shown in Figure 3-2b). For this reason,

anodization was conducted with the anodization vessel contained within an ice bath. For a similar reason, we found that galvanostatic anodization is preferred over potentiostatic anodization for the formation of nanostructured oxide. Upon applying a constant voltage, current densities initially decrease as an oxide layer is formed, followed by increase owing to pitting caused by etching. However, if current densities become too high, we noticed a similar avalanche effect of etching rates and increasing temperature; the morphology of anodized nickel using a potentiostatic process is shown in Figure 3-2c. It can be noted that the morphologies displayed by potentiostatic anodization in an ice bath and room temperature galvanostatic anodization display remarkable similarity.

SEM images of the anodized films using the optimized recipe are shown in Figure 3-1. The imaged layers are labelled as NiO for FTO samples, $\text{NiO}_x(\text{OH})_y$ on ITO samples, and NiO/NiSi for Si samples which is proven later. There are significant differences in morphology between each substrate. The NiO formed on FTO resulted in small pores (13.4 ± 2.8 nm diameter), and etching occurred preferentially at grain boundaries. Meanwhile, the NiO formed on ITO and Si had larger pore diameters of 24.4 ± 7.4 nm and 22.7 ± 4.6 nm, respectively. The ITO samples displayed much less preferential grain boundary etching than FTO samples, although the etched pores grew large enough to agglomerate in several locations; these locations resemble the structure of former grain boundaries, and it might be guessed that it is a small amount of preferential etching that caused this phenomenon. However, silicon samples displayed no preferential grain boundary etching. The primary reason for the difference in final NiO morphologies can be explained by the differing roughness of each substrate. As characterized by AFM (images of the AFM scans shown in Figure 3-3), the root-mean-square roughness (S_q) of the sputtered Ni film on FTO glass, ITO glass, and the Si wafer was 28.8 nm, 5.58 nm, and 2.42 nm respectively. It follows that the rougher a film is,

the more exposed grain boundaries there are. As grain boundaries undergo chemical reactions at a higher rate than elsewhere in the film microstructure, the etching-pitting environment for each substrate is different, and thus a different nanoporous morphology ensues. This mechanism also explains the general similarity of the morphologies of ITO glass to Si when one considers their relatively similar roughness, at least compared to that of FTO glass.

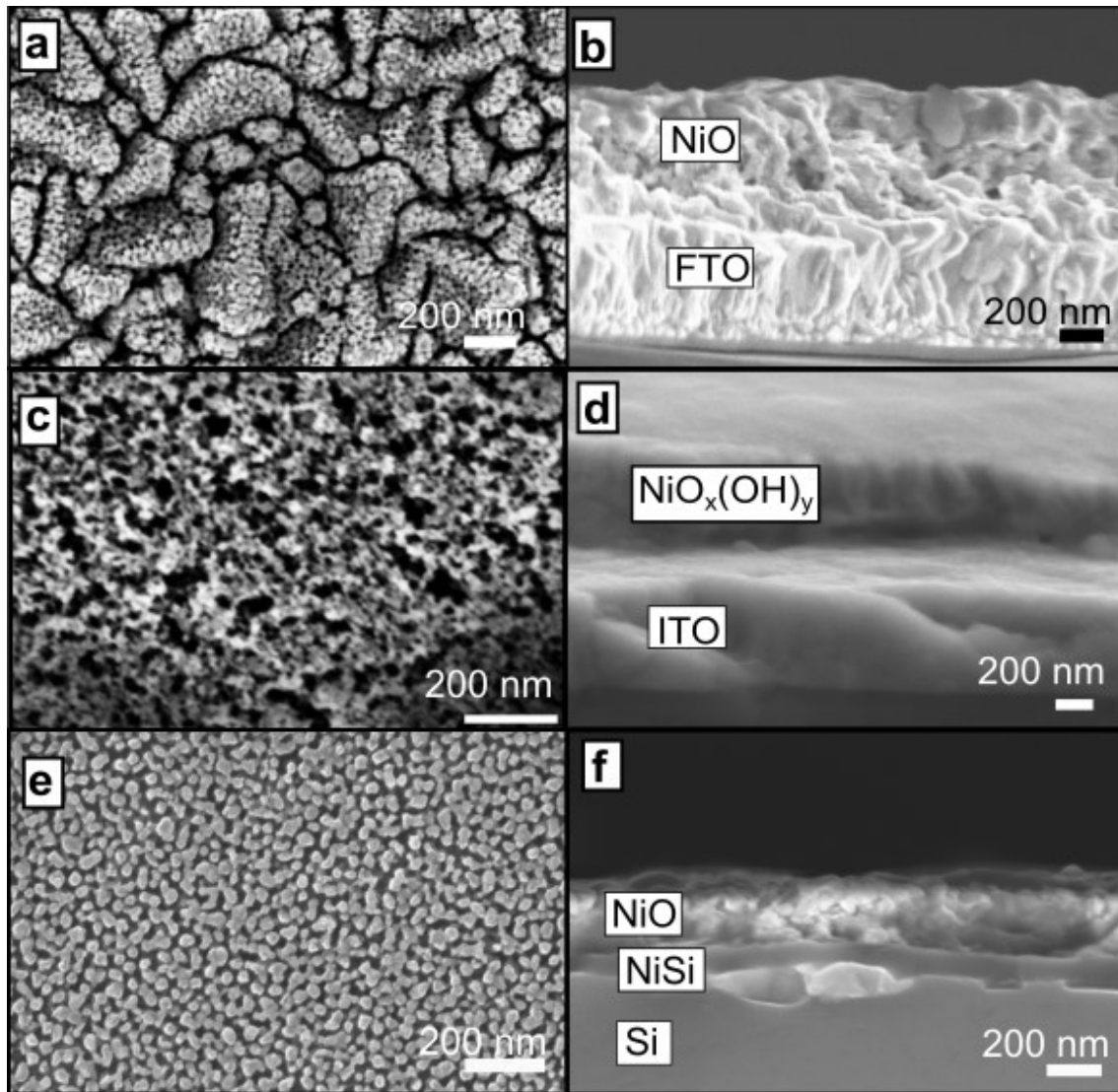


Figure 3-1: SEM images of nanoporous NiO film compared across substrates

(a), (b) FTO-coated glass, (c), (d) ITO-coated glass, and (e), (f) an Si wafer. (a), (c), and (e) show the films from a top-down perspective, while (b), (d), and (f) show the films from a cross-sectional view. All scale bars correspond to 200 nm.

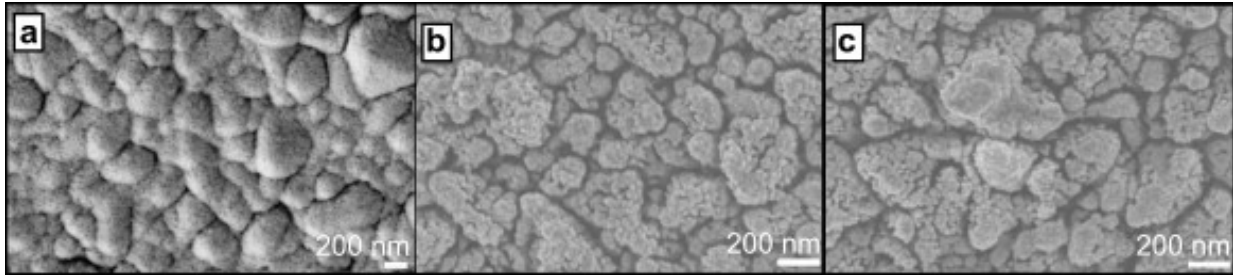


Figure 3-2: SEM images of nanoporous NiO films on FTO Glass using alternate anodization parameters (a) anodized using ethylene glycol in place of diethylene glycol as the electrolyte (b) anodization was begun with electrolyte at room temperature instead of chilled in ice bath (c) anodization conducted at constant voltage of 45 V. All scale bars correspond to 200 nm.

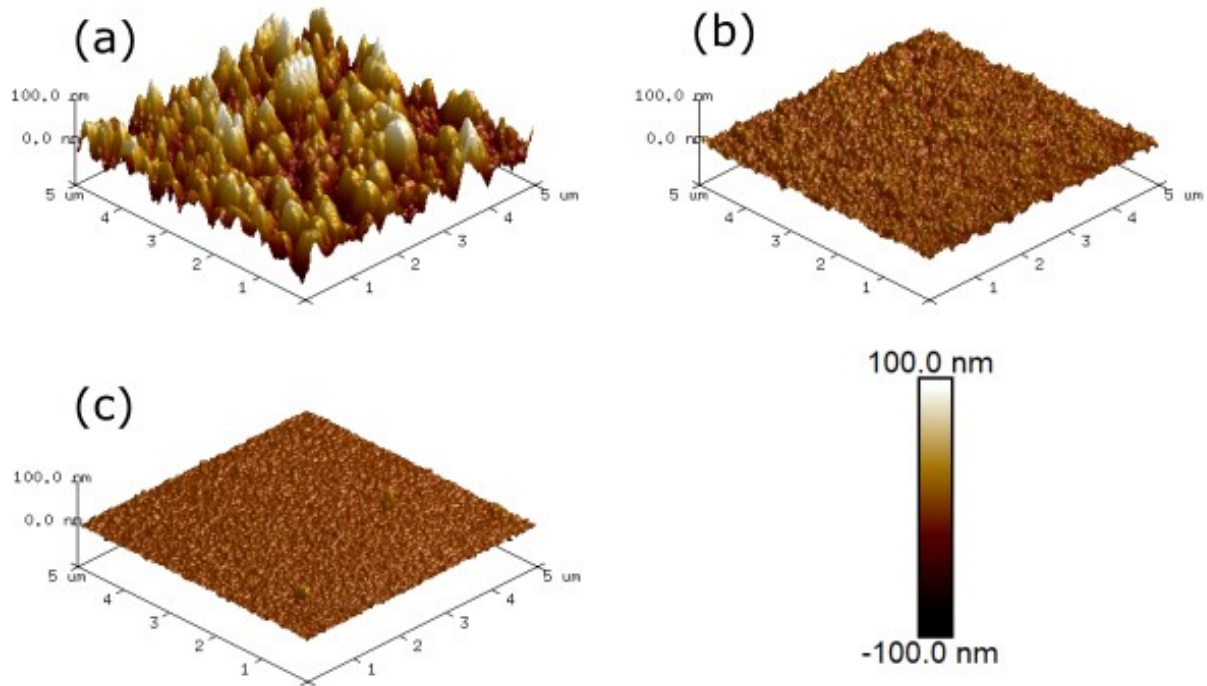


Figure 3-3: : Three-dimensional AFM Topographical Images of sputtered Ni On (a) FTO Glass, (b) ITO Glass, and (c) a silicon wafer. Shown in the bottom right corner of the figure is the scale for interpreting topographical heights by colour.

3.3.2 Anodized Film Characterization

A study of the phases present after anodization and the subsequent annealing step was conducted through use of XRD and XPS; XRD results are shown in Figure 3-4 while XPS results are shown in Figure 3-5 and Figure 3-6 for the Ni 2p and O 1s regions respectively. XPS was not conducted on Si samples, but as the annealing temperatures were identical for FTO and Si samples the spectra corresponding to FTO can be considered representative for Si as the approximately 10 nm surface depth characterized by XPS is not expected to be affected by the underlying substrate. On all substrates after anodizing but before annealing, no crystalline phases are present with the exception of trace amounts of Ni and the substrate. XPS spectra reveal the films are comprised of amorphous NiOOH and Ni(OH)₂ prior to the annealing step; this agrees with prior reports on anodization of Ni (46). However, after annealing the film at 600°C, XRD confirms the formation of crystalline NiO on both FTO and Si samples. On the other hand, NiO peaks on the ITO sample annealed at 375°C are very weak and the XRD signal is overwhelmed by stronger Ni peaks because the annealing temperature was not high enough. XPS results further substantiate this, as significant Ni(OH)₂ and NiOOH contribution to the spectra are apparent. This lower annealing temperature was selected in the case of ITO samples because ITO experiences thermal degradation as oxygen diffuses throughout its structure, lowering its conductivity (188). Thus, 375°C was the highest temperature that was attempted; clearly, there is incompatibility with a procedure that requires a post-annealing process and the use of ITO. On the other hand, XRD results of annealed NiO/Si samples show the presence of not only NiO but NiSi as well; from SEM images, this NiSi layer may be estimated as approximately 120 nm thick. Comparing the XRD patterns of Si samples before and after annealing, it can be ascertained that NiSi formed as Ni diffused into Si during the

annealing process, a well understood interaction that occurs between the two elements owing to the high diffusivity (189).

The formation of NiSi here is unavoidable as NiSi has a much lower formation temperature than NiO, with onset of formation at around 350°C. However, we also note that NiSi has been investigated for use in the microelectronics industry, such as a contact material for Si-based transistors owing to its low resistivity, and relatively low consumption of silicon during formation.(189-191) While we do not further investigate the NiO/NiSi/Si structure that forms, it may prove advantageous in device applications.

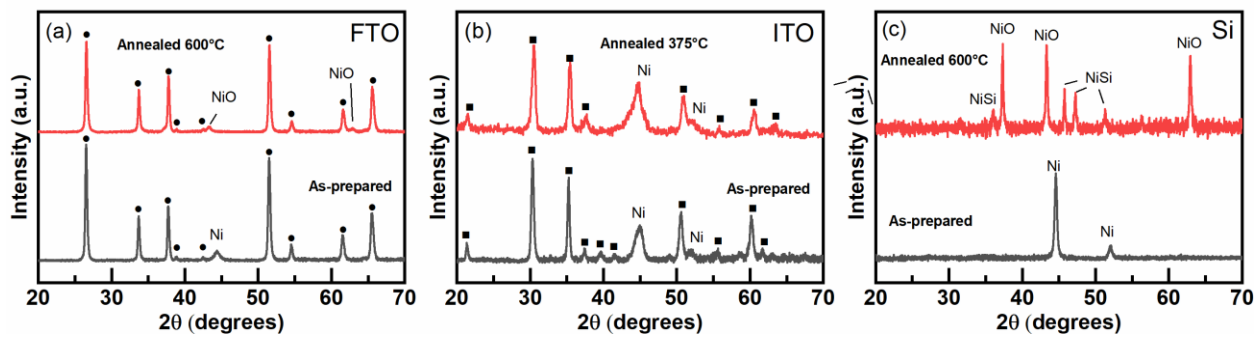


Figure 3-4: XRD patterns of anodized Ni films

On (a) FTO Glass, (b) ITO glass and (c) Si wafer substrates. The top red curve corresponds to annealed samples (600°C for FTO and Si, 375°C for ITO), while the bottom right curve corresponds to samples as-prepared after anodizing. The peaks labelled with a black circle ● corresponds to FTO while peaks labelled with a black square ■ corresponds to ITO, as determined by comparison to works by Yousif et al. and Irwin et al. respectively.(192, 193) The XRD peak corresponding to the Si substrate, located at $2\theta = 70^\circ$ is just out of frame.

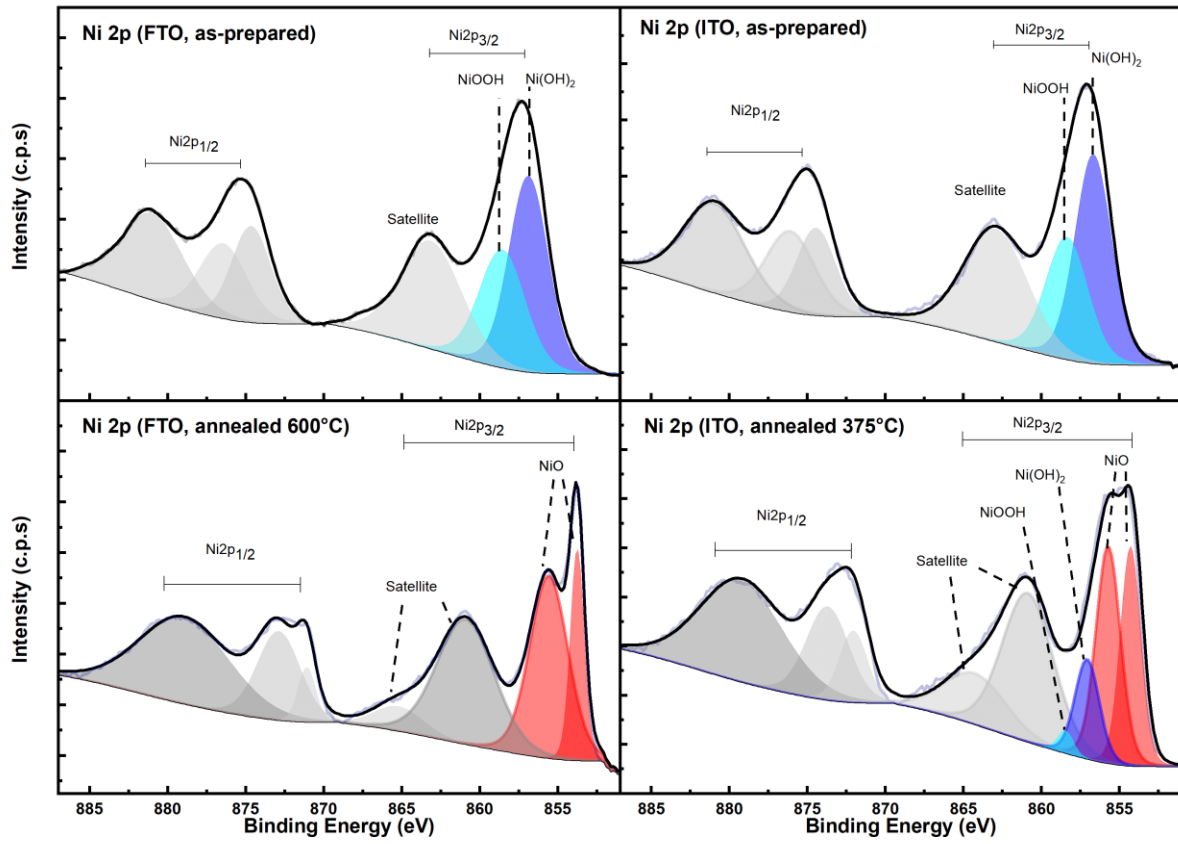


Figure 3-5: XPS spectra showing the Ni 2p region of anodized Ni films

(a) FTO samples as-prepared, (b) ITO samples as-prepared, (c) FTO samples annealed 600°C, (d) ITO samples annealed 375°C

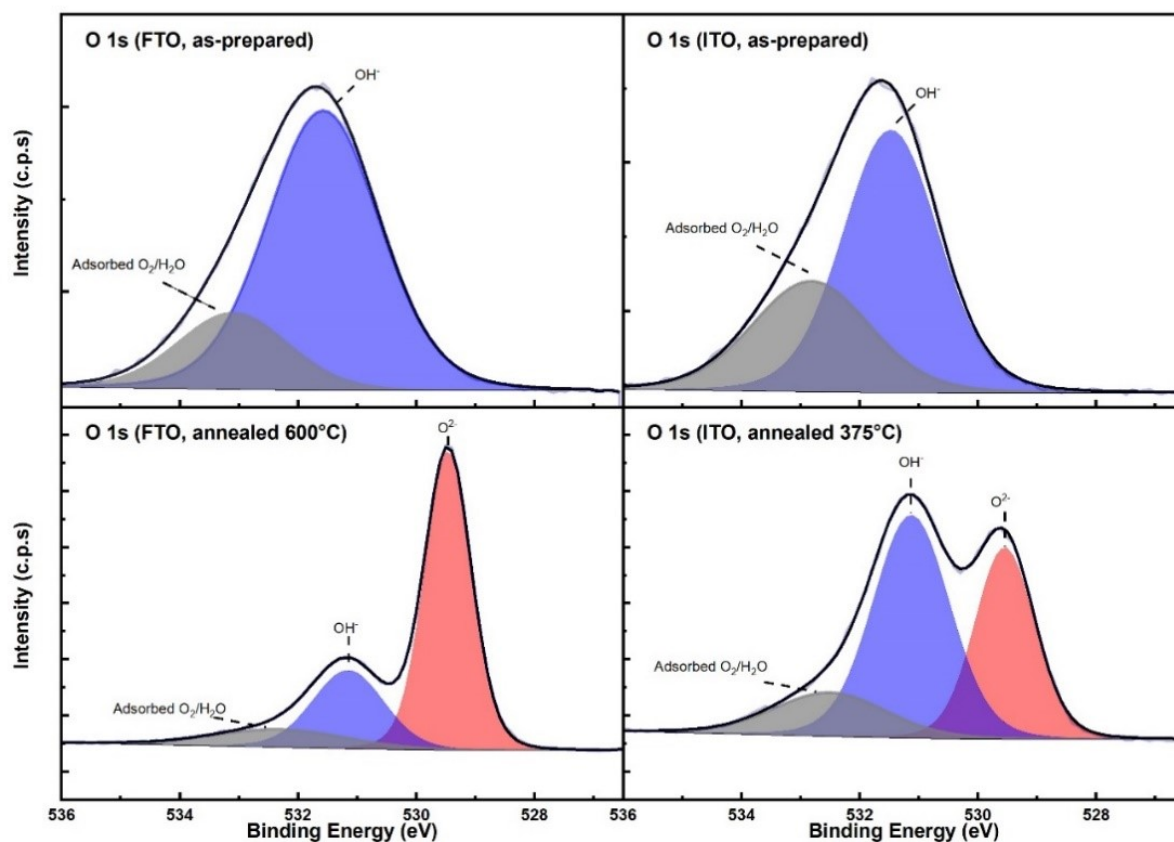


Figure 3-6: XPS spectra showing the O 1s region of anodized Ni films on (a) FTO samples as-prepared, (b) ITO samples as-prepared, (c) FTO samples annealed 600°C, (d) ITO samples annealed 375°C.

3.3.3 Optoelectronic Characterization of NiO on FTO-Coated Glass

The remainder of this work is devoted to optoelectronic investigation of the nanoporous NiO that was synthesized on FTO-coated glass through UV-Vis spectroscopy, electrochemical impedance spectroscopy (EIS) and Mott-Schottky analysis.

As shown in Figure 3-7, UV-Vis absorption spectra show the transparency of the NiO at visible wavelengths, which is expected given its large bandgap. In addition, a Tauc plot could be generated in order to determine the optical band gap of the material by plotting $(\alpha h\nu)^{\frac{1}{n}}$ vs $h\nu$,

where α is the absorption coefficient, h is Planck's constant, ν is the frequency of light, and n is a constant dependent on the electronic transition type (in most cases either direct or indirect transitions are considered, corresponding to an n of $\frac{1}{2}$ or 2 respectively). Here, NiO is assumed to have a direct band gap as has been generally done in previous literature (193-195). By extrapolating the linear region of Tauc plot to the point on the y-axis where $(\alpha h\nu)^{\frac{1}{n}} = 0$, the band gap can be determined to be 3.5 eV, which falls within the range of values typically reported for NiO (3.4–4.0 eV).

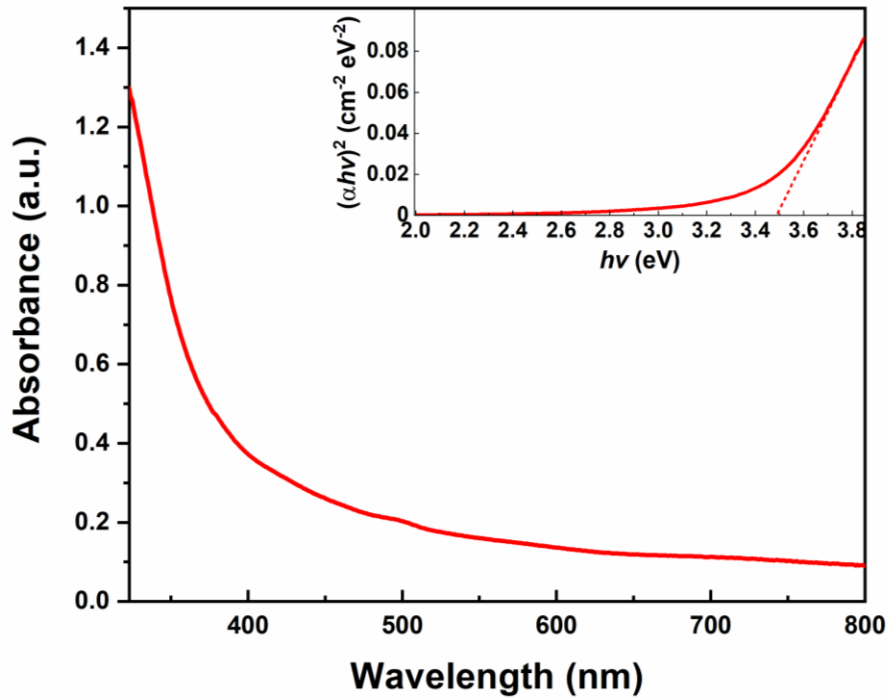


Figure 3-7: UV-Vis Spectra of NiO films on FTO-coated glass.

The inset shows the Tauc plot of the associated spectra, with the dashed line showing the measured band gap of the material at the x-intercept.

EIS was used to study the semiconductor interfacial behavior of the nanoporous NiO film in a phosphate buffer solution at pH 7, in room temperature and room lighting conditions. Experimental and fitted Nyquist and Bode Phase plots in the frequency range of 1 to 70000 Hz under dark

condition (i.e. without exposure to illumination), and at an applied potential of -0.4 V vs. Ag/AgCl are shown in Figure 3-8a and Figure 3-8b. The equivalent circuit of the EIS data is shown Figure 3-8c, where R_S , R_T , R_C , C_{SC} , and C_H are electrolyte resistance, charge transport resistance, charge transfer resistance, space charge capacitance, and electrochemical double-layer capacitance, respectively. Also present in the equivalent circuit diagram are two constant phase elements denoted by Q_1 and Q_2 with coefficients n_1 and n_2 . While impedances due to resistance R_S , R_C , and R_T are frequency independent and have the same magnitude as the resistances themselves, impedances due to capacitances ($Z_{C_{SC}}$ and Z_{C_H}) and constant phase elements (Z_{Q_1} and Z_{Q_2}) are frequency dependent, and are given by equations 3-1 to 3-4, where $i = \sqrt{-1}$. The total impedance of the system (Z) is given by equation 3-5.

$$Z_{C_{SC}} = \frac{1}{i(2\pi f)C_{SC}} \quad (3-1)$$

$$Z_{C_H} = \frac{1}{i(2\pi f)C_H} \quad (3-2)$$

$$Z_{Q_1} = \frac{1}{(i2\pi f)^{n_1}Q_1} \quad (3-3)$$

$$Z_{Q_2} = \frac{1}{(i2\pi f)^{n_2}Q_2} \quad (3-4)$$

$$Z = R_S + R_C + R_T + Z_{C_{SC}} + Z_{C_H} + Z_{Q_1} + Z_{Q_2} \quad (3-5)$$

The values of the equivalent circuit elements were obtained by fitting the transverse function, which was obtained by summing up the impedance of the elements. R_S , R_C , and R_T were determined to be 40, 15 and 78 $\Omega \text{ cm}^{-2}$, respectively. Similarly, C_{SC} , and C_H were determined to

be 4.2×10^{-8} and $6.0 \times 10^{-6} \text{ Fcm}^{-2}$, respectively. Q_1 and Q_2 are $9.3 \times 10^{-5} \text{ Fcm}^{-2}\text{s}^{-0.19}$ and $2.0 \times 10^{-4} \text{ Fcm}^{-2}\text{s}^{-0.08}$, respectively, and imply capacitive nature of the constant phase elements. Lastly, n_1 and n_2 were determined to be 0.92 and 0.81, respectively. R_C for this porous NiO film is found to be higher than other porous nickel oxide electrodes and therefore implies reasonable chemical stability (196). The product of R_T and C_{SC} is the hole-lifetime, τ , which is $3.28 \mu\text{s}$.

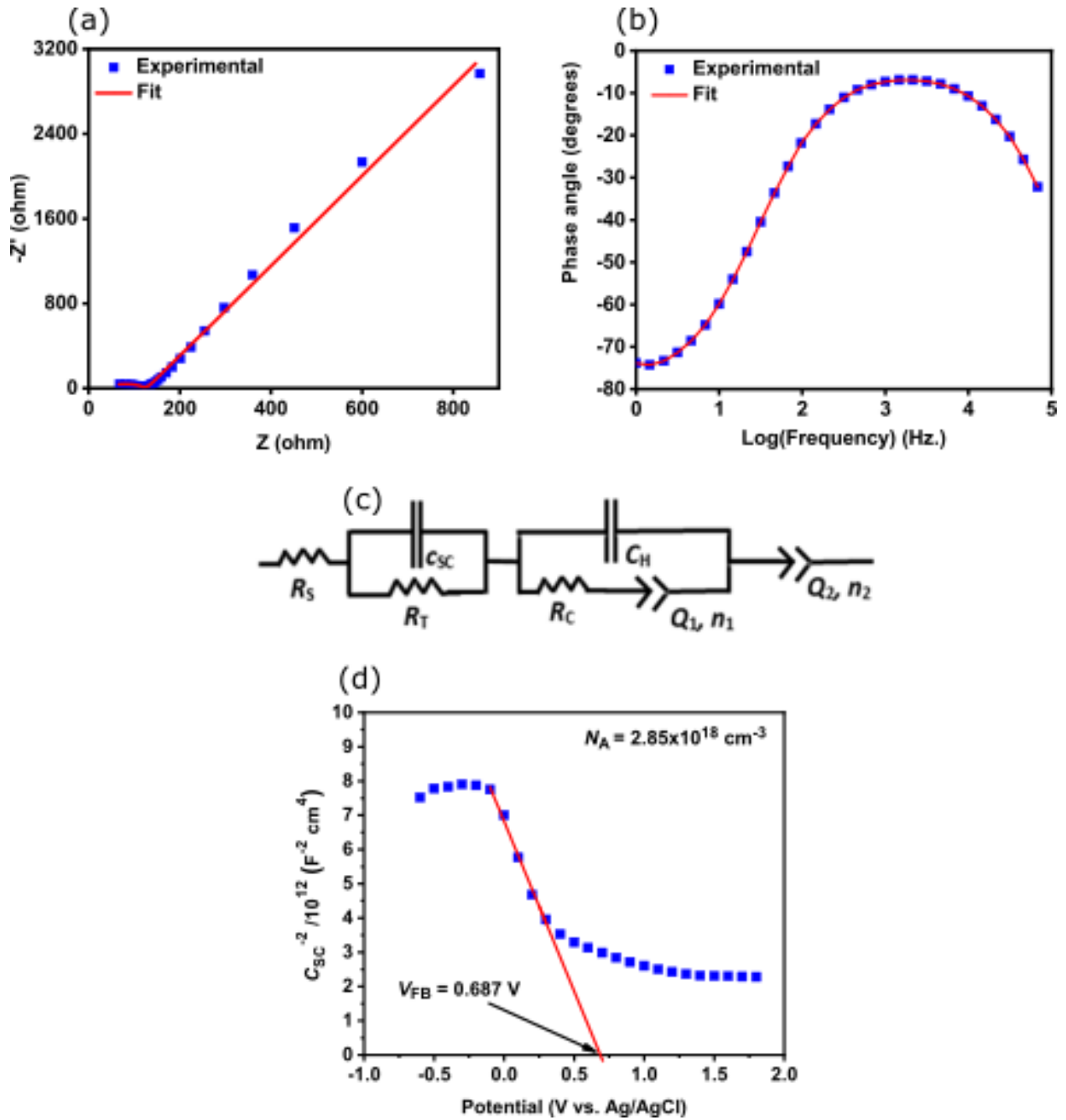


Figure 3-8: (a) Nyquist plot and (b) Bode phase plot of the NiO film on FTO. (c) is the equivalent circuit representing the Nyquist and Bode plots in (a) and (b). (d) Mott-Schottky plot of the NiO film showing the V_{FB} and straight-line fit that was used to calculate V_{FB} and N_A.

$$\frac{1}{C_{sc}^2} = \frac{2}{e\epsilon_0\epsilon_r N_A} \left(V - V_{FB} - \frac{kT}{e} \right) \quad (3-6)$$

$$N_A = \frac{-2}{e\epsilon_0\epsilon_r} \frac{dV}{dC_{SC}^2} \quad (3-7)$$

Mott–Schottky analysis was performed to estimate the charge carrier concentration (N_A) and flat band potential (V_{FB}) of the nanoporous NiO film on FTO-coated glass; the relevant equations for this analysis are shown in equations 3-6 and 3-7. In these equations, e is the elementary charge (1.602×10^{-19} C), ϵ_0 is the vacuum permittivity (8.854×10^{-12} F m⁻¹), ϵ_r is the semiconductor dielectric constant, taken as 5 for NiO(197), V is the applied potential, k is the Boltzmann constant (1.381×10^{-23} J K⁻¹), and T is the temperature in K. N_A was calculated using eqn. (7) and the slope of the Mott-Schottky's plot (Figure 3-8d). The slope is noted to be negative, which confirms the expected p-type behaviour. N_A is found to be 2.85×10^{18} cm⁻³, a value that is similar to acceptor densities values reported in literature (198, 199). V_{FB} was determined from the intersection of the slope of the Mott-Schottky plot with the horizontal axis denoting potential and is found to be 0.687 V vs. Ag/AgCl.

3.4 Chapter Conclusion

Here again are the research sub-questions asked in this chapter, which contribute to the major research question, “What are the effects of conducting novel anodization techniques on sputtered non-native substrates?”:

1. Can nanoporous NiO be formed on non-native substrates?
2. How does substrate surface texture and material of choice impact resultant morphology?
3. What are the properties of nanoporous NiO on non-native substrates?

We have presented, for the first time, anodized nanoporous NiO on non-native substrates. The formed NiO layers were approximately 200 nm thick. Based on SEM observations, we have found that the morphology of the as-anodized $\text{NiO}_x(\text{OH})_y$ tends to be highly dependent on the surface roughness of the underlying substrate, which may be attributed increased vulnerability to chemical etching processes. That anodization of Ni tends to result in hydroxides rather than an oxide directly can also be attributed to the overall difficulty experienced by researchers in achieving nanotubular NiO. Furthermore, based on the phases identified using XRD and SEM observations, an approximately 120 nm thick layer of NiSi is present underneath anodized NiO on Si wafers, which may be attributed to the high diffusivity between Ni and Si. By investigating the samples by XPS in the as-anodized and after annealing state, the presence of $\text{NiO}_x(\text{OH})_y$ after anodizing is confirmed and NiO after annealing. The relative fragility of $\text{NiO}_x(\text{OH})_y$ compared to other anodized materials such as TiO_2 or Al_2O_3 explains the importance of surface roughness to the resultant morphology, as grain boundaries serve as preferential etching sites. This also means that precise control of voltage and temperature are particularly important when anodizing thin films of Ni, as there is no bulk amount of Ni below the anodized layer and over-etching is a risk. We found that using constant current when anodizing at ice bath temperatures helped prevent over-etching from occurring and resulted in a more ordered morphology with distinct nanopores. A DEG-based electrolyte was found to result in pores an order of magnitude larger than EG-based electrolytes on NiO on FTO-coated glass (2-3 nm pore diameter in EG, pushing the resolution limit of the SEM and the ability to make a more quantitative observation, compared to 13.4 ± 2.8 nm using DEG). We also found that anodized NiO demonstrated an appropriate band gap and charge carrier densities of 3.5 eV and $2.85 \times 10^{18} \text{ cm}^{-3}$ respectively, and demonstrated p-type semiconducting behaviour, indicating that the quality of the nanoporous layer is excellent.

Chapter 4: Ta₂O₅ Nanodimples formed on non-native substrates

4.1 Chapter Introduction

Tantalum pentoxide has been studied extensively over the past decades. In particular, thin films of tantalum oxide have been investigated for a diverse host of applications—initially as an antireflective coating on the 1970's for optoelectronic applications, their largest use is in tantalum-based capacitors (200). Ta₂O₅'s success in the microelectronics industry is largely attributed to its performance as a dielectric material. Ta₂O₅ is considered a high dielectric constant (high- κ) material, meaning that its dielectric constant is greater than SiO₂. Ta₂O₅'s typical classification as an insulator is blurred when one considers its bandgap—depending on its method of manufacture, it has been reported as somewhere as low as 3.8 eV and as high as 5.3 eV, meaning that it can also exist as a wide-bandgap semiconductor. With respect to the microelectronics industry, chemical vapour deposition (CVD) is the standard method used for Ta₂O₅'s integration into silicon-based technology, owing to CVD's advantages in conformality and relatively high rates of deposition (200). Other techniques for manufacture include oxidation techniques such as anodic and thermal oxidation, physical and chemical vapour deposition techniques, and sol-gel techniques (201-205).

Anodization of metals such as Al, Ti, Ta, Ni, Fe, etc. has proven to be an effective method to produce ordered nanostructured surfaces (84, 153, 168, 206, 207). Furthermore, this solution-processable method is proven to be suitable for industrial-scale production. The films that are produced by anodization have numerous uses, from superior wear and corrosion resistance, to serving as a base layer for the production of fouling resistant, to taking advantage of the fact they are dielectrics and semiconductors in optical and electronic applications (3, 208-210). Tantalum nanodimples can be obtained by electrochemical means, including electropolishing and

delamination of grown nanotubes in an anodization process (211-214). These pores have been observed in several studies, but to date they have barely been investigated. To the best of our knowledge, the only studies that are dedicated to this topic were conducted by the Kruse group and Birss group, who investigated Ta dimple formation on Ta foils and their use as nanostructured electrodes (212-216).

The conversion of the Ta to its analogous oxide or nitride opens up a huge array of possibilities to take advantage of, such as serving as a base for UV-transparent superhydrophobic coatings, as a platform for high-energy photo sensors, etc. Herein, we describe the production of Ta₂O₅ nanodimples on technology-relevant non-native substrates using a simple annealing procedure. The morphological changes during this process are minor, and the ordering of the dimples is maintained. We also demonstrate that oxide conversion of the dimples is also possible via a secondary anodization process. We conduct a comparison of structural dimensions across differing anodization voltages and quantify the morphological changes that are expected after the annealing procedure, using electron and helium ion microscopy, and atomic force microscopy (AFM). X-ray diffraction (XRD) provides further support of the effects of the annealing process. We then turn to potential uses of the Ta₂O₅ nanodimples as platforms for plasmonic photocatalysis by decorating the surface of the produced nanodimples with Au nanoparticles. We utilize ultraviolet-visible (UV-VIS) spectroscopy to demonstrate the absorption characteristics of these samples before and after Au nanoparticle decoration to show the clear effects that localized surface plasmon resonance (LSPR) causes in the absorption profile and, in tandem with electron energy loss spectroscopy (EELS), quantify the optical band gap of the bare Ta₂O₅. Lumerical simulations are utilized to demonstrate the optical effects of the dimple morphology. Finally, we demonstrate that Ta₂O₅ nanodimples are able to increase the photoconversion of para-aminothiophenol (PATP)

to p,p'-dimercaptoazobenzene (DMAB) when used in tandem with Au nanoparticle photocatalysts by surface-enhanced Raman spectroscopy (SERS).

4.2 Experimental Details

4.2.1 Sample Preparation

A schematic of the process flow is shown in Figure 4-1. The first step in the process was sputtering. The substrates were fused quartz slides purchased from Advalue Technologies. Before sputtering, the substrates were immersed for in a piranha solution comprised of a 3:1 mixture of sulfuric acid and hydrogen peroxide for 15 minutes, then rinsed with deionized (DI) water and dried under flowing nitrogen. Ta was deposited on substrates by DC magnetron sputtering using a Ta target of 99.95% purity (Kurt J. Lesker). All sputtering was conducted in an argon-filled chamber at 2.5 mTorr using a power of 200 W, with a target-to-substrate distance of 15 cm. The substrate was heated to 500° C during deposition, and the deposition rate was approximately 1.28 Å/s.

The electrolyte used for anodization consisted of 0.24 M NH₄F in 5 vol.% DI water, 5 vol.% diethylene glycol (DEG), 90 vol.% sulfuric acid (H₂SO₄, 95-98%). This electrolyte was prepared by first dissolving NH₄F in H₂O, then mixing in the DEG. The H₂SO₄ was then slowly added in, stirred, and the as-formed solution allowed to cool to room temperature (the addition of H₂SO₄ being exothermic). The cathode used was a 3.05 mm diameter carbon rod. The anode was spaced 1 cm away from the base of this cylindrical carbon rod. No reference electrode was used, and anodization was conducted without stirring. Anodization was conducted using potentiostatic conditions for the desired length of time. After anodization, the sample was removed from the electrolyte and submerged in DI water to remove the formed nanotubes and clean the residual

electrolyte from the sample. After drying under nitrogen, samples were placed in a tube furnace for annealing. Annealing was conducted at 650°C for 3 hours, with a 3 hour ramp up time; the furnace was turned off at the end of this process and allowed to cool back to ambient before the sample was removed from the furnace.

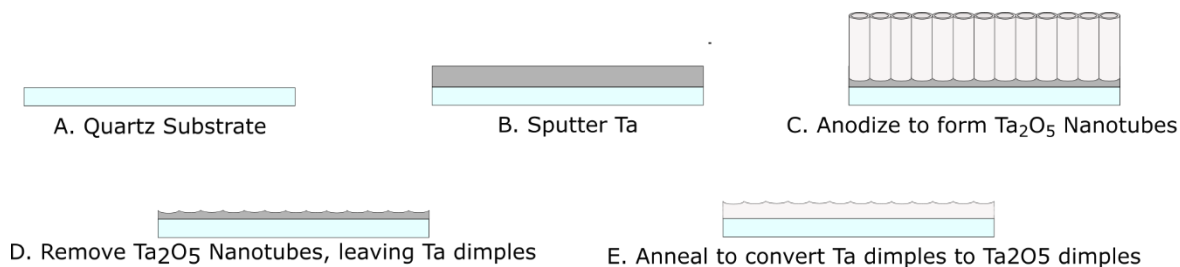


Figure 4-1: Schematic Illustration of the Growth of Ta₂O₅ nanodimples on a quartz substrate

4.2.2 Characterization

Imaging was conducted using either a Zeiss Sigma Field Emission Scanning Electron Microscope (FESEM) and a Zeiss Orion Helium Ion Microscope (HIM). The pore diameters were measured from acquired micrographs using ImageJ software. The diameter of each pore was measured as the farthest distance a horizontal line could pass from left side to the right side of a pore. For pore selection, a single pore was initially selected arbitrarily near the center of an FESEM micrograph, with subsequent pores being chosen in an outward spiral from the starting pore. In all cases, 100 pores were measured. Two-dimensional fast Fourier transforms (2D-FFT) of the FESEM images was obtained using WSxM software (217).

AFM was conducted using a Bruker Dimension Edge atomic force microscope. The instrument was operated in tapping mode and used a tip of <10 nm atomic radius to form a topographical map 3 μm x 3 μm. Using Bruker Nanoscope Analysis software, dimple depth was measured by considering the vertical depth of a pore from the sidewall to the lowest point in the middle of a pore; pore selection was done in an identical fashion to pore diameter, and 100 pores

were measured. XRD patterns were collected using a Rigaku Ultima IV equipped with a Cu-K α source. High resolution transmission electron microscope (HRTEM) images were collected with a Hitachi H9500 TEM, with an accelerating voltage of 300 kV. The EELS spectra were recorded under TEM imaging mode, recorded on a Gatan GIF Tridium spectrometer. UV-Vis Spectroscopy was conducted using a PerkinElmer Lambda 1050 Spectrophotometer operating in transmission mode.

Finite difference time domain electromagnetic simulations were used to model the optical properties of the Ta₂O₅ dimples using Lumerical FDTD simulation software. The optical absorption and scattering of nanodimples with a pore diameter of 30 nm and a pore depth of 5 nm, corresponding to an anodization voltage of 30 V, were simulated. Three sets of simulations were performed, each exploring the effect of the high index Ta₂O₅ dimpled dielectric substrate on gold nanoparticles (NPs): (i) Au NPs partially embedded in a planar film of Ta₂O₅ (ii) Au NPs partially embedded in a Ta₂O₅ dimple, and (iii) An array of Au NPs partially embedded in an array of Ta₂O₅ nanodimples. The Au NPs were of radius 10 nm and the simulations were performed in a vacuum environment. Index monitors were utilized to provide refractive index mapping of the simulated structures and helped confirm that the dimples and nanoparticles were appropriately configured and identified by the software throughout the course of the simulation. Near-field, and far-field profiles and frequency monitors captured reflection and transmission as well scattering and absorption spectra of the dimple-nanoparticle systems. Refractive index data corresponding to Ta₂O₅ were obtained from Marcos et al. (218). In Lumerical, the dimples were illuminated by a plane-wave light source incident at normal angle from above with a bandwidth between 250–800 nm. The symmetry of the Ta₂O₅ dimples were considered by setting appropriate symmetric and anti-symmetric boundaries allowing for shorter simulation times, and accurate data aggregation.

For plasmonic photocatalytic testing, Au nanoparticles were deposited on Ta₂O₅ nanodimples. For these experiments, nanodimples were prepared using the above procedure with an anodizing voltage of 20 V and the thermal annealing process. Au nanoparticle decoration was done by sputter-deposition upon the surface of the as-synthesized samples using a DC magnetron sputter system (Kurt. J. Lesker CMS-18). Deposition parameters were as follows: the base pressure was around 10⁻⁶ Torr, argon was used as the deposition gas, the deposition pressure was 7 mTorr, and the deposition power was 75 W. Sputtering was conducted for 20 seconds at a rate of approximately 7.6 nm per minute using a 3 inch diameter 99.9% purity sputtering target. No heating was used during gold deposition. Following sputtering, the gold-decorated samples were annealed in a tube furnace in air at 650 °C for 30 minutes. A one-hour ramping duration was employed; following annealing, the samples remained in the tube furnace as it cooled to room temperature before being removed. Gold nanoparticle dimensions were obtained by the selecting nanoparticles from a FESEM micrograph by the same procedure as described for pore diameter. The samples were prepared for photocatalytic studies by drop-coating 1 mL of a solution of 50 μM of PATP in methanol on the Au nanoparticle-decorated Ta₂O₅ substrates. The photocatalytic reaction was powered by the laser of a Nicolet Omega XR Raman Microscope using a 633 nm wavelength and a laser illumination power of 0.1–2 mW, which simultaneously collected Raman spectra and allowed for immediate feedback of reaction products. The reaction time (which was also the Raman spectra acquiring time) was 60 s.

4.3 Results and Discussion

4.3.1 Ta₂O₅ Dimple Formation

Anodization was conducted using a voltage of 7-40 V, after which Ta₂O₅ nanotubes were observed; some images of delaminated nanotubes is shown in Figure 4-2. Extending the voltage beyond this range (experiments conducted at an anodizing voltage of 45 V, 50 V, 60 V and 80 V) results in a disordered porous oxide, in agreement with the findings of Singh et al. (216); SEM images of these disordered porous oxides is shown in Figure 4-3. The current density was recorded as a function of time during the anodization process and a representative example is shown in Figure 4-4. The curve is typical of a nanotube anodization process according to the following steps: (i) an initial rapid decrease in current is observed as oxide forms on the surface, which acts as a barrier to the flow of electrons and ions, (ii) an increase in current as the oxide thins locally owing to pore formation an, (iii) a steady decrease in current as the nanotubes grow longer, meaning ions must diffuse further to take part in the anodization reaction. Abnormally, two small increases in current are observed between 20–35s; they can possibly be attributed to a shift from a disordered pore formation to a self-organized one that occurs during initial steps (72), or an increase in temperature leading to a faster reaction rate that occurs during the exothermic anodization process.

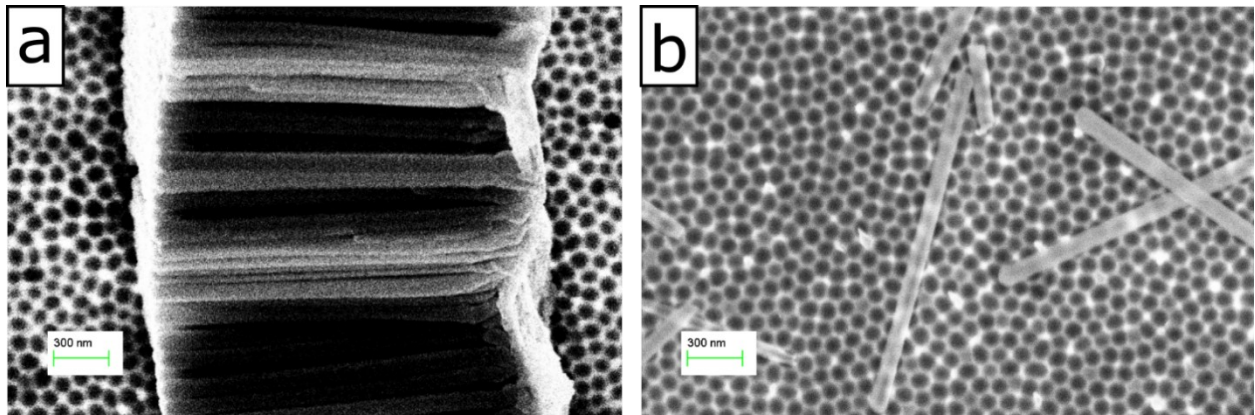


Figure 4-2: SEM Images of delaminated Ta₂O₅ nanotubes laying on top of Ta Dimples

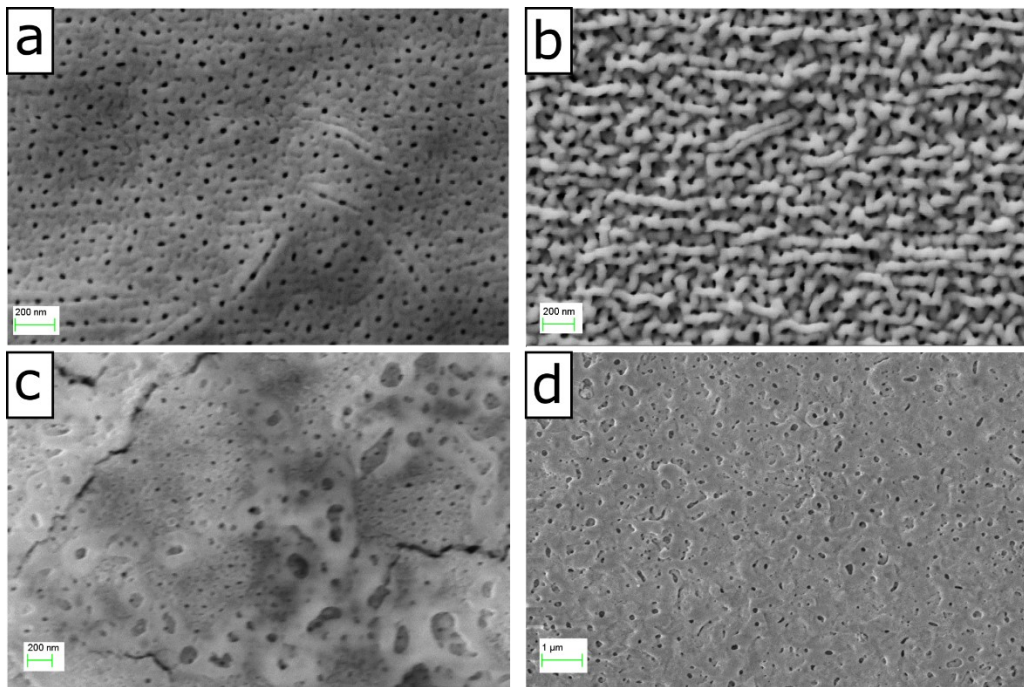


Figure 4-3: SEM images of disordered porous oxides
Formed by anodization voltages of (a) 45 V, (b) 50 V, (c) 60 V, (d) 80 V

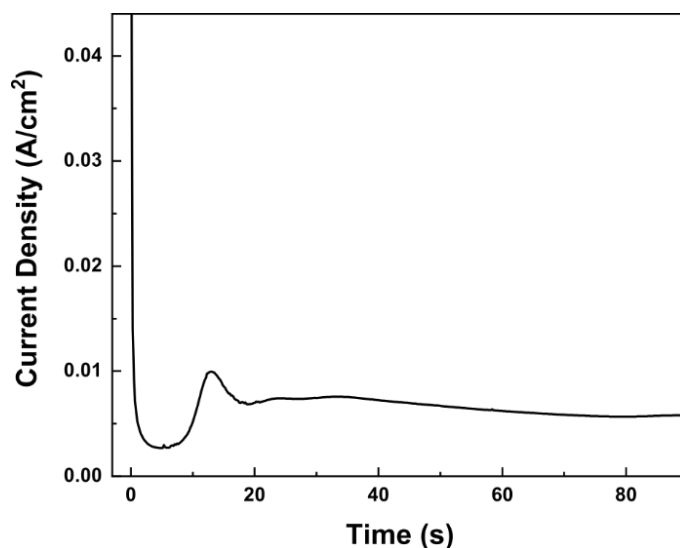


Figure 4-4: Typical current density-time plot of Ta_2O_5 nanotube anodization. This plot in particular was produced using a constant anodization voltage of 30 V.

As anodization proceeds, Ta is consumed and the thickness of the Ta film decreases linearly, with higher voltages causing faster anodization; as shown in Figure 4-5a, Ta is consumed at a rate of approximately 1.0 nm/s and 2.0 nm/s for 15 V and 40 V respectively. As the Ta is consumed, the length of the Ta_2O_5 nanotubes (which may also be referred to as the thickness of the nanotube layer) increases correspondingly, at a rate of 3.8 nm/s for 15 V as is shown in Figure 4-5b. The length of the grown nanotubes far outstrips the amount of Ta consumed. This is partly explained by the volumetric expansion that occurs when a metal is converted to its metal-oxide analogue. Conventionally, the Pillings-Bedworth ratio (PBR) relates the volume expansion of an oxide to its analogous metal. Considering a 2D layer of material, one can assume all volumetric expansion occurs in the direction perpendicular to the substrate plane, meaning that the increase in layer thickness between Ta and Ta_2O_5 can be directly related to the Pillings-Bedworth Ratio. When oxide formation occurs at a metal/oxide interface, a volume change occurs due to the formation of the oxide (219). This volume change depends on the metal, and is calculated as:

$$PBR_{Metal} = \frac{V_{m,oxide}}{V_{m,metal}} = \frac{M_{oxide} \cdot \rho_{Metal}}{n_{atoms} \cdot M_{metal} \cdot \rho_{Oxide}} \quad (4-1)$$

where $V_{m,oxide}$ and $V_{m,metal}$ is the molar volume of the oxide and metal respectively, M_{oxide} and M_{metal} is the atomic mass of the oxide and metal respectively, and n_{atoms} is the number of atoms of metal per molecule of the oxide. Thus, the calculated ratio for Ta₂O₅ is 2.47. We observe an average expansion ratio in layer thickness of 3.95 for Ta₂O₅ nanotubes, far higher than the PBR predicts. This is explained by the porosity of the nanotube layer and the plastic flow model of nanostructural growth by anodization (220). We note that our nanotubes appear to be more dense than that obtained by Horwood et al., who noted an expansion ratio of 4.4; while it is difficult to make a further comparison as their anodization occurred on an annealed Ta foil, this may occur because of the relatively Ta high densities obtained when sputtering Ta at elevated temperatures, as in this work.

After removal of formed nanotubes, well-defined pores were found across the substrate. As-formed, these pores are comprised of Ta (as verified by XRD and EELS later); however, it should be noted that based on etch-depth x-ray electron spectroscopy investigations by El-Sayed et al., a thin layer of amorphous Ta₂O₅ approximately 4 nm thick—which is within the range that would be expected for the native oxide—is likely present at the surface (215). After the annealing process, the Ta has been converted into Ta₂O₅, as shown by XRD and EELS later. We conducted FESEM imaging characteristic samples across a range of synthesis voltages both before and after the annealing step, which is shown in Figure 4-6. The dimples enlarge as synthesis voltage increases, and during annealing the Ta is observed to expand during oxide formation. This means that the very small dimples observed when obtained using an anodization voltage of 7 V disappear

completely upon annealing. The ordering of the nanodimples is observed to be largely maintained after annealing as evidenced by 2D-FFT results shown in the insets of Figure 4-6; a sharp ring showing the presence of short term order and slightly disturbed long-term periodicity (75). The samples made at 7 V show only a diffuse ring, indicating disorder across the sample surface. We also note that upon annealing, the entire layer thickness increases substantially owing to oxide expansion, as is shown in Figure 4-5c. Here, we note an expansion ratio of 2.43, which is well in line with the calculated Pillings-Bedworth ratio of 2.47.

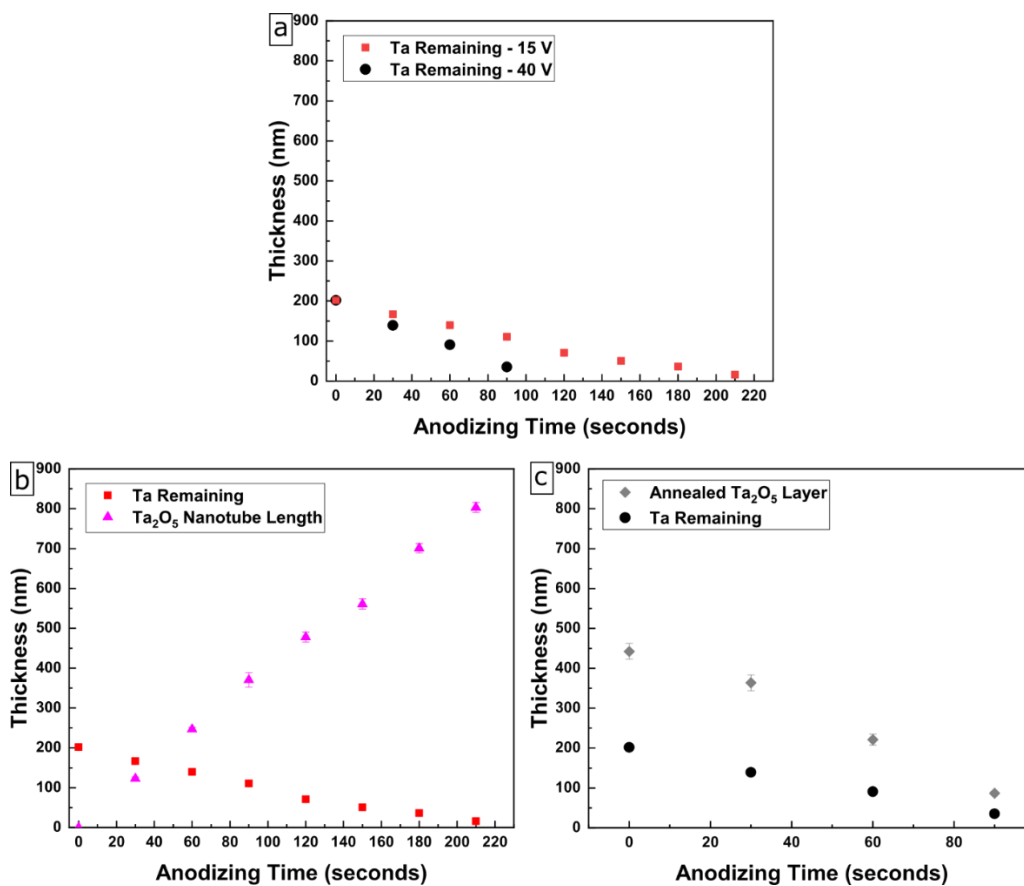


Figure 4-5: Ta film thicknesses as a function of anodizing time.

(a) shows the consumption of 200 nm Ta films under anodization at both 15 V and 40 V synthesis voltages. (b) shows a growth of nanotube length and corresponding tantalum consumed at 15 V (c) shows the conversion of a nanodimpled Ta film into a Ta₂O₅ film after annealing at 40 V. Note that (b) in part displays identical data as the “Ta Remaining – 15 V” data points from (a), and (c) in part displays identical data as the “Ta Remaining – 40 V” data points from (a).

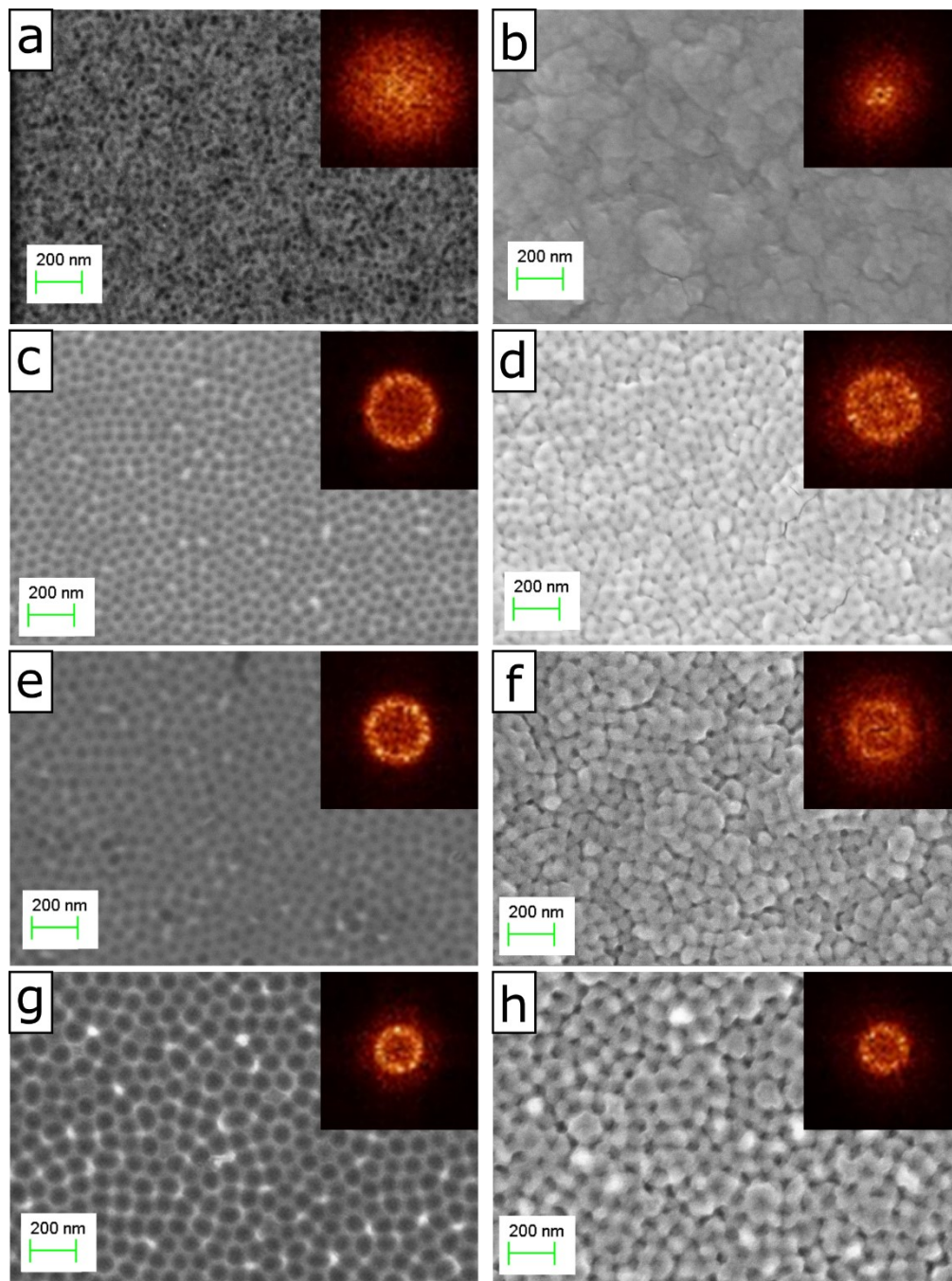


Figure 4-6: SEM Images of Ta nanodimples. Insets shows 2D-FFT
 Images (a), (c), (e), and (g) are Ta dimples (left side column), while (b), (d), (f), and (h) are Ta_2O_5 dimples (right side column). Anodization voltages correspond as follows: (a-b) 7 V, (c-d) 15V, (e-f) 25 V, and (g-h) 40 V.

The requirement of elevated annealing temperatures presents problems where film-substrate interactions at high temperature are possible and undesired; for example, if silicon is the underlying substrate, at elevated annealing temperatures silicon could be incorporated into the oxide film (221). We conducted some brief exploration into using a second anodic oxidation to convert Ta nanodimples into Ta₂O₅, which we concluded was feasible. We concluded that it is possible to obtain Ta₂O₅ dimples by a second anodization conducted after the first anodization, after the obtained nanotubes have been removed. This converts Ta to Ta₂O₅ without producing pores itself and is usually referred to as a compact layer anodization. When anodizing to obtain a compact layer, it should be recognized that there is a practical maximum thickness that can be obtained, related to the breakdown voltage of the oxide film. Oxide growth proceeds by field aided ion transport, as O²⁻ ions react with oxidized metal ion species. As the oxide layer grows thicker and thicker, the electric field at the metal/oxide interface grows weaker and weaker, according to Equation 1-6. Assuming potentiostatic conditions, then this process is self-limiting and film formation will reach some maximum; under galvanostatic conditions, the voltage will increase as thickness grows until the breakdown voltage is reached.

In order to completely convert the approximately 100 nm of Ta into Ta₂O₅, anodic oxidation was conducted using potentiostatic conditions at 100 V in a 0.5 M aqueous H₂SO₄ electrolyte using a graphite cathode with an electrode spacing of 1 cm; the dimpled Ta area was the area of anodization. The observed current-density–time plot obtained during anodization and the resultant Ta₂O₅ dimples is shown in Figure 4-7a and Figure 4-7b respectively. The current density decreased to a minimum value due to the formation of a highly resistive oxide layer without the formation of further pitting; this is expected in a compact layer anodization. There are several noticeable abnormalities in the spectrum with sudden spikes in current which might be

related to gas bubble formation and release. Also, it was noted macroscopically that around 25% of the produced film consisted of a featureless oxide that might be indicative of local electropolishing. Nevertheless, across much of the film the nanodimpled surface was intact, with an oxide expansion similar to that observed in Figure 4-6. This double-anodization process stands to be optimized, but for the purposes of this work, we simply note that it is a viable method to obtain Ta₂O₅ nanodimples.

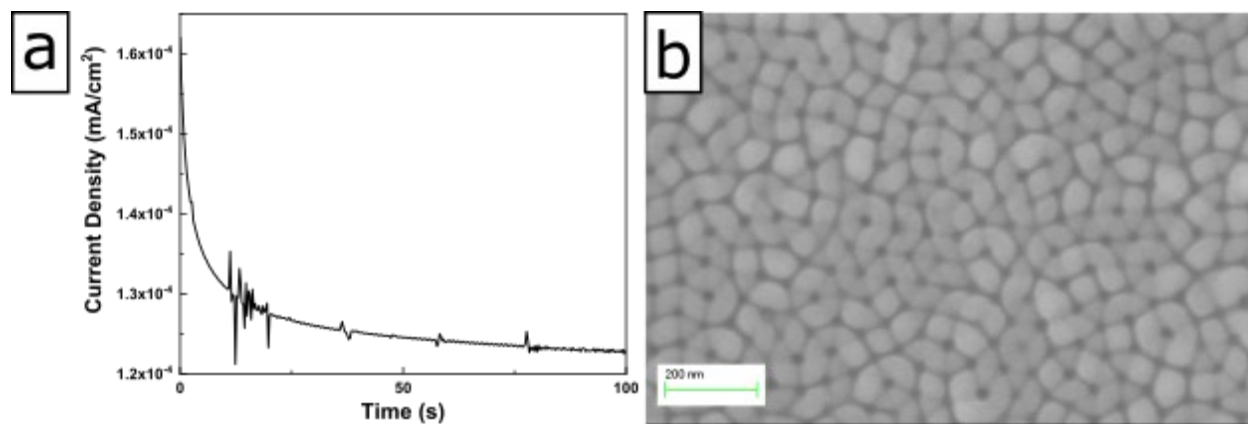


Figure 4-7: (a) Compact layer anodization to convert Ta dimples to Ta₂O₅ (b) Ta₂O₅ as obtained by double anodization.

By analysis of FESEM Images and AFM (characteristic AFM results shown in Figure 4-8), we demonstrate control of both the pore diameter and depth of the dimples by controlling the anodizing voltage. Both diameter and depth are shown to be an approximately linear function of the anodizing voltage, as shown in Figure 4-9. After annealing to form Ta₂O₅, pore diameter and depth decrease as a result of the oxide expansion. It should be noted however, that it is possible that the measured pore depth which can be affected by the tip geometry owing to the relatively small lateral dimensions of the pores; fresh tips were frequently used when acquiring

measurements and tips were of radius $<10\text{nm}$, but nevertheless we cannot entirely preclude a deeper pore depth than is measured.

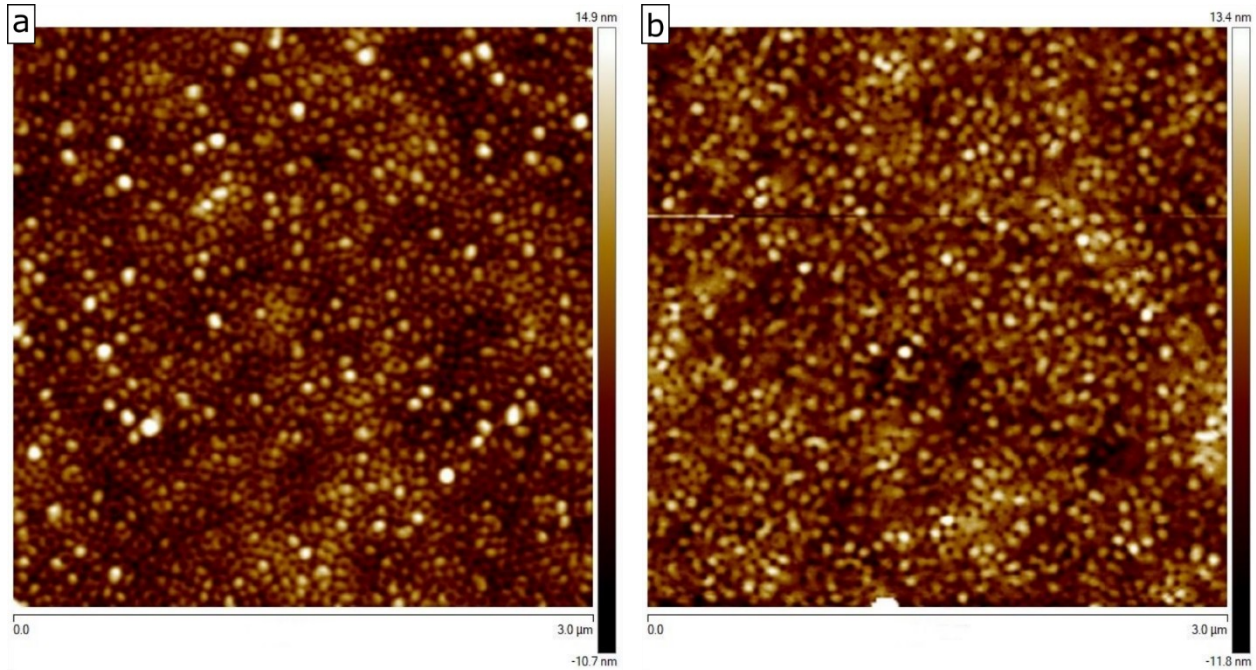


Figure 4-8: Characteristic 2D AFM Images of (a) Ta nanodimples and (b) Ta₂O₅ nanodimples. Both sets of images were collected from samples made using a 20 V anodization voltage

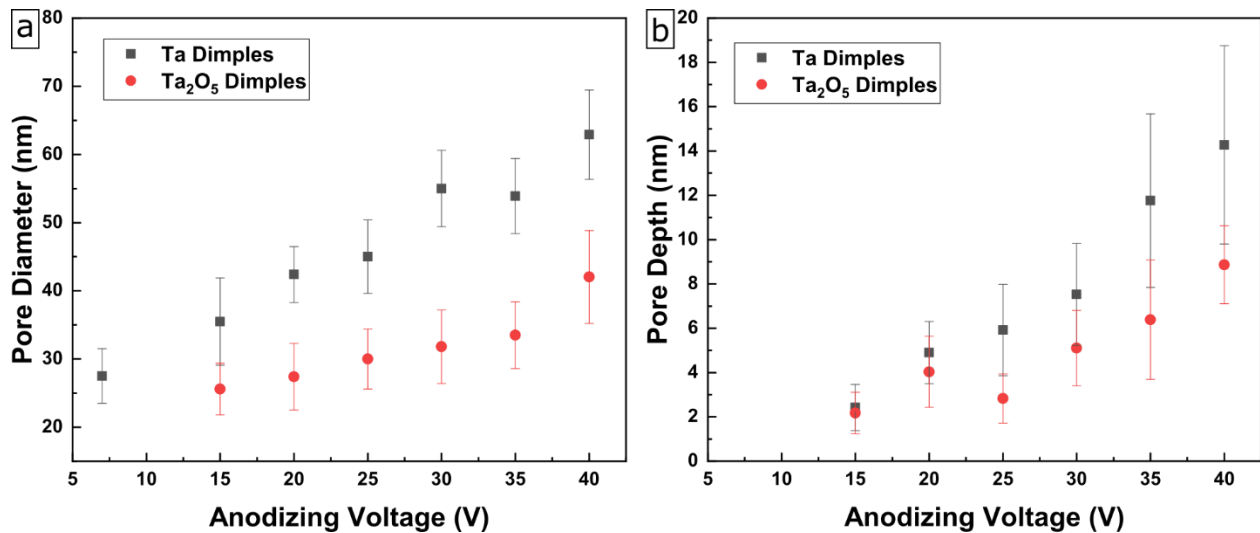


Figure 4-9: (a) shows the pore diameter while (b) shows the pore depth of nanodimples as a function of anodization voltage, before and after annealing.

4.3.2 Characterization of Ta₂O₅ Dimples

XRD patterns of Ta and Ta₂O₅ nanodimples are shown in Figure 4-10a and Figure 4-10b. The peaks in the XRD patterns were identified using Powder Diffraction Files 00-046-1045, 00-004-0788, 04-011-3914, and 01-089-284 for quartz, α -Ta, β -Ta, and β -Ta₂O₅ respectively (222). XRD confirms the presence of crystalline Ta prior to annealing; this pattern is representative of Ta films obtained after sputtering but before any further processing. After annealing, we note the formation of crystalline Ta₂O₅ but see no evidence of Ta. We also note that the broad peak attributed to the quartz substrate in Figure 4-10a appears to still be visible in Figure 4-10b, although a much stronger peak attributed to (001) Ta₂O₅ mostly overlaps it.

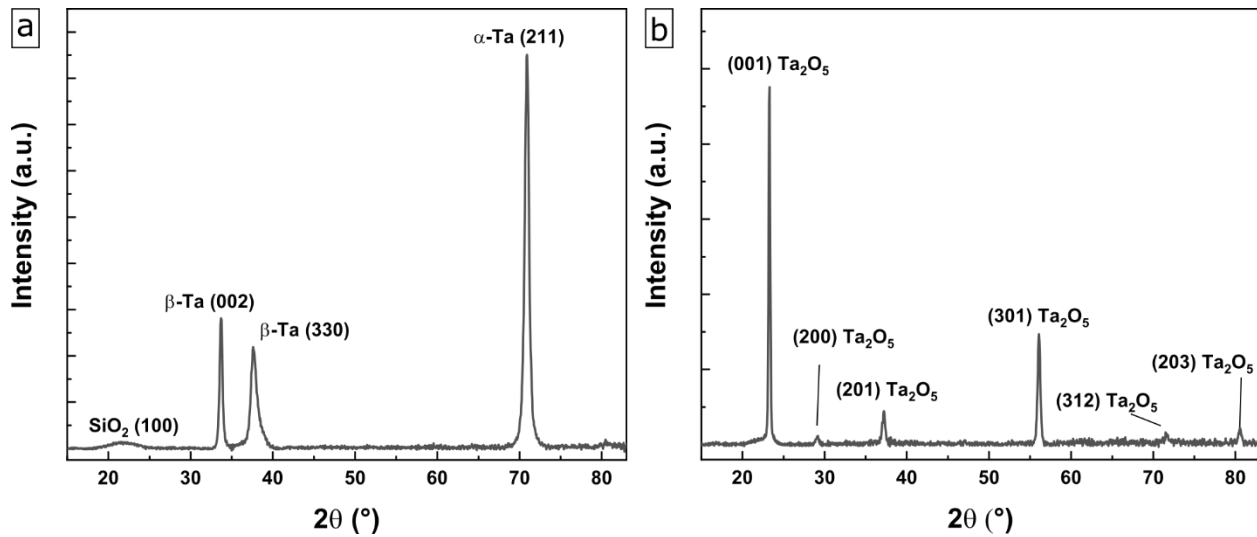


Figure 4-10: XRD patterns of (a) Ta nanodimples and (b) Ta₂O₅ nanodimples. The pattern in (a) is also representative of the sputtered Ta film before further processing.

HRTEM was conducted on the Ta₂O₅ nanodimple sample, and is shown in Figure 4-11a. As is visible from inspection of the image (selected area diffraction pattern not shown), the material under inspection is amorphous, which suggests that despite strong peaks indicative of crystalline Ta₂O₅ material shown in the XRD pattern, the material has not fully crystallized. The EELS

spectrum, shown in Figure 4-11b, confirms the presence of Ta₂O₅ by the position of the band with its maxima at around 23.5 eV, which corresponds to the plasma oscillation frequency, ω_p (223). The very broad bulk plasmon band is indicative of strong carrier scattering mechanisms (high plasmon damping) in Ta₂O₅, also observed in other reports (224). The overall shape of the EELS spectrum closely resembles that of Ta₂O₅ and differs noticeably from Ta, Ta coated with a native oxide and non-stoichiometric tantalum oxide (225, 226). Bands corresponding to the Ta-O_{2,3} edge are also identified in the spectrum, which again confirm the presence of Ta in the sample. The bandgap of the Ta₂O₅, E_g can be estimated from the low energy threshold to be 4.5 eV, which falls within the range reported for Ta₂O₅ (223). The O-K edge is shown in the inset of Figure 4-11b, with a typical edge onset of 532 eV, which is expected for pentoxide bonding characteristics as in Ta₂O₅ (227). At energies below the bandgap transition, a sharp peak at 3 eV is observed which is assigned to elastic scattering by O atoms (225). However, oxygen vacancies in β -Ta₂O₅ are also known to show signature absorption peaks in this energy range. In particular, triply coordinated oxygen vacancy in β -Ta₂O₅ has been predicted to result in an EELS absorption peak at 2.9 eV due to a defect-mediated transition from an occupied level 2.1 eV above the valence band to the conduction band (228).

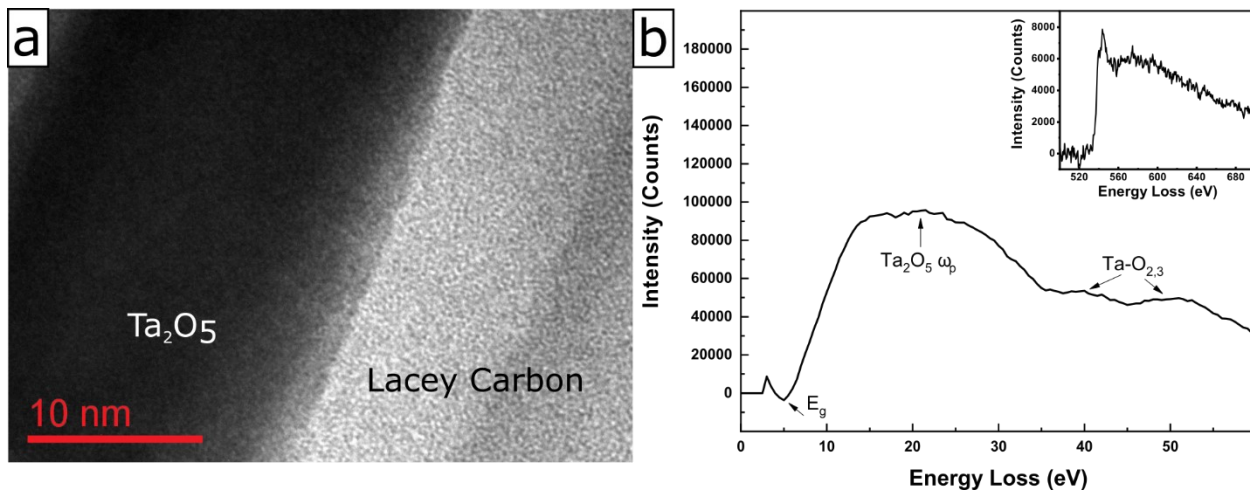


Figure 4-11: (a) HRTEM Image of Ta₂O₅ nanodimples., (b) EELS spectrum, inset showing O-K edge range

4.3.3 Au Nanoparticle Decoration and Plasmonic Photocatalysis

The nanodimple samples were decorated with Au nanoparticles; an image of the surface after decoration is shown in Figure 4-12a. The nanoparticles have a diameter of 14.6 ± 2.8 nm. The UV-Vis spectra (Figure 4-12b) show the absorption of the Ta₂O₅ nanodimples with and without Au nanoparticle decoration. The Ta₂O₅ nanodimple array exhibits a sharp band-edge at ~ 300 nm in Figure 4-12b. In addition, some weak interference fringes are visible with crests at 309 nm, 474 nm and troughs at 382 nm, 692 nm. The fringes result from constructive and destructive interference of light reflected from the air- Ta₂O₅ and Ta₂O₅-quartz interfaces (*110*). The inset of Figure 4-12b shows the Tauc plot for the direct transition of Ta₂O₅, and we note a bandgap of 4.5 eV (confirming the value obtained earlier from EELS). For Au NPs on Ta₂O₅ nanodimple arrays, a distinct LSPR resonance appears at 600 nm (red curve in Figure 4-12b). This is a relatively long wavelength for plasmonic absorption for gold nanoparticles in air or water, with plasmonic peaks usually centered around 510-530 nm for this size (229). While the red shifting of LSPR is typical for a higher dielectric constant environment around the Au NPs, the magnitude of the red-shift is suggestive of Au NPs not merely located at the Ta₂O₅-air interface but being more substantially enveloped/surrounded by Ta₂O₅. Our results are remarkably similar to those obtained by Luo et al., who embedded Au nanoparticles in Ta₂O₅ and observed a red shifting of the plasmonic peak albeit with significant peak broadening (230). Since the plasmonic enhancement of the local electromagnetic field is inversely proportional to the LSPR peak-width, broadening of the surface plasmon resonance feature is particularly undesirable. Contrastingly, we observed a narrowing of the dipolar surface plasmon extinction band with the LSPR full-width at half-maximum (FWHM) decreasing from 0.64 eV for Au NPs on glass to a FWHM value of 0.44 eV for Au NPs on Ta₂O₅

nanodimple arrays (Figure 4-13). Consequently, the quality factor (Q) of the resonance given by ω_p/FWHM increases by 27% from 3.7 to 4.7.

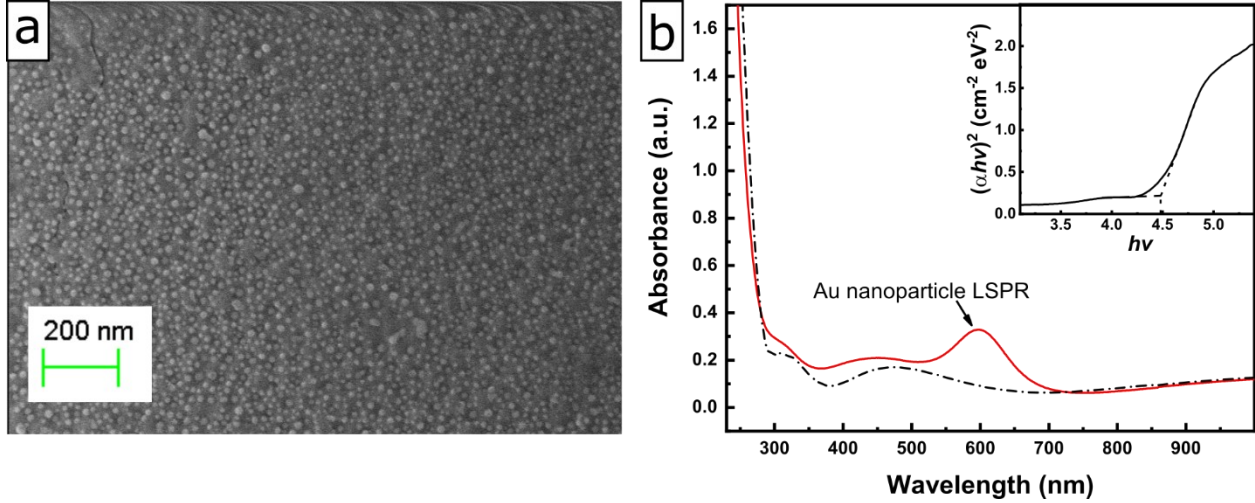


Figure 4-12: (a) HIM Image of Au nanoparticles on Ta_2O_5 nanodimples. (b) UV-Vis spectra of bare Ta_2O_5 nanodimples (black dashed line) and Ta_2O_5 nanodimples decorated with Au nanoparticles (red solid line). Inset shows Tauc plot of bare Ta_2O_5 nanodimples.

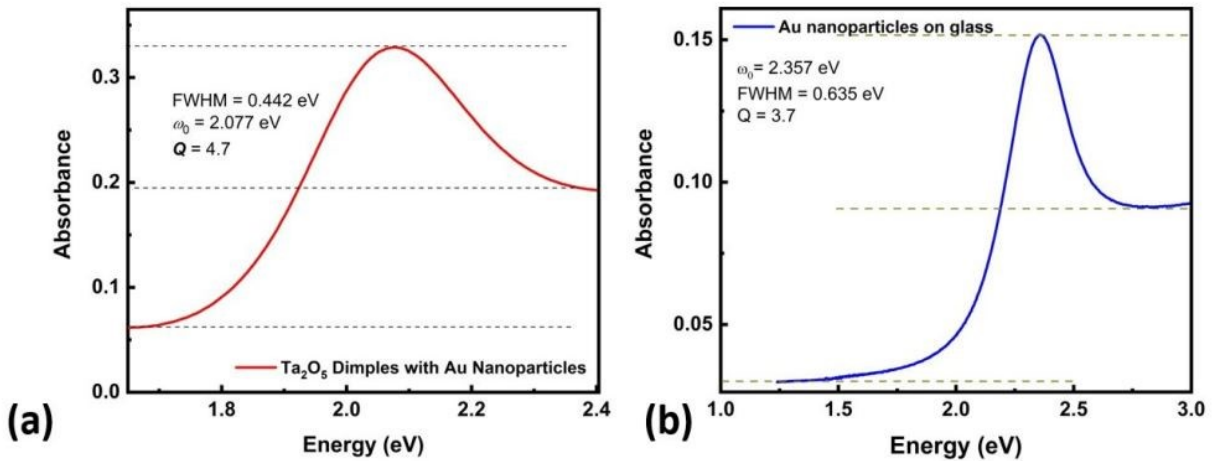


Figure 4-13: Extraction of peak-width and quality factors for gold nanoparticles on Ta_2O_5 nanodimple array (a) and on glass substrate (b)

The optical properties of the bare and Au NP coated Ta_2O_5 nanodimples were investigated using finite difference time domain (FDTD) electromagnetic simulations. The dimples were

simulated using three different specifications of pore diameters and depths corresponding to anodization voltages of 15 V, 30 V, and 40 V, based on the pore dimensions observed in Figure 4-9. For anodization voltages of 15 V, 30 V, and 40 V we use pore diameters of 25 nm, 30 nm, and 40 nm respectively, and pore depths of 2 nm, 5 nm, and 9 nm, respectively to construct the geometry. Index monitors were utilized to provide refractive index mapping of the simulated structures, as shown in Figure 4-14a-c, and helped confirm the dimples were appropriately configured and identified by the software throughout the course of the simulation. Figure 4-14d shows the simulated absorption spectra of the dimples, which reproduced the sharp band-edge and ~ 300 nm and interferometric fringes seen in experimental UV-Vis spectra. The interference fringe caused red-shifts slightly as dimple size decreases. This is probably caused by the changing local thickness of the film owing to the dimple size.

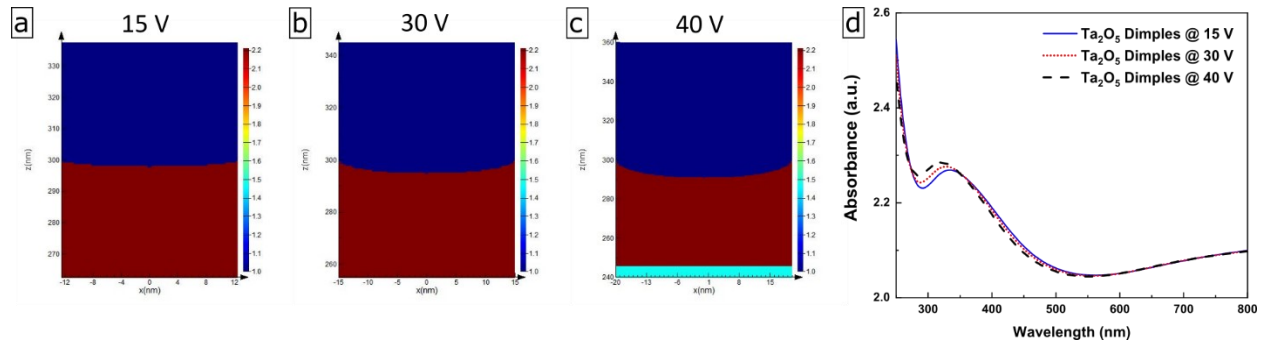


Figure 4-14: Simulated absorption spectrum of various dimple sizes.

(a)-(c) shows a schematic of the simulated dimples along with corresponding electric field intensities along the xy-plane. (d) shows the simulated absorption spectra.

Merely decorating the surface of planar Ta₂O₅ or Ta₂O₅ nanodimples with Au NPs could not reproduce the experimentally observed optical spectra. More specifically the observed red-shift of the LSPR peak was too small and could not account for the 600 nm LSPR peak shown in Figure 4-12b. Partially embedding isolated Au NPs inside planar Ta₂O₅ (Figure 4-15a) or Ta₂O₅

nanodimples (Figure 4-15b) was able to reproduce the 600 nm LSPR peak. The corresponding electric field profiles (Figure 4-15e and Figure 4-15f) show the most intense field enhancement (hot spots) close to the three component (air/gold/Ta₂O₅) interface. However, Figure 4-15a and Figure 4-15b miss the interference fringes and sharp band-edge at ~ 300 nm (due to the Ta₂O₅ electronic transition) observed in Figure 4-12b. The LSPR maximum is much broader than what is experimentally observed and they also indicate the 350-550 nm spectral range to be dominated by a monotonically increasing absorption due to the gold interband transition, which differs from the spectra of real samples. When an array of Au NPs was partially embedded in Ta₂O₅ nanodimple arrays, the simulated absorption spectrum (Figure 4-15c) reproduced all the key features seen in the experimental optical spectrum (Figure 4-12b) such as the 300 nm band-edge, the LSPR peak at 600 nm, the relatively narrow LSPR peak-width and the presence of interferometric maxima and minima along with their approximate spectra location. The corresponding electric field profile is shown in , Figure 4-15f.

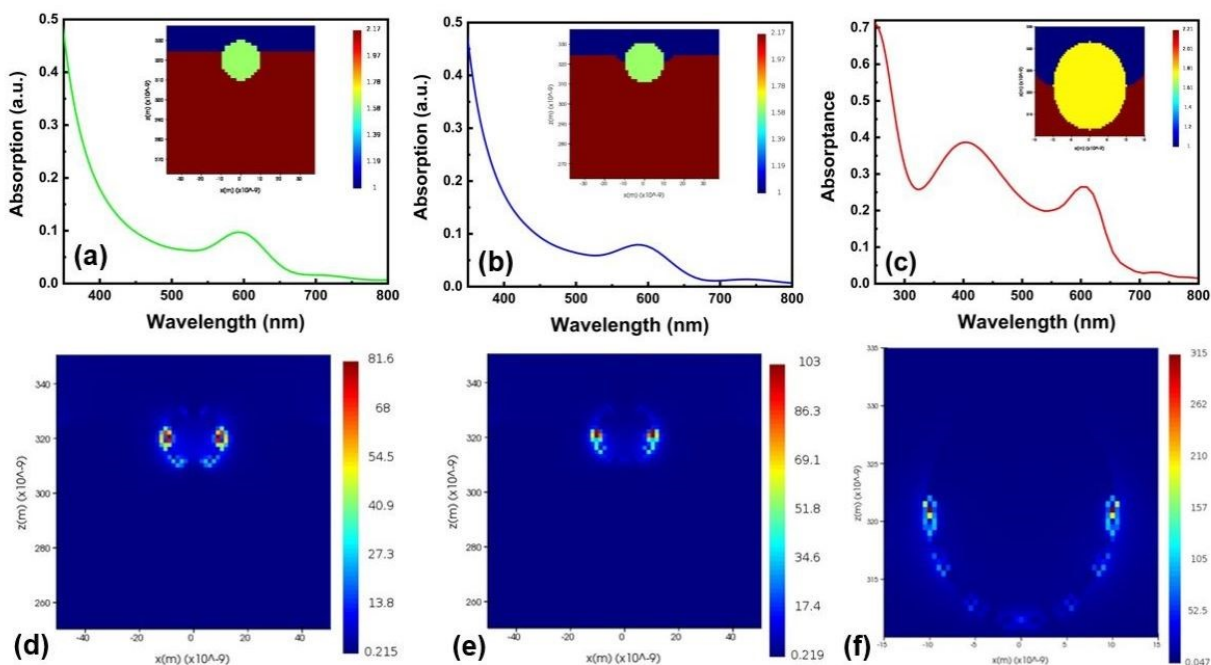


Figure 4-15: Simulated optical properties of possible Au nanoparticle/ Ta_2O_5 nanodimple configurations. (a-c) shows the simulated absorption spectra with the corresponding insets indicating the refractive index profile and (d-f) shows the corresponding electric field intensities along the xy -plane corresponding to the substrate surface. Light was normally incident on the xy plane. The figures are arranged so that each column corresponds to a different simulation, i.e. (a) and (d) correspond to the same simulation

The Au nanoparticle-decorated Ta_2O_5 nanodimples were examined for use in plasmonic visible-light induced photocatalysis. The conversion of PATP to DMAB is studied. The photocatalytic reaction is powered by the laser in a Raman microscope; the resulting SERS signal is measured, which allows for immediate feedback of the experimental results. The Raman spectra of reference PATP and DMAB is shown in Figure 4-16a, with signature peaks of PATP occurring at 1085 cm^{-1} and 1593 cm^{-1} , and the signature peaks of DMAB occurring at 1140 cm^{-1} and 1438 cm^{-1} (231, 232). It should be noted, however, that some DMAB peaks occur close to the characteristic PATP peaks, at 1078 cm^{-1} and 1558 cm^{-1} . The results of the surface reaction of PATP on bare Ta_2O_5 nanodimples, Au nanoparticles, and Au-nanoparticle decorated Ta_2O_5 nanodimples are also shown in Figure 4-16a. Bare Ta_2O_5 nanodimples show almost no conversion of PATP to

DMAB, as would be expected given the low light absorption of these samples; the intensity of the Raman signal at 1438 cm^{-1} is extremely weak, and does not even rise above the noise in the spectrum. Au nanoparticles show a modest conversion of PATP to DMAB, with relatively weak PATP and DMAB peaks appearing in the spectrum. When Ta_2O_5 nanodimples are decorated with Au nanoparticles, we observe the strongest conversion of PATB to DATB, with strong DATB peaks similar to the reference DATB sample appearing throughout and PATP peaks either completely vanishing or weak enough to be overlapped by stronger DMAB peaks. The evolution of PATP to DATB for the latter two samples is also monitored by varying the laser power from 0.1 mW to 2 mW and is shown in Figure 4-16b and Figure 4-16c. As Raman laser power increases, we observe increasing amounts of conversion of PATP to DATB based on the stronger Raman signal. The ratio of the intensity of the 1140 cm^{-1} peak (a_g mode of DMAB) to the 1080 cm^{-1} peak (a_1 mode of PATP) is widely used as a measure of the yield for DMAB formation. For Au NPs on quartz, this ratio increases from 0.10 at a laser power of 0.1 mW to 0.73 at a laser power of 2 mW (Figure 4-16c). For Ta_2O_5 -Au, this ratio increases from 0.16 at a laser power of 0.1 mW to 1.18 at a laser power of 2 mW (Figure 4-16c).

Studies of the mechanism of SERS photocatalysis are ongoing, and a full understanding of the reaction mechanism of plasmon-driven photocatalysis is still out of reach given the intertwined complexity of the multiple processes involved. However, it has been shown that a key step is the photo-activation of species by injection of plasmonic hot electrons, which are created via Landau damping when the photon frequency of incident light is in resonance with the frequency of the oscillating valence electrons on the surface of metallic nanoparticles. Two mechanisms have been proposed for this reaction: the activation of triplet oxygen by generated hot electrons which oxidate the thiols, or the oxidation of the thiols by hot holes (233, 234). Regardless of the mechanism, it

is well understood that the lifetime of hot electrons is extremely short, ranging from time scales of femtoseconds to picoseconds (235). This means that effective extraction of the hot electrons, before they undergo relaxation, is critical to an efficient photocatalytic reaction. With that in mind, the increased conversion of PATP to DATB that we observe when Ta₂O₅ nanodimples are used as the platform for the Au nanoparticles may be explained by an excitement of the electrons over or through the Schottky barrier at the interface between the materials. This is shown schematically in Figure 4-17. This extraction of hot electrons by the Ta₂O₅ can increase hot electron-density and increase photocatalytic conversion (236).

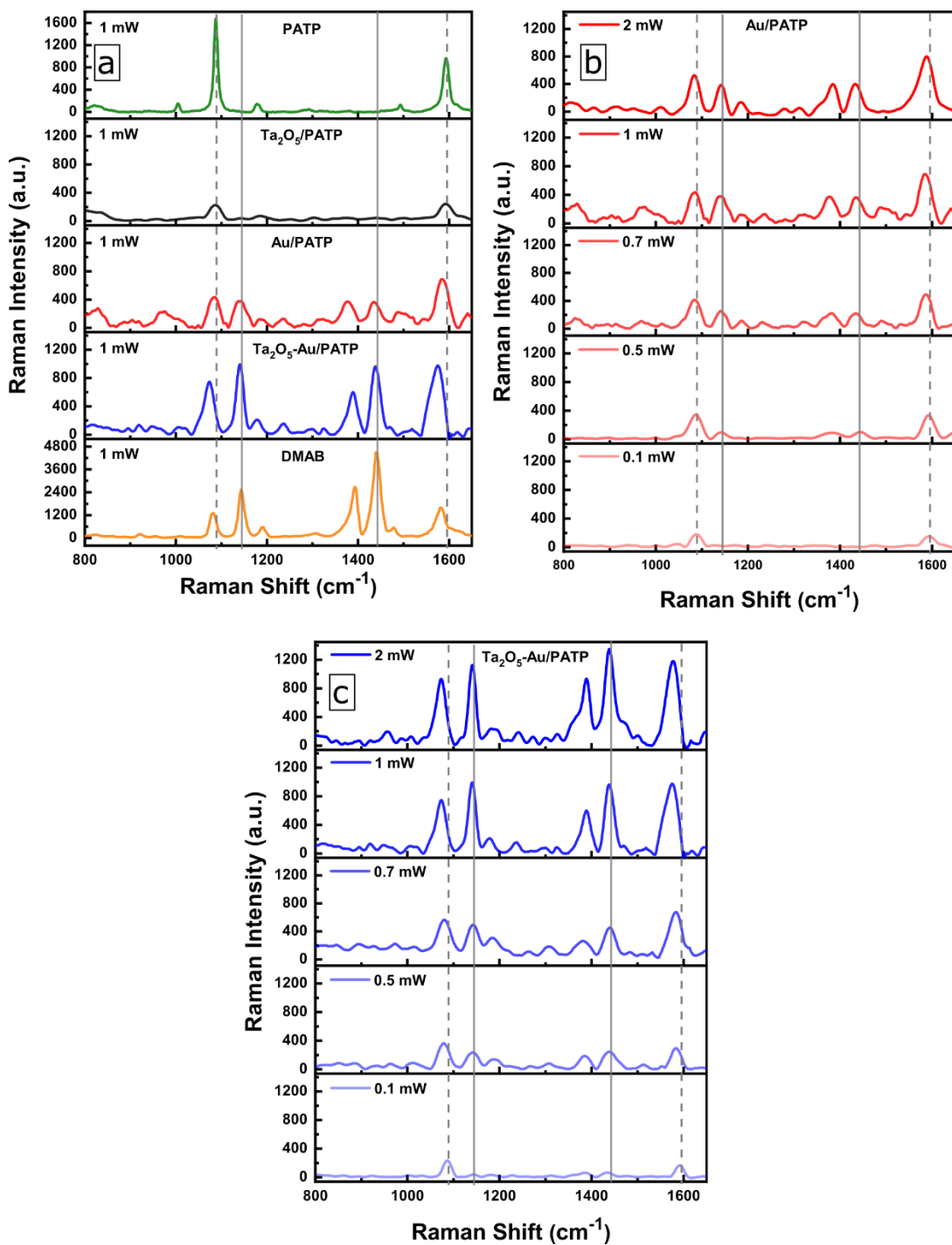


Figure 4-16: Photooxidative Raman spectra of Ta₂O₅ nanodimples

(a), from top to bottom, reference PATP, photooxidation results of PATP on bare Ta₂O₅ nanodimples, Au nanoparticles on quartz, and Au nanoparticles on Ta₂O₅ nanodimples, and reference DMAB. (b) photooxidation results of PATP on Au nanoparticles on quartz across differing Raman laser intensities. (c) photooxidation results of PATP on Au nanoparticles on Ta₂O₅ nanodimples across differing Raman laser intensities. Dashed lines show characteristic peaks of PATP and solid lines show characteristic peaks of DMAB.

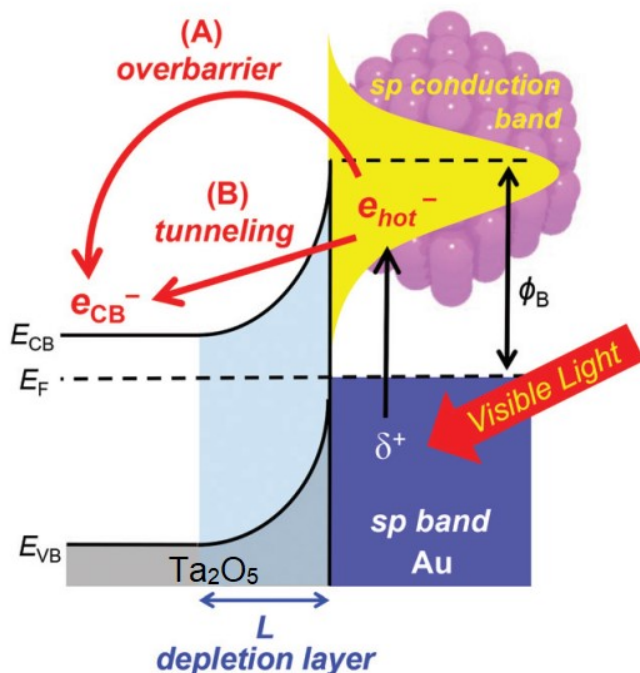


Figure 4-17: A schematic of the proposed mechanism for hot electron extraction from Au nanoparticles to Ta₂O₅. E_F , E_{VB} , E_{CB} , ϕ_B , and L are the Fermi level, valence band level, conduction band level, Schottky barrier height, and the depletion layer width, respectively. Adapted with permission from Royal Society of Chemistry (237).

4.4 Chapter Conclusion

Here again are the research sub-questions asked in this chapter, which contribute to the major research question, “What are the effects of conducting novel anodization techniques on sputtered non-native substrates?”:

1. Can Ta₂O₅ nanotubes be formed on non-native substrates, and delaminated to leave behind Ta dimples?
2. Can Ta dimples be oxidized to produce a similarly nanodimpled Ta₂O₅?
3. How do synthesis parameters control Ta anodization and the resultant morphology of both Ta and Ta₂O₅ nanodimples?
4. How does nanodimpled Ta₂O₅ perform as a platform for plasmonic photocatalysis?

We have demonstrated that nanodimpled Ta₂O₅ may be formed by anodizing Ta, delaminating the formed Ta₂O₅ nanotubes to reveal Ta dimples, and the oxidizing the Ta by annealing or a secondary anodization. This method produces an ordered nanodimpled surface that does not require the use of expensive techniques such as lithography. As tested, the ordered Ta₂O₅ nanodimples result when an anodizing range of 15 to 40 V is used, and by 2D-FFT analysis we note that the ordering is maintained after oxidation. We find that pore diameter and depth follow a linear trend increasing with anodizing voltage. At a consistent anodizing voltage, the produced film thickness is a function of anodizing time and increases predictably according to the Pillings-Bedworth ratio, with annealing; we found a experimental ratio of 2.43 which agrees well with the theoretical value of 2.47. We also found that a double-anodizing process may be used in lieu of annealing, in cases where elevated temperatures may be undesired. The Ta₂O₅ nanodimples produced an elevated photocatalytic response using a 632 nm laser for converting PATP to DMAB when used in tandem with plasmonic Au nanoparticles. This may be attributed to the relatively long wavelengths the Au nanoparticle LSPR is centered around when coupled with Ta₂O₅ (600 nm as observed by UV-Vis spectroscopy here), as indicated by the partial embedding of Au NP into the Ta₂O₅ as suggested by FDTD simulations, as well as the hot electron injection mechanism proposed by others. Finally, the nanodimples are characterized as having a band gap of 4.5 eV, as evidenced by UV-Vis and EELS measurements. In conclusion, their ease of fabrication and excellent properties means that these nanodimples have use in a wide variety of applications such as sensing, electronics, photocatalysis, and coatings.

Chapter 5: Conclusion

This thesis has investigated the effects of conducting novel anodization techniques of sputtered metallic thin films on non-native substrates. To the very best of my knowledge, the formation of these materials on non-native substrates has not been demonstrated nor investigated prior.

5.1 Key Conclusions

In Chapter 2, it is demonstrated that preferentially oriented TiO₂ nanotube arrays may be fabricated on non-native substrates. An electrolyte water content of 1 vol % and an optimal post-anodization 1.5 wt.% zinc doping process are found to lead to a optimally preferentially ordered polycrystalline grains based on the high $I_{(004)}/I_{(101)}$ of 12 observed by XRD, compared to 0.3 as is observed for randomly oriented TNTA. However, it is observed that the zinc doping process makes no discernable improvement to preferential orientation on nanotubes made with electrolyte water contents known to produce a random grain orientation; when using a 4 vol % water content electrolyte to anodize, $I_{(004)}/I_{(101)}$ remains centered around 0.3 regardless of Zn doping. This suggests that a low enough hydroxyl ion content within the nanotubes is necessary to produce a preferential orientation so that aligned crystal orientation can propagate through the nanotubes during the annealing step, as hydroxyl ions are nucleation centers for crystallization. we note that surface roughness does not affect preferential orientation as it does for anodizations conducted on metal foils. This observation makes sense in the light that the local electric field encountered at forming pores on different substrates are expected to be relatively similar to one another, given the identical sputtering conditions used on all substrates. In fact, it is observed that using a rougher substrate (FTO-coated glass) produced a greater degree of preferential orientation than a smoother

substrate (Si wafers). A possible explanation for this is the degree of lattice mismatch between the expected crystal orientation of annealed nanotubes and the with the underlying; higher degrees of lattice mismatch, as is the case with Si as opposed to SnO₂, may hinder oriented grain propagation. Further investigations into the resultant properties of preferential orientation show that preferred orientation has mixed effects. When utilized as a photoconductor, higher levels of trapping in preferentially oriented nanotubes (attributed to adsorption of oxygen to more exposed {100} facets) lead to a decrease on responsivity from 523 A/W to 36.5 A/W; however, as the surface is not exposed to ambient air in the case of perovskite solar cells, higher power conversion efficiencies are noted in solar cells made with preferentially oriented nanotubes. A 1 vol % water electrolyte corresponding to TNTAs with a $I_{(004)}/I_{(101)}$ of 2.3 led to an average PCE of 10.5% PCE, while a 4 vol% water electrolyte corresponding to TNTAs with a $I_{(004)}/I_{(101)}$ of 0.3 led to an average PCE of 6.1% PCE. When used as the electron transport layer in halide perovskite solar cells, Zn-doped TNTAs exhibited a poorer solar cell performance compared to undoped TNTA samples. For example, when using a 1 vol.% water electrolyte, a Zn-TNTA corresponding to a $I_{(004)}/I_{(101)}$ of 7 only achieved an average PCE of 9.0%. The reason for this is not clear but may be related to increased electron-hole recombination. Nevertheless, these results show that inducing preferential orientation is a powerful method to tailor TiO₂ nanotube properties.

In Chapter 3, nanoporous NiO is demonstrated to form from sputtered films of NiO on non-native substrates. By XRD and XPS characterization, this film is proven to be NiO_x(OH)_y after anodization, which upon annealing becomes NiO. Further characterizations confirmed that the NiO is p-type, with a band gap of 3.5 eV and a charge carrier density of $2.85 \times 10^{18} \text{ cm}^{-3}$, values well within an expected range for NiO. The roughness of the substrate is demonstrated be an important factor for resulting morphology when considering anodized Ni films, much more so than other

metals; by SEM observations, the morphology of the anodized films are remarkably different across FTO, ITO, and Si substrates. This is explained to occur because $\text{NiO}_x(\text{OH})_y$ is much more susceptible to chemical etching than other anodized materials; this susceptibility to chemical etching is also what makes the formation of NiO nanotubes so difficult. Etching, which typically concentrates on grain boundaries due to the presence of local electric field hot spots, becomes increasingly pronounced when chemical etching rates are higher. As a result, on rougher substrates such as FTO-coated glass there are distinct pitting formations at grain boundaries, to the extent that evidence of grain boundaries are still visible after anodizing. In the case of a smoother ITO-coated substrate, there is no visible evidence of the original grain boundaries, and on the smoothest substrate of Si, the most uniform ordered morphology results. Another identified influence the substrate has on the nanoporous films occurs during the annealing step of fabrication. In the case of an Si substrate, the formation of a distinct NiSi layer is noted to form upon annealing by XRD. This observation highlights the importance of the mass diffusivity between substrate and anodized film at the elevated temperatures often used during annealing to produce a stoichiometric, crystalline films. Presumably, some small amount of diffusion frequently takes place between film and substrate takes place at elevated temperatures; however, it is only in this instance that diffusion is detected. This insight highlights the importance of either using lower-temperature annealing processes or avoiding them entirely when dealing with two materials with high mass diffusivity.

In Chapter 4, it is shown that Ta nanodimples may be formed after removal of anodized Ta_2O_5 nanotubes on sputtered Ta films. Ta nanodimple diameter and depth are shown to be linearly dependent on the anodizing voltage, and nanodimples are demonstrated to form best in an anodization voltage range of 15-40 V. The dimples may be converted from Ta to Ta_2O_5 by thermal or anodic oxidation; the thermal oxidation method proved superior to anodic oxidation, which

tended to result in partial film delamination. The oxidation process also impacted morphology of the dimples; as Ta expands as it is converted into oxide, there is a decrease in pore diameter and depth after annealing. Furthermore, the layer thickness under annealing is observed to expand according to the Pillings-Bedworth ratio, observed to be 2.43 which is comparable to the 2.47 as predicted by theory. The degree of dimple ordering can be said to be maintained after annealing. By 2D-FFT analysis of SEM images, an excellent degree of ordering is seen to remain after annealing. XRD results suggest that the Ta₂O₅ produced by annealing is crystalline, although HRTEM analysis indicates that crystallization may not have been complete at the annealing time or temperature used in this study. UV-Vis and EELS absorption spectra indicate that the band gap of the Ta₂O₅ is 4.5 eV. Coating the Ta nanodimples with a gold film and annealing the composite produces Au nanoparticle coated Ta₂O₅ nanodimple arrays with a relatively narrow localized surface plasmon resonance (LSPR) at 600 nm, redshifted by 75 nm from the LSPR maximum of Au nanoparticles on SiO₂. FDTD modeling of the observed optical properties indicates Au NPs to be at least partially embedded in the Ta₂O₅. Based on the strong Raman intensity observed of characteristic DMAB peaks and diminished intensity of PATP peaks, the results of these experiments show that the hybrid system of Au nanoparticles and Ta₂O₅ nanodimples outperform either of these materials when used individually. This elevated photocatalytic response suggests that Ta₂O₅ may be able to extract generated hot electrons from the Au nanoparticles, thus increasing the photocatalytic reaction.

5.2 Future Work

The following is some recommendations how the contributions of this thesis might be built upon in the future:

With preferentially oriented nanotubes on non-native substrates demonstrated, there are many possibilities to further investigate the resulting effects in applications. The heightened exposure of {100} facets means that adsorption of gaseous molecules can be expected to change, which would have significant effects on photocatalytic reaction rates. For this reason, CO₂ photoreduction is a prime topic for further experiment. Preferential orientation may also affect noble metal and thin film formation, which presents intriguing possibilities in plasmonic photocatalysis. I hypothesize that the preferentially oriented exposed crystal facets would result in improved heteroepitaxy between the nanotubes and a deposited material. This in turn can be expected to result in an effect on charge transfer, most interestingly on hot electron injection. An effect like this would be also useful for photocatalysis, and CO₂ photoreduction is again a prime focal point for these studies. It would also be useful to clarify the effect of the substrate material on resulting preferential orientation, which could be done by producing preferentially oriented nanotubes on differing material substrates that all possess identical roughness; a simple experiment to do this would be to anodize sputtered films of Ti on single-crystal wafers of not only Si but also GaN, TiO₂, Al₂O₃, etc.

Nanoporous NiO, being one of the few p-type metal oxide semiconductors, has potential for uses in devices such as a photocathode and as a hole transporting layer. The porous structure would lend strength to its integration with noble metal nanoparticles, drop-cast or spin-coated solvents, etc. It would also be interesting to further investigate nanodimpled Ta₂O₅ as a photoanode, especially with respect to the beneficial loading of Au nanoparticles. Conversion of the Ta₂O₅ to Ta₃N₅ would also be interesting to study for photocatalysis, given its excellent band structure for water-splitting. It is worth noting that across previous literature, Ta₃N₅ conversion from Ta₂O₅ nanotubes is done when photocatalytic water splitting is of interest by annealing in the presence

of NH_3 , and experimental procedure that would be easily accomplished with the nanodimples demonstrated here as well. Both nanoporous NiO and nanodimpled Ta_2O_5 would also be interesting to utilize in studies on thin-film optical interference devices owing to their tunable structure and high refractive index.

Lastly, in the context of the anodization technique's potential for large scale fabrication, there is a need to further investigate anodizations on non-conductive substrates such as glass and polymers. As anodizing proceeds, the metal is consumed and if the underlying substrate is not itself conductive, and the resistance increases. In the case of the relatively small substrates as used in this thesis research and across all previous research to date, there is no observable change in morphology or properties in the anodized films across the substrate. However, when scaled up, enough of a voltage drop across the substrate would be expected to produce noticeable differences in the anodized films; for example, hydroxyl ion incorporation during TiO_2 nanotube formation would be expected to change, resulting in a weaker or stronger preferential orientation across a substrate. This problem can probably be solved by an appropriate configuration when anodizing; for example, a conductive passthrough through the insulating substrate at spaced intervals or across the top surface of the anodized metal, but as of now there is no protocol for conducting such large-scale anodizations on non-conductive substrates. Such a series of experiments would build upon the experimental protocols and optimizations identified throughout this thesis and would be another significant step forward towards the use of anodized metal-oxide nanostructures in real-world applications.

Bibliography

1. G. K. Mor, K. Shankar, M. Paulose, O. K. Varghese, C. A. Grimes, Use of Highly-Ordered TiO₂ Nanotube Arrays in Dye-Sensitized Solar Cells. *Nano Letters* **6**, 215-218 (2006).
2. U. Thakur, R. Kisslinger, K. Shankar, One-Dimensional Electron Transport Layers for Perovskite Solar Cells. *Nanomaterials* **7**, 95 (2017).
3. P. Roy, R. Kisslinger, S. Farsinezhad, N. Mahdi, A. Bhatnagar, A. Hosseini, L. Bu, W. Hua, B. D. Wiltshire, A. Eisenhawer, P. Kar, K. Shankar, All-solution processed, scalable superhydrophobic coatings on stainless steel surfaces based on functionalized discrete titania nanotubes. *Chemical Engineering Journal* **351**, 482-489 (2018).
4. J. M. Runge, A Brief History of Anodizing Aluminum, in *The Metallurgy of Anodizing Aluminum: Connecting Science to Practice*. (Springer International Publishing, Cham, 2018), pp. 65-148.
5. K. Shankar, G. K. Mor, H. E. Prakasam, S. Yoriya, M. Paulose, O. K. Varghese, C. A. Grimes, Highly-ordered TiO₂ nanotube arrays up to 220 μm in length: use in water photoelectrolysis and dye-sensitized solar cells. *Nanotechnology* **18**, 065707 (2007).
6. O. K. Varghese, M. Paulose, T. J. LaTempa, C. A. Grimes, High-Rate Solar Photocatalytic Conversion of CO₂ and Water Vapor to Hydrocarbon Fuels. *Nano Letters* **9**, 731-737 (2009).
7. C. W. Lai, J. C. Juan, W. B. Ko, S. Bee Abd Hamid, An Overview: Recent Development of Titanium Oxide Nanotubes as Photocatalyst for Dye Degradation. *International Journal of Photoenergy* **2014**, 524135 (2014).
8. A. Auer, J. Kunze-Liebhäuser, Recent Progress in Understanding Ion Storage in Self-Organized Anodic TiO₂ Nanotubes. *Small Methods* **3**, 1800385 (2019).
9. S. Yoriya, H. E. Prakasam, O. K. Varghese, K. Shankar, M. Paulose, G. K. Mor, T. J. Latempa, C. A. Grimes, Initial Studies on the Hydrogen Gas Sensing Properties of Highly-

- Ordered High Aspect Ratio TiO₂ Nanotube-Arrays 20 μm to 222 μm in Length. *Sensor Letters* **4**, 334-339 (2006).
10. M. R. Nickel, G. Melligan, T. P. W. McMullen, R. E. Burrell, The effect of chemical additives in phosphoric acid anodization of aluminum-tantalum thin films. *Thin Solid Films* **685**, 245-253 (2019).
 11. T. Li, K. Gulati, N. Wang, Z. Zhang, S. Ivanovski, Understanding and augmenting the stability of therapeutic nanotubes on anodized titanium implants. *Materials Science and Engineering: C* **88**, 182-195 (2018).
 12. L. Meyer, S. Brinkman, L. van Kesteren, N. Leprince-Ringuet, F. van Boxmeer, IPCC, 2014: Climate Change 2014: Synthesis Report. Contribution of Working Groups I, II and III to the Fifth Assessment Report of the Intergovernmental Panel on Climate Change, (2014).
 13. J. Rogelj, G. Luderer, R. C. Pietzcker, E. Kriegler, M. Schaeffer, V. Krey, K. Riahi, Energy system transformations for limiting end-of-century warming to below 1.5 °C. *Nature Climate Change* **5**, 519 (2015).
 14. International Renewable Energy Agency, Renewable Power Generation Costs in 2019, (2020).
 15. N. S. Lewis, D. G. Nocera, Powering the planet: Chemical challenges in solar energy utilization. *Proceedings of the National Academy of Sciences* **103**, 15729-15735 (2006).
 16. S. Koochi-Fayegh, M. A. Rosen, A review of energy storage types, applications and recent developments. *Journal of Energy Storage* **27**, 101047 (2020).
 17. C.-J. Winter, Hydrogen energy — Abundant, efficient, clean: A debate over the energy-system-of-change. *International Journal of Hydrogen Energy* **34**, S1-S52 (2009).
 18. International Organization for Standardization, ISO/TS 80004-1:2015, Nanotechnologies — Vocabulary — Part 1: Core terms (2015).

19. P. K. Jain, X. Huang, I. H. El-Sayed, M. A. El-Sayed, Noble Metals on the Nanoscale: Optical and Photothermal Properties and Some Applications in Imaging, Sensing, Biology, and Medicine. *Accounts of Chemical Research* **41**, 1578-1586 (2008).
20. P. Reineck, D. Brick, P. Mulvaney, U. Bach, Plasmonic Hot Electron Solar Cells: The Effect of Nanoparticle Size on Quantum Efficiency. *The Journal of Physical Chemistry Letters* **7**, 4137-4141 (2016).
21. B. Hou, L. Shen, H. Shi, R. Kapadia, S. B. Cronin, Hot electron-driven photocatalytic water splitting. *Physical Chemistry Chemical Physics* **19**, 2877-2881 (2017).
22. D. S. Alexei, N. G. Gregory, S. Roman, Hot-electron effect in superconductors and its applications for radiation sensors. *Superconductor Science and Technology* **15**, R1 (2002).
23. B. R. Nag, *Theory of Electrical Transport in Semiconductors*. (Pergamon, Oxford, 1972).
24. J. van de Lagemaat, A. J. Frank, Nonthermalized Electron Transport in Dye-Sensitized Nanocrystalline TiO₂ Films: Transient Photocurrent and Random-Walk Modeling Studies. *The Journal of Physical Chemistry B* **105**, 11194-11205 (2001).
25. D. R. Baker, P. V. Kamat, Photosensitization of TiO₂ Nanostructures with CdS Quantum Dots: Particulate versus Tubular Support Architectures. *Advanced Functional Materials* **19**, 805-811 (2009).
26. A. Ghicov, S. P. Albu, R. Hahn, D. Kim, T. Stergiopoulos, J. Kunze, C.-A. Schiller, P. Falaras, P. Schmuki, TiO₂ Nanotubes in Dye-Sensitized Solar Cells: Critical Factors for the Conversion Efficiency. *Chemistry – An Asian Journal* **4**, 520-525 (2009).
27. T. Guo, M.-S. Yao, Y.-H. Lin, C.-W. Nan, A comprehensive review on synthesis methods for transition-metal oxide nanostructures. *CrystEngComm* **17**, 3551-3585 (2015).
28. S. M. Amorim, J. Suave, L. Andrade, A. M. Mendes, H. J. José, R. F. P. M. Moreira, Towards an efficient and durable self-cleaning acrylic paint containing mesoporous TiO₂ microspheres. *Progress in Organic Coatings* **118**, 48-56 (2018).

29. M. Shinsuke, I. Junpei, Y. Akira, K. Makoto, High Quality Aluminum Oxide Passivation Layer for Crystalline Silicon Solar Cells Deposited by Parallel-Plate Plasma-Enhanced Chemical Vapor Deposition. *Applied Physics Express* **3**, 012301 (2010).
30. X. Li, F. Xie, S. Zhang, J. Hou, W. C. H. Choy, MoO₂ and V₂O_x as hole and electron transport layers through functionalized intercalation in normal and inverted organic optoelectronic devices. *Light: Science & Applications* **4**, e273 (2015).
31. G. F. Fine, L. M. Cavanagh, A. Afonja, R. Binions, Metal Oxide Semi-Conductor Gas Sensors in Environmental Monitoring. *Sensors* **10**, 5469-5502 (2010).
32. M. D. Hernandez-Alonso, F. Fresno, S. Suarez, J. M. Coronado, Development of alternative photocatalysts to TiO₂: Challenges and opportunities. *Energy & Environmental Science* **2**, 1231-1257 (2009).
33. J. A. Turner, Sustainable Hydrogen Production. *Science* **305**, 972-974 (2004).
34. M. A. Green, Commercial progress and challenges for photovoltaics. *Nature Energy* **1**, 15015 (2016).
35. Technavio, Aluminum Extrusion Market by Product, End-user, and Geography - Forecast and Analysis 2020-2024, (2020).
36. P. Roy, S. Berger, P. Schmuki, TiO₂ Nanotubes: Synthesis and Applications. *Angewandte Chemie International Edition* **50**, 2904-2939 (2011).
37. L. V. Taveira, J. M. Macak, K. Sirotna, L. F. P. Dick, P. Schmuki, Voltage Oscillations and Morphology during the Galvanostatic Formation of Self-Organized TiO₂ Nanotubes. *Journal of the Electrochemical Society* **153**, B137 (2006).
38. A. Valota, D. J. LeClere, T. Hashimoto, P. Skeldon, G. E. Thompson, S. Berger, J. Kunze, P. Schmuki, The efficiency of nanotube formation on titanium anodized under voltage and current control in fluoride/glycerol electrolyte. *Nanotechnology* **19**, 355701 (2008).

39. W. Lee, S.-J. Park, Porous Anodic Aluminum Oxide: Anodization and Templated Synthesis of Functional Nanostructures. *Chemical Reviews* **114**, 7487-7556 (2014).
40. H. Masuda, K. Fukuda, Ordered Metal Nanohole Arrays Made by a Two-Step Replication of Honeycomb Structures of Anodic Alumina. *Science* **268**, 1466-1468 (1995).
41. M. Assefpour-Dezfuly, C. Vlachos, E. H. Andrews, Oxide morphology and adhesive bonding on titanium surfaces. *Journal of Materials Science* **19**, 3626-3639 (1984).
42. V. Zwillling, E. Darque-Ceretti, A. Boutry-Forveille, D. David, M. Y. Perrin, M. Aucouturier, Structure and physicochemistry of anodic oxide films on titanium and TA6V alloy. *Surface and Interface Analysis* **27**, 629-637 (1999).
43. Y. Yang, S. P. Albu, D. Kim, P. Schmuki, Enabling the Anodic Growth of Highly Ordered V₂O₅ Nanoporous/Nanotubular Structures. *Angewandte Chemie International Edition* **50**, 9071-9075 (2011).
44. H. E. Prakasam, O. K. Varghese, M. Paulose, G. K. Mor, C. A. Grimes, Synthesis and photoelectrochemical properties of nanoporous iron (III) oxide by potentiostatic anodization. *Nanotechnology* **17**, 4285-4291 (2006).
45. C.-Y. Lee, K. Lee, P. Schmuki, Anodic Formation of Self-Organized Cobalt Oxide Nanoporous Layers. *Angewandte Chemie International Edition* **52**, 2077-2081 (2013).
46. C. Hu, K. Chu, Y. Zhao, W. Y. Teoh, Efficient Photoelectrochemical Water Splitting over Anodized p-Type NiO Porous Films. *ACS Applied Materials & Interfaces* **6**, 18558-18568 (2014).
47. P. Kar, M. K. El-Tahlawy, Y. Zhang, M. Yassin, N. Mahdi, R. Kisslinger, U. K. Thakur, A. M. Askar, R. Fedosejevs, K. Shankar, Anodic copper oxide nanowire and nanopore arrays with mixed phase content: synthesis, characterization and optical limiting response. *Journal of Physics Communications* **1**, 045012 (2017).

48. N. K. Shrestha, K. Lee, R. Hahn, P. Schmuki, Anodic growth of hierarchically structured nanotubular ZnO architectures on zinc surfaces using a sulfide based electrolyte. *Electrochemistry Communications* **34**, 9-13 (2013).
49. B. Pandey, P. S. Thapa, D. A. Higgins, T. Ito, Formation of Self-Organized Nanoporous Anodic Oxide from Metallic Gallium. *Langmuir* **28**, 13705-13711 (2012).
50. H. Tsuchiya, P. Schmuki, Thick self-organized porous zirconium oxide formed in H₂SO₄/NH₄F electrolytes. *Electrochemistry Communications* **6**, 1131-1134 (2004).
51. I. Sieber, H. Hildebrand, A. Friedrich, P. Schmuki, Formation of self-organized niobium porous oxide on niobium. *Electrochemistry Communications* **7**, 97-100 (2005).
52. H.-C. Shin, J. Dong, M. Liu, Porous Tin Oxides Prepared Using an Anodic Oxidation Process. *Advanced Materials* **16**, 237-240 (2004).
53. H. Tsuchiya, P. Schmuki, Self-organized high aspect ratio porous hafnium oxide prepared by electrochemical anodization. *Electrochemistry Communications* **7**, 49-52 (2005).
54. I. Sieber, B. Kannan, P. Schmuki, Self-Assembled Porous Tantalum Oxide Prepared in H₂SO₄/HF Electrolytes. *Electrochemical and Solid-State Letters* **8**, J10 (2005).
55. N. Mukherjee, M. Paulose, O. K. Varghese, G. K. Mor, C. A. Grimes, Fabrication of nanoporous tungsten oxide by galvanostatic anodization. *Journal of Materials Research* **18**, 2296-2299 (2003).
56. R. Hang, Y. Liu, L. Zhao, A. Gao, L. Bai, X. Huang, X. Zhang, B. Tang, P. K. Chu, Fabrication of Ni-Ti-O nanotube arrays by anodization of NiTi alloy and their potential applications. *Scientific Reports* **4**, 7547 (2014).
57. M. Qadir, J. Lin, A. Biesiekierski, Y. Li, C. Wen, Effect of Anodized TiO₂-Nb₂O₅-ZrO₂ Nanotubes with Different Nanoscale Dimensions on the Biocompatibility of a Ti₃₅Zr₂₈Nb Alloy. *ACS Applied Materials & Interfaces* **12**, 6776-6787 (2020).

58. D. Regonini, C. R. Bowen, A. Jaroenworarluck, R. Stevens, A review of growth mechanism, structure and crystallinity of anodized TiO₂ nanotubes. *Materials Science and Engineering: R: Reports* **74**, 377-406 (2013).
59. J. P. O'Sullivan, G. C. Wood, The Morphology and Mechanism of Formation of Porous Anodic Films on Aluminium. *Proceedings of the Royal Society of London. Series A, Mathematical and Physical Sciences* **317**, 511-543 (1970).
60. S. P. Albu, A. Ghicov, S. Aldabergenova, P. Drechsel, D. LeClere, G. E. Thompson, J. M. Macak, P. Schmuki, Formation of Double-Walled TiO₂ Nanotubes and Robust Anatase Membranes. *Advanced Materials* **20**, 4135-4139 (2008).
61. P. Mishra, K. R. Hebert, Flow Instability Mechanism for Formation of Self-Ordered Porous Anodic Oxide Films. *Electrochimica Acta* **222**, 1186-1190 (2016).
62. A. Baron-Wiecheć, M. G. Burke, T. Hashimoto, H. Liu, P. Skeldon, G. E. Thompson, H. Habazaki, J. J. Ganem, I. C. Vickridge, Tracer study of pore initiation in anodic alumina formed in phosphoric acid. *Electrochimica Acta* **113**, 302-312 (2013).
63. D. J. LeClere, A. Velota, P. Skeldon, G. E. Thompson, S. Berger, J. Kunze, P. Schmuki, H. Habazaki, S. Nagata, Tracer Investigation of Pore Formation in Anodic Titania. *Journal of the Electrochemical Society* **155**, C487 (2008).
64. P. Skeldon, G. E. Thompson, S. J. Garcia-Vergara, L. Iglesias-Rubianes, C. E. Blanco-Pinzon, A Tracer Study of Porous Anodic Alumina. *Electrochemical and Solid-State Letters* **9**, B47 (2006).
65. S. Berger, S. P. Albu, F. Schmidt-Stein, H. Hildebrand, P. Schmuki, J. S. Hammond, D. F. Paul, S. Reichlmaier, The origin for tubular growth of TiO₂ nanotubes: A fluoride rich layer between tube-walls. *Surface Science* **605**, L57-L60 (2011).
66. W. Wei, S. Berger, C. Hauser, K. Meyer, M. Yang, P. Schmuki, Transition of TiO₂ nanotubes to nanopores for electrolytes with very low water contents. *Electrochemistry Communications* **12**, 1184-1186 (2010).

67. J. M. Macak, S. P. Albu, P. Schmuki, Towards ideal hexagonal self-ordering of TiO₂ nanotubes. *physica status solidi (RRL) – Rapid Research Letters* **1**, 181-183 (2007).
68. K. R. Hebert, S. P. Albu, I. Paramasivam, P. Schmuki, Morphological instability leading to formation of porous anodic oxide films. *Nature Materials* **11**, 162-166 (2012).
69. V. P. Parkhutik, V. I. Shershulsky, Theoretical modelling of porous oxide growth on aluminium. *Journal of Physics D: Applied Physics* **25**, 1258-1263 (1992).
70. C. Sample, A. A. Golovin, Formation of porous metal oxides in the anodization process. *Physical Review E* **74**, 041606 (2006).
71. L. G. Stanton, A. A. Golovin, Effect of ion migration on the self-assembly of porous nanostructures in anodic oxides. *Physical Review B* **79**, 035414 (2009).
72. K. Yasuda, J. M. Macak, S. Berger, A. Ghicov, P. Schmuki, Mechanistic Aspects of the Self-Organization Process for Oxide Nanotube Formation on Valve Metals. *Journal of the Electrochemical Society* **154**, C472 (2007).
73. A. Anders, A structure zone diagram including plasma-based deposition and ion etching. *Thin Solid Films* **518**, 4087-4090 (2010).
74. J. A. Thornton, Influence of apparatus geometry and deposition conditions on the structure and topography of thick sputtered coatings. *Journal of Vacuum Science and Technology* **11**, 666-670 (1974).
75. S. Farsinezhad, A. N. Dalrymple, K. Shankar, Toward single-step anodic fabrication of monodisperse TiO₂ nanotube arrays on non-native substrates. *physica status solidi (a)* **211**, 1113-1121 (2014).
76. K. N. Chappanda, Y. R. Smith, L. W. Rieth, P. Tathireddy, M. Misra, S. K. Mohanty, Effect of Sputtering Parameters on the Morphology of TiO₂ Nanotubes Synthesized From Thin Ti Film on Si Substrate. *IEEE Transactions on Nanotechnology* **14**, 18-25 (2015).

77. J. A. Thornton, High Rate Thick Film Growth. *Annual Review of Materials Science* **7**, 239-260 (1977).
78. C. Charpentier, P. Prod'homme, I. Maurin, M. Chaigneau, P. Roca i Cabarrocas, X-Ray diffraction and Raman spectroscopy for a better understanding of ZnO:Al growth process. *EPJ Photovolt.* **2**, 25002 (2011).
79. R. C. Furneaux, W. R. Rigby, A. P. Davidson, The formation of controlled-porosity membranes from anodically oxidized aluminium. *Nature* **337**, 147-149 (1989).
80. D. Gong, C. A. Grimes, O. K. Varghese, W. Hu, R. S. Singh, Z. Chen, E. C. Dickey, Titanium oxide nanotube arrays prepared by anodic oxidation. *Journal of Materials Research* **16**, 3331-3334 (2001).
81. Q. Cai, M. Paulose, O. K. Varghese, C. A. Grimes, The Effect of Electrolyte Composition on the Fabrication of Self-Organized Titanium Oxide Nanotube Arrays by Anodic Oxidation. *Journal of Materials Research* **20**, 230-236 (2005).
82. J. M. Macák, H. Tsuchiya, P. Schmuki, High-Aspect-Ratio TiO₂ Nanotubes by Anodization of Titanium. *Angewandte Chemie International Edition* **44**, 2100-2102 (2005).
83. M. Paulose, K. Shankar, S. Yoriya, H. E. Prakasam, O. K. Varghese, G. K. Mor, T. A. Latempa, A. Fitzgerald, C. A. Grimes, Anodic Growth of Highly Ordered TiO₂ Nanotube Arrays to 134 μm in Length. *The Journal of Physical Chemistry B* **110**, 16179-16184 (2006).
84. H. E. Prakasam, K. Shankar, M. Paulose, O. K. Varghese, C. A. Grimes, A new benchmark for TiO₂ nanotube array growth by anodization. *Journal of Physical Chemistry C* **111**, 7235-7241 (2007).
85. A. El Ruby Mohamed, S. Rohani, Modified TiO₂ nanotube arrays (TNTAs): progressive strategies towards visible light responsive photoanode, a review. *Energy & Environmental Science* **4**, 1065-1086 (2011).

86. S. Zeng, E. Vahidzadeh, C. G. VanEssen, P. Kar, R. Kisslinger, A. Goswami, Y. Zhang, N. Mahdi, S. Riddell, A. E. Kobryn, S. Gusarov, P. Kumar, K. Shankar, Optical control of selectivity of high rate CO₂ photoreduction via interband- or hot electron Z-scheme reaction pathways in Au-TiO₂ plasmonic photonic crystal photocatalyst. *Applied Catalysis B: Environmental* **267**, 118644 (2020).
87. E. Üzer, P. Kumar, R. Kisslinger, P. Kar, U. K. Thakur, S. Zeng, K. Shankar, T. Nilges, Vapor Deposition of Semiconducting Phosphorus Allotropes into TiO₂ Nanotube Arrays for Photoelectrocatalytic Water Splitting. *ACS Applied Nano Materials* **2**, 3358-3367 (2019).
88. E. Üzer, P. Kumar, R. Kisslinger, P. Kar, U. K. Thakur, K. Shankar, T. Nilges, Vapor growth of binary and ternary phosphorus-based semiconductors into TiO₂ nanotube arrays and application in visible light driven water splitting. *Nanoscale Advances* **1**, 2881-2890 (2019).
89. J. M. Runge, Base Metal Microstructural Considerations for Anodizing Aluminum Substrates, in *The Metallurgy of Anodizing Aluminum: Connecting Science to Practice*. (Springer International Publishing, Cham, 2018), pp. 373-431.
90. S. Leonardi, V. Russo, A. Li Bassi, F. Di Fonzo, T. M. Murray, H. Efstathiadis, A. Agnoli, J. Kunze-Liebhäuser, TiO₂ Nanotubes: Interdependence of Substrate Grain Orientation and Growth Rate. *ACS Applied Materials & Interfaces* **7**, 1662-1668 (2015).
91. J. M. Macak, M. Jarosova, A. Jäger, H. Sopha, M. Klementová, Influence of the Ti microstructure on anodic self-organized TiO₂ nanotube layers produced in ethylene glycol electrolytes. *Applied Surface Science* **371**, 607-612 (2016).
92. H. Sopha, A. Jäger, P. Knotek, K. Tesař, M. Jarosova, J. M. Macak, Self-organized Anodic TiO₂ Nanotube Layers: Influence of the Ti substrate on Nanotube Growth and Dimensions. *Electrochimica Acta* **190**, 744-752 (2016).

93. H. Sopha, K. Tesar, P. Knotek, A. Jäger, L. Hromadko, J. M. Macak, TiO₂ nanotubes grown on Ti substrates with different microstructure. *Materials Research Bulletin* **103**, 197-204 (2018).
94. T. H. Choudhury, S. Raghavan, Anodization of sputtered metallic films: The microstructural connection. *Scripta Materialia* **105**, 18-21 (2015).
95. S. Farsinezhad, A. Mohammadpour, M. Benlamri, A. N. Dalrymple, K. Shankar, The Morphology of TiO₂ Nanotube Arrays Grown from Atomically Peened and Non-Atomically Peened Ti Films. *Journal of Nanoscience and Nanotechnology* **17**, 4936-4945 (2017).
96. A. L. Adams, M. Klings, G. C. Fischer, L. Vroman, Three simple ways to detect antibody—Antigen complex on flat surfaces. *Journal of Immunological Methods* **3**, 227-232 (1973).
97. G. K. Mor, O. K. Varghese, M. Paulose, C. A. Grimes, Transparent Highly Ordered TiO₂ Nanotube Arrays via Anodization of Titanium Thin Films. *Advanced Functional Materials* **15**, 1291-1296 (2005).
98. R. Kisslinger, A. M. Askar, U. K. Thakur, S. Riddell, D. Dahunsi, Y. Zhang, S. Zeng, A. Goswami, K. Shankar, Preferentially oriented TiO₂ nanotube arrays on non-native substrates and their improved performance as electron transporting layer in halide perovskite solar cells. *Nanotechnology* **30**, 204003 (2019).
99. G. K. Mor, O. K. Varghese, M. Paulose, K. Shankar, C. A. Grimes, A review on highly ordered, vertically oriented TiO₂ nanotube arrays: Fabrication, material properties, and solar energy applications. *Solar Energy Materials and Solar Cells* **90**, 2011-2075 (2006).
100. K. Shankar, TiO₂ Nanotube Arrays: Growth and Application, in *Encyclopedia of Nanotechnology*, B. Bhushan, Ed. (Springer Netherlands, Dordrecht, 2012), pp. 2742-2755.
101. K. Zhu, T. B. Vinzant, N. R. Neale, A. J. Frank, Removing structural disorder from oriented TiO₂ nanotube arrays: Reducing the dimensionality of transport and recombination in dye-sensitized solar cells. *Nano Letters* **7**, 3739-3746 (2007).

102. R. Mohammadpour, A. I. Zad, A. Hagfeldt, G. Boschloo, Comparison of Trap-state Distribution and Carrier Transport in Nanotubular and Nanoparticulate TiO₂ Electrodes for Dye-Sensitized Solar Cells. *Chemphyschem* **11**, 2140-2145 (2010).
103. A. Mohammadpour, P. Kar, B. D. Wiltshire, A. M. Askar, K. Shankar, Electron Transport, Trapping and Recombination in Anodic TiO₂ Nanotube Arrays. *Current Nanoscience* **11**, 593-614 (2015).
104. M. Hattori, K. Noda, T. Nishi, K. Kobayashi, H. Yamada, K. Matsushige, Investigation of electrical transport in anodized single TiO₂ nanotubes. *Applied Physics Letters* **102**, (2013).
105. A. Lamberti, A. Sacco, S. Bianco, D. Manfredi, M. Armandi, M. Quaglio, E. Tresso, C. F. Pirri, An easy approach for the fabrication of TiO₂ nanotube-based transparent photoanodes for Dye-sensitized Solar Cells. *Solar Energy* **95**, 90-98 (2013).
106. J. H. Park, S. Kim, A. J. Bard, Novel carbon-doped TiO₂ nanotube arrays with high aspect ratios for efficient solar water splitting. *Nano Letters* **6**, 24-28 (2006).
107. Z. H. Zhang, L. B. Zhang, M. N. Hedhili, H. N. Zhang, P. Wang, Plasmonic Gold Nanocrystals Coupled with Photonic Crystal Seamlessly on TiO₂ Nanotube Photoelectrodes for Efficient Visible Light Photoelectrochemical Water Splitting. *Nano Letters* **13**, 14-20 (2013).
108. P. Kar, Y. Zhang, S. Farsinezhad, A. Mohammadpour, B. D. Wiltshire, H. Sharma, K. Shankar, Rutile phase n- and p-type anodic titania nanotube arrays with square-shaped pore morphologies. *Chemical Communications* **51**, 7816-7819 (2015).
109. D. Chen, H. Zhang, X. Li, J. H. Li, Biofunctional Titania Nanotubes for Visible-Light-Activated Photoelectrochemical Biosensing. *Analytical Chemistry* **82**, 2253-2261 (2010).
110. S. Farsinezhad, A. Mohammadpour, A. N. Dalrymple, J. Geisinger, P. Kar, M. J. Brett, K. Shankar, Transparent Anodic TiO₂ Nanotube Arrays on Plastic Substrates for Disposable Biosensors and Flexible Electronics. *Journal of Nanoscience and Nanotechnology* **13**, 2885-2891 (2013).

111. J. Y. Tian, Y. Li, J. J. Dong, M. J. Huang, J. S. Lu, Photoelectrochemical TiO₂ nanotube arrays biosensor for asulam determination based on in-situ generation of quantum dots. *Biosensors & Bioelectronics* **110**, 1-7 (2018).
112. M. Ni, M. K. H. Leung, D. Y. C. Leung, K. Sumathy, A review and recent developments in photocatalytic water-splitting using TiO₂ for hydrogen production. *Renewable & Sustainable Energy Reviews* **11**, 401-425 (2007).
113. N. K. Allam, M. A. El-Sayed, Photoelectrochemical Water Oxidation Characteristics of Anodically Fabricated TiO₂ Nanotube Arrays: Structural and Optical Properties. *The Journal of Physical Chemistry C* **114**, 12024-12029 (2010).
114. P. Kar, S. Farsinezhad, N. Mahdi, Y. Zhang, U. Obuekwe, H. Sharma, J. Shen, N. Semagina, K. Shankar, Enhanced CH₄ yield by photocatalytic CO₂ reduction using TiO₂ nanotube arrays grafted with Au, Ru, and ZnPd nanoparticles. *Nano Research* **9**, 3478-3493 (2016).
115. T. T. Zhang, B. Yu, D. A. Wang, F. Zhou, Molybdenum-doped and anatase/rutile mixed-phase TiO₂ nanotube photoelectrode for high photoelectrochemical performance. *Journal of Power Sources* **281**, 411-416 (2015).
116. I. J. Park, D. H. Kim, W. M. Seong, B. S. Han, G. S. Han, H. S. Jung, M. Yang, W. Fan, S. Lee, J.-K. Lee, K. S. Hong, Observation of anatase nanograins crystallizing from anodic amorphous TiO₂ nanotubes. *CrystEngComm* **17**, 7346-7353 (2015).
117. J. Villanueva-Cab, S.-R. Jang, A. F. Halverson, K. Zhu, A. J. Frank, Trap-Free Transport in Ordered and Disordered TiO₂ Nanostructures. *Nano Letters* **14**, 2305-2309 (2014).
118. S. K. Wallace, K. P. McKenna, Grain Boundary Controlled Electron Mobility in Polycrystalline Titanium Dioxide. *Advanced Materials Interfaces* **1**, 1400078 (2014).
119. C. Wehrenfennig, C. M. Palumbiny, H. J. Snaith, M. B. Johnston, L. Schmidt-Mende, L. M. Herz, Fast Charge-Carrier Trapping in TiO₂ Nanotubes. *The Journal of Physical Chemistry C* **119**, 9159-9168 (2015).

120. S. Lee, I. J. Park, D. H. Kim, W. M. Seong, D. W. Kim, G. S. Han, J. Y. Kim, H. S. Jung, K. S. Hong, Crystallographically preferred oriented TiO₂ nanotube arrays for efficient photovoltaic energy conversion. *Energy & Environmental Science* **5**, 7989-7995 (2012).
121. P. Acevedo-Pena, F. Gonzalez, G. Gonzalez, I. Gonzalez, The effect of anatase crystal orientation on the photoelectrochemical performance of anodic TiO₂ nanotubes. *Physical Chemistry Chemical Physics* **16**, 26213-26220 (2014).
122. W. M. Seong, D. H. Kim, I. J. Park, G. D. Park, K. Kang, S. Lee, K. S. Hong, Roughness of Ti Substrates for Control of the Preferred Orientation of TiO₂ Nanotube Arrays as a New Orientation Factor. *The Journal of Physical Chemistry C* **119**, 13297-13305 (2015).
123. A. John K, J. Naduvath, S. Mallick, T. Shripathi, M. Thankamoniamma, R. R. Philip, A novel cost effective fabrication technique for highly preferential oriented TiO₂ nanotubes. *Nanoscale* **7**, 20386-20390 (2015).
124. M. Rezaee, S. M. Mousavi Khoie, K. H. Liu, The role of brookite in mechanical activation of anatase-to-rutile transformation of nanocrystalline TiO₂: An XRD and Raman spectroscopy investigation. *CrystEngComm* **13**, 5055-5061 (2011).
125. H. K. Adli, T. Harada, S. Nakanishi, S. Ikeda, Effects of TiCl₄ treatment on the structural and electrochemical properties of a porous TiO₂ layer in CH₃NH₃PbI₃ perovskite solar cells. *Physical Chemistry Chemical Physics* **19**, 26898-26905 (2017).
126. G. Choe, J. Kang, I. Ryu, S. W. Song, H. M. Kim, S. Yim, Influence of the concentration of TiCl₄ solution used for post-treatment on mesoporous TiO₂ layers in hybrid lead halide perovskite solar cells. *Solar Energy* **155**, 1148-1156 (2017).
127. S.-W. Lee, K.-S. Ahn, K. Zhu, N. R. Neale, A. J. Frank, Effects of TiCl₄ Treatment of Nanoporous TiO₂ Films on Morphology, Light Harvesting, and Charge-Carrier Dynamics in Dye-Sensitized Solar Cells. *The Journal of Physical Chemistry C* **116**, 21285-21290 (2012).
128. T. N. Murakami, T. Miyadera, T. Funaki, L. Cojocar, S. Kazaoui, M. Chikamatsu, H. Segawa, Adjustment of Conduction Band Edge of Compact TiO₂ Layer in Perovskite Solar

- Cells Through TiCl_4 Treatment. *ACS Applied Materials & Interfaces* **9**, 36708-36714 (2017).
129. F. Bella, G. Griffini, J.-P. Correa-Baena, G. Saracco, M. Grätzel, A. Hagfeldt, S. Turri, C. Gerbaldi, Improving efficiency and stability of perovskite solar cells with photocurable fluoropolymers. *Science*, (2016).
130. L. D. Sun, S. Zhang, X. W. Sun, X. D. He, Effect of electric field strength on the length of anodized titania nanotube arrays. *Journal of Electroanalytical Chemistry* **637**, 6-12 (2009).
131. S. Sreekantan, K. A. Saharudin, Z. Lockman, T. W. Tzu, Fast-rate formation of TiO_2 nanotube arrays in an organic bath and their applications in photocatalysis. *Nanotechnology* **21**, (2010).
132. D. Ariosa, F. Elhordoy, E. A. Dalchiele, R. E. Marotti, C. Stari, Texture vs morphology in ZnO nano-rods: On the x-ray diffraction characterization of electrochemically grown samples. *Journal of Applied Physics* **110**, 124901 (2011).
133. S. Y. Sayed, J. M. Buriak, Epitaxial Growth of Nanostructured Gold Films on Germanium via Galvanic Displacement. *ACS Applied Materials & Interfaces* **2**, 3515-3524 (2010).
134. Z. Banyamin, P. Kelly, G. West, J. Boardman, Electrical and Optical Properties of Fluorine Doped Tin Oxide Thin Films Prepared by Magnetron Sputtering. *Coatings* **4**, 732 (2014).
135. D. Tatar, B. Düzgün, The relationship between the doping levels and some physical properties of $\text{SnO}_2\text{:F}$ thin films spray-deposited on optical glass. *Pramana* **79**, 137-150 (2012).
136. C. Soci, A. Zhang, X.-Y. Bao, H. Kim, Y. Lo, D. Wang, Nanowire Photodetectors. *Journal of Nanoscience and Nanotechnology* **10**, 1430-1449 (2010).
137. S. Emmons, K. Ashley, Minority-Carrier Sweepout in 0.09-eV HgCdTe. *Applied Physics Letters* **20**, 162-163 (1972).

138. M. Misra, D. Korakakis, H. Ng, T. Moustakas, Photoconductive detectors based on partially ordered $\text{Al}_x\text{Ga}_{1-x}\text{N}$ alloys grown by molecular beam epitaxy. *Applied Physics Letters* **74**, 2203-2205 (1999).
139. S. Thomas, K. Stefanie, P. Kristin, P. Oliver, D. Kay, F. Daniel, O. Ivan, S. Adriana, K. Ernst-Bernhard, T. Andreas, Materials Pushing the Application Limits of Wire Grid Polarizers further into the Deep Ultraviolet Spectral Range. *Advanced Optical Materials* **4**, 1780-1786 (2016).
140. K. Wang, F. Chen, G. Belev, S. Kasap, K. S. Karim, Lateral metal-semiconductor-metal photodetectors based on amorphous selenium. *Applied Physics Letters* **95**, 013505 (2009).
141. J. Zou, Q. Zhang, K. Huang, N. Marzari, Ultraviolet Photodetectors Based on Anodic TiO_2 Nanotube Arrays. *The Journal of Physical Chemistry C* **114**, 10725-10729 (2010).
142. G. Liu, N. Hoivik, X. Wang, S. Lu, K. Wang, H. Jakobsen, Photoconductive, free-standing crystallized TiO_2 nanotube membranes. *Electrochimica Acta* **93**, 80-86 (2013).
143. M. H. Zarifi, A. Mohammadpour, S. Farsinezhad, B. D. Wiltshire, M. Nosrati, A. M. Askar, M. Daneshmand, K. Shankar, Time-Resolved Microwave Photoconductivity (TRMC) Using Planar Microwave Resonators: Application to the Study of Long-Lived Charge Pairs in Photoexcited Titania Nanotube Arrays. *The Journal of Physical Chemistry C* **119**, 14358-14365 (2015).
144. M. H. Zarifi, S. Farsinezhad, M. Abdolrazzaghi, M. Daneshmand, K. Shankar, Selective microwave sensors exploiting the interaction of analytes with trap states in TiO_2 nanotube arrays. *Nanoscale* **8**, 7466-7473 (2016).
145. D. F. Rodríguez, P. M. Perillo, TiO_2 nanopores with high sensitivity to ultraviolet light. *Optical Materials* **42**, 52-55 (2015).
146. Y. Zhao, C. Z. Li, X. H. Liu, F. Go, H. L. Du, L. Y. Shi, Zn-doped TiO_2 nanoparticles with high photocatalytic activity synthesized by hydrogen-oxygen diffusion flame. *Applied Catalysis B-Environmental* **79**, 208-215 (2008).

147. Z. K. Zheng, B. B. Huang, X. D. Meng, J. P. Wang, S. Y. Wang, Z. Z. Lou, Z. Y. Wang, X. Y. Qin, X. Y. Zhang, Y. Dai, Metallic zinc-assisted synthesis of Ti^{3+} self-doped TiO_2 with tunable phase composition and visible-light photocatalytic activity. *Chemical Communications* **49**, 868-870 (2013).
148. T. T. Loan, V. H. Huong, V. T. Tham, N. N. Long, Effect of zinc doping on the bandgap and photoluminescence of Zn^{2+} -doped TiO_2 nanowires. *Physica B-Condensed Matter* **532**, 210-215 (2018).
149. R. Long, N. J. English, Tailoring the electronic structure of TiO_2 by cation codoping from hybrid density functional theory calculations. *Physical Review B* **83**, (2011).
150. M.-C. Wu, S.-H. Chan, M.-H. Jao, W.-F. Su, Enhanced short-circuit current density of perovskite solar cells using Zn-doped TiO_2 as electron transport layer. *Solar Energy Materials and Solar Cells* **157**, 447-453 (2016).
151. F. Huang, Q. Li, G. J. Thorogood, Y.-B. Cheng, R. A. Caruso, Zn-doped TiO_2 electrodes in dye-sensitized solar cells for enhanced photocurrent. *Journal of Materials Chemistry* **22**, 17128-17132 (2012).
152. H. Sierra-Uribe, J. E. Carrera-Crespo, A. Cano, E. M. Córdoba-Tuta, I. González, P. Acevedo-Peña, Electroreduction as a viable strategy to obtain TiO_2 nanotube films with preferred anatase crystal orientation and its impact on photoelectrochemical performance. *Journal of Solid State Electrochemistry* **22**, 1881-1891 (2018).
153. R. Kisslinger, S. Riddell, S. Savela, P. Kar, U. K. Thakur, S. Zeng, K. Shankar, Transparent nanoporous P-type NiO films grown directly on non-native substrates by anodization. *Journal of Materials Science: Materials in Electronics* **30**, 11327-11335 (2019).
154. S. Rühle, A. Y. Anderson, H.-N. Barad, B. Kupfer, Y. Bouhadana, E. Rosh-Hodesh, A. Zaban, All-Oxide Photovoltaics. *The Journal of Physical Chemistry Letters* **3**, 3755-3764 (2012).

155. S. Martha, P. Chandra Sahoo, K. M. Parida, An overview on visible light responsive metal oxide based photocatalysts for hydrogen energy production. *RSC Advances* **5**, 61535-61553 (2015).
156. M. Grundmann, H. Frenzel, A. Lajn, M. Lorenz, F. Schein, H. v. Wenckstern, Transparent semiconducting oxides: materials and devices. *physica status solidi (a)* **207**, 1437-1449 (2010).
157. A. Dey, Semiconductor metal oxide gas sensors: A review. *Materials Science and Engineering: B* **229**, 206-217 (2018).
158. S. Lee, S. Jeon, R. Chaji, A. Nathan, Transparent Semiconducting Oxide Technology for Touch Free Interactive Flexible Displays. *Proceedings of the IEEE* **103**, 644-664 (2015).
159. Z. Wang, P. K. Nayak, J. A. Caraveo-Frescas, H. N. Alshareef, Recent Developments in p-Type Oxide Semiconductor Materials and Devices. *Advanced Materials* **28**, 3831-3892 (2016).
160. P. Kar, K. Shankar, Biodiagnostics Using Oriented and Aligned Inorganic Semiconductor Nanotubes and Nanowires. *Journal of Nanoscience and Nanotechnology* **13**, 4473-4496 (2013).
161. P. M. Rao, L. Cai, C. Liu, I. S. Cho, C. H. Lee, J. M. Weisse, P. Yang, X. Zheng, Simultaneously Efficient Light Absorption and Charge Separation in WO₃/BiVO₄ Core/Shell Nanowire Photoanode for Photoelectrochemical Water Oxidation. *Nano Letters* **14**, 1099-1105 (2014).
162. D. Sarkar, S. Ishchuk, D. H. Taffa, N. Kaynan, B. A. Berke, T. Bendikov, R. Yerushalmi, Oxygen-Deficient Titania with Adjustable Band Positions and Defects; Molecular Layer Deposition of Hybrid Organic–Inorganic Thin Films as Precursors for Enhanced Photocatalysis. *The Journal of Physical Chemistry C* **120**, 3853-3862 (2016).
163. Y. Wang, L. Zhu, T. Wang, Y. Hu, Z. Deng, Q. Cui, Z. Lou, Y. Hou, F. Teng, Sensitive, fast, stable, and broadband polymer photodetector with introducing TiO₂ nanocrystal trap states. *Organic Electronics* **59**, 63-68 (2018).

164. G. Katwal, M. Paulose, I. A. Rusakova, J. E. Martinez, O. K. Varghese, Rapid Growth of Zinc Oxide Nanotube–Nanowire Hybrid Architectures and Their Use in Breast Cancer-Related Volatile Organics Detection. *Nano Letters* **16**, 3014-3021 (2016).
165. M. I. A. Umar, F. Y. Naumar, M. M. Salleh, A. A. Umar, Hydrothermally grown of well-aligned ZnO NRs: dependence of alignment ordering upon precursor concentration. *Journal of Materials Science: Materials in Electronics* **29**, 6892-6897 (2018).
166. D.-D. Qin, C.-L. Tao, S.-i. In, Z.-Y. Yang, T. E. Mallouk, N. Bao, C. A. Grimes, Facile Solvothermal Method for Fabricating Arrays of Vertically Oriented α -Fe₂O₃ Nanowires and Their Application in Photoelectrochemical Water Oxidation. *Energy & Fuels* **25**, 5257-5263 (2011).
167. T. J. LaTempa, X. Feng, M. Paulose, C. A. Grimes, Temperature-Dependent Growth of Self-Assembled Hematite (α -Fe₂O₃) Nanotube Arrays: Rapid Electrochemical Synthesis and Photoelectrochemical Properties. *The Journal of Physical Chemistry C* **113**, 16293-16298 (2009).
168. N. K. Allam, X. J. Feng, C. A. Grimes, Self-Assembled Fabrication of Vertically Oriented Ta₂O₅ Nanotube Arrays, and Membranes Thereof, by One-Step Tantalum Anodization. *Chemistry of Materials* **20**, 6477-6481 (2008).
169. J.-S. Baik, G. Yun, M. Balamurugan, S. K. Lee, J.-H. Kim, K.-S. Ahn, S. H. Kang, Hydrogen Treated Niobium Oxide Nanotube Arrays for Photoelectrochemical Water Oxidation. *Journal of the Electrochemical Society* **163**, H1165-H1170 (2016).
170. J. He, Y. Hu, Z. Wang, W. Lu, S. Yang, G. Wu, Y. Wang, S. Wang, H. Gu, J. Wang, Hydrothermal growth and optical properties of Nb₂O₅ nanorod arrays. *Journal of Materials Chemistry C* **2**, 8185-8190 (2014).
171. C. W. Lai, S. B. Abd Hamid, S. Sreekantan, A Novel Solar Driven Photocatalyst: Well-Aligned Anodic WO₃ Nanotubes. *International Journal of Photoenergy* **2013**, 745301 (2013).

172. J.-H. Ha, P. Muralidharan, D. K. Kim, Hydrothermal synthesis and characterization of self-assembled h-WO₃ nanowires/nanorods using EDTA salts. *Journal of Alloys and Compounds* **475**, 446-451 (2009).
173. C. E. Castillo, M. Gennari, T. Stoll, J. Fortage, A. Deronzier, M. N. Collomb, M. Sandroni, F. Légalité, E. Blart, Y. Pellegrin, C. Delacote, M. Boujtita, F. Odobel, P. Rannou, S. Sadki, Visible Light-Driven Electron Transfer from a Dye-Sensitized p-Type NiO Photocathode to a Molecular Catalyst in Solution: Toward NiO-Based Photoelectrochemical Devices for Solar Hydrogen Production. *The Journal of Physical Chemistry C* **119**, 5806-5818 (2015).
174. Z. Zhu, Y. Bai, T. Zhang, Z. Liu, X. Long, Z. Wei, Z. Wang, L. Zhang, J. Wang, F. Yan, S. Yang, High-Performance Hole-Extraction Layer of Sol-Gel-Processed NiO Nanocrystals for Inverted Planar Perovskite Solar Cells. *Angewandte Chemie International Edition* **53**, 12571-12575 (2014).
175. S. R. Nalage, M. A. Chougule, S. Sen, P. B. Joshi, V. B. Patil, Sol-gel synthesis of nickel oxide thin films and their characterization. *Thin Solid Films* **520**, 4835-4840 (2012).
176. B. R. Cruz-Ortiz, M. A. Garcia-Lobato, E. R. Larios-Durán, E. M. Múzquiz-Ramos, J. C. Ballesteros-Pacheco, Potentiostatic electrodeposition of nanostructured NiO thin films for their application as electrocatalyst. *Journal of Electroanalytical Chemistry* **772**, 38-45 (2016).
177. A. Sápi, A. Varga, G. F. Samu, D. Dobó, K. L. Juhász, B. Takács, E. Varga, Á. Kukovecz, Z. Kónya, C. Janáky, Photoelectrochemistry by Design: Tailoring the Nanoscale Structure of Pt/NiO Composites Leads to Enhanced Photoelectrochemical Hydrogen Evolution Performance. *The Journal of Physical Chemistry C* **121**, 12148-12158 (2017).
178. J. Bandara, K. Shankar, J. Basham, H. Wietasch, M. Paulose, O. K. Varghese, C. A. Grimes, M. Thelakkat, Integration of TiO₂ nanotube arrays into solid-state dye-sensitized solar cells. *Eur. Phys. J. Appl. Phys.* **53**, 20601 (2011).

179. K. N. Chappanda, Y. R. Smith, M. Misra, S. K. Mohanty, Site-specific and patterned growth of TiO₂ nanotube arrays from e-beam evaporated thin titanium film on Si wafer. *Nanotechnology* **23**, 385601 (2012).
180. K. N. Chappanda, Y. R. Smith, S. K. Mohanty, L. W. Rieth, P. Tathireddy, M. Misra, Growth and characterization of TiO₂ nanotubes from sputtered Ti film on Si substrate. *Nanoscale research letters* **7**, 388-388 (2012).
181. V. Galstyan, A. Vomiero, E. Comini, G. Faglia, G. Sberveglieri, TiO₂ nanotubular and nanoporous arrays by electrochemical anodization on different substrates. *RSC Advances* **1**, 1038-1044 (2011).
182. V. Galstyan, A. Vomiero, I. Concina, A. Braga, M. Brisotto, E. Bontempi, G. Faglia, G. Sberveglieri, Vertically Aligned TiO₂ Nanotubes on Plastic Substrates for Flexible Solar Cells. *Small* **7**, 2437-2442 (2011).
183. S. L. Lim, Y. Liu, J. Li, E.-T. Kang, C. K. Ong, Transparent titania nanotubes of micrometer length prepared by anodization of titanium thin film deposited on ITO. *Applied Surface Science* **257**, 6612-6617 (2011).
184. Y. Tang, J. Tao, Z. Dong, J. T. Oh, Z. Chen, The formation of micrometer-long TiO₂ nanotube arrays by anodization of titanium film on conducting glass substrate. *Advances in Natural Sciences: Nanoscience and Nanotechnology* **2**, 045002 (2011).
185. H. Wang, H. Li, J. Wang, J. Wu, High aspect-ratio transparent highly ordered titanium dioxide nanotube arrays and their performance in dye sensitized solar cells. *Materials Letters* **80**, 99-102 (2012).
186. J. Weickert, C. Palumbiny, M. Nedelcu, T. Bein, L. Schmidt-Mende, Controlled Growth of TiO₂ Nanotubes on Conducting Glass. *Chemistry of Materials* **23**, 155-162 (2011).
187. A. Mohammadpour, K. Shankar, Anodic TiO₂ nanotube arrays with optical wavelength-sized apertures. *Journal of Materials Chemistry* **20**, 8474-8477 (2010).

188. Y.-N. Kim, H.-G. Shin, J.-K. Song, D.-H. Cho, H.-S. Lee, Y.-G. Jung, Thermal Degradation Behavior of Indium Tin Oxide Thin Films Deposited by Radio Frequency Magnetron Sputtering. *Journal of Materials Research* **20**, 1574-1579 (2005).
189. C. Lavoie, F. M. d'Heurle, C. Detavernier, C. Cabral, Towards implementation of a nickel silicide process for CMOS technologies. *Microelectronic Engineering* **70**, 144-157 (2003).
190. S. M. Jung, J. H. Kim, C. J. Park, M. W. Shin, Nickel mono-silicide formation using a photo-thermal process assisted by ultra-violet laser. *Materials Science in Semiconductor Processing* **75**, 263-268 (2018).
191. F. A. Geenen, E. Solano, J. Jordan-Sweet, C. Lavoie, C. Mocuta, C. Detavernier, The influence of alloying on the phase formation sequence of ultra-thin nickel silicide films and on the inheritance of texture. *Journal of Applied Physics* **123**, 185302 (2018).
192. S. A. Yousif, J. M. Abass, Structural, Morphological and Optical Characterization of SnO₂:F Thin Films Prepared by Chemical Spray Pyrolysis. *International Letters of Chemistry, Physics and Astronomy* **18**, 90-102 (2013).
193. M. D. Irwin, D. B. Buchholz, A. W. Hains, R. P. H. Chang, T. J. Marks, Type semiconducting nickel oxide as an efficiency-enhancing anode interfacial layer in polymer bulk-heterojunction solar cells. *Proceedings of the National Academy of Sciences* **105**, 2783 (2008).
194. N. M. Hosny, Synthesis, characterization and optical band gap of NiO nanoparticles derived from anthranilic acid precursors via a thermal decomposition route. *Polyhedron* **30**, 470-476 (2011).
195. N. Park, K. Sun, Z. Sun, Y. Jing, D. Wang, High efficiency NiO/ZnO heterojunction UV photodiode by sol-gel processing. *Journal of Materials Chemistry C* **1**, 7333-7338 (2013).
196. X. Sun, G. Wang, J.-Y. Hwang, J. Lian, Porous nickel oxide nano-sheets for high performance pseudocapacitance materials. *Journal of Materials Chemistry* **21**, 16581-16588 (2011).

197. K. V. Rao, A. Smakula, Dielectric Properties of Cobalt Oxide, Nickel Oxide, and Their Mixed Crystals. *Journal of Applied Physics* **36**, 2031-2038 (1965).
198. G. Natu, P. Hasin, Z. Huang, Z. Ji, M. He, Y. Wu, Valence Band-Edge Engineering of Nickel Oxide Nanoparticles via Cobalt Doping for Application in p-Type Dye-Sensitized Solar Cells. *ACS Applied Materials & Interfaces* **4**, 5922-5929 (2012).
199. H.-L. Chen, Y.-S. Yang, Effect of crystallographic orientations on electrical properties of sputter-deposited nickel oxide thin films. *Thin Solid Films* **516**, 5590-5596 (2008).
200. C. Chaneliere, J. L. Autran, R. A. B. Devine, B. Balland, Tantalum pentoxide (Ta₂O₅) thin films for advanced dielectric applications. *Materials Science and Engineering: R: Reports* **22**, 269-322 (1998).
201. L. Young, Anodization Constants for Tantalum. *Journal of the Electrochemical Society* **124**, 528 (1977).
202. S.-J. Joo, J. H. Choi, S. J. Kim, S.-C. Kim, Pd/Ta₂O₅/SiC Schottky-diode hydrogen sensors formed by using rapid thermal oxidation of Ta thin films. *Journal of the Korean Physical Society* **63**, 1794-1798 (2013).
203. J.-Y. Kim, M. C. Nielsen, E. J. Rymaszewski, T.-M. Lu, Electrical characteristics of thin Ta₂O₅ films deposited by reactive pulsed direct-current magnetron sputtering. *Journal of Applied Physics* **87**, 1448-1452 (2000).
204. J. Aarik, K. Kukli, A. Aidla, L. Pung, Mechanisms of suboxide growth and etching in atomic layer deposition of tantalum oxide from TaCl₅ and H₂O. *Applied Surface Science* **103**, 331-341 (1996).
205. T. J. Rehg, J. A. Ochoa-Tapia, A. Knoesen, B. G. Higgins, Solgel derived tantalum pentoxide films as ultraviolet antireflective coatings for silicon. *Applied Optics* **28**, 5215-5221 (1989).

206. A. M. Md Jani, D. Losic, N. H. Voelcker, Nanoporous anodic aluminium oxide: Advances in surface engineering and emerging applications. *Progress in Materials Science* **58**, 636-704 (2013).
207. K. Xie, M. Guo, H. Huang, Y. Liu, Fabrication of iron oxide nanotube arrays by electrochemical anodization. *Corrosion Science* **88**, 66-75 (2014).
208. P. G. Sheasby, S. Wernick, R. Pinner, *Surface treatment and finishing of aluminum and its alloys*. (ASM International/Finishing Publications, Ltd., Metals Park, OH, United States, 1987).
209. T. B. Tripp, The Effect of Phosphorus Doping on the Direct Current Leakage of Anodic Oxide Films on Tantalum. *Journal of the Electrochemical Society* **137**, 2528 (1990).
210. B. O'Regan, M. Grätzel, A low-cost, high-efficiency solar cell based on dye-sensitized colloidal TiO₂ films. *Nature* **353**, 737-740 (1991).
211. J. E. Barton, C. L. Stender, P. Li, T. W. Odom, Structural control of anodized tantalum oxide nanotubes. *Journal of Materials Chemistry* **19**, (2009).
212. H. El-Sayed, S. Singh, P. Kruse, Formation of Dimpled Tantalum Surfaces from Electropolishing. *Journal of the Electrochemical Society* **154**, (2007).
213. H. A. El-Sayed, V. I. Birss, Versatile fabrication of self-assembled metallic nanoparticle arrays. *Journal of Materials Chemistry* **21**, (2011).
214. H. A. El-Sayed, H. B. Campbell, V. I. Birss, Electrochemical applications of a Au nanoparticle array fabricated using highly ordered dimpled Ta templates. *Electrochimica Acta* **112**, 845-852 (2013).
215. H. El-Sayed, S. Singh, M. T. Greiner, P. Kruse, Formation of highly ordered arrays of dimples on tantalum at the nanoscale. *Nano Letters* **6**, 2995-2999 (2006).
216. S. Singh, W. R. T. Barden, P. Kruse, Nanopatterning of Transition Metal Surfaces via Electrochemical Dimple Array Formation. *ACS Nano* **2**, 2453-2464 (2008).

217. I. Horcas, R. Fernández, J. M. Gómez-Rodríguez, J. Colchero, J. Gómez-Herrero, A. M. Baro, WSXM: A software for scanning probe microscopy and a tool for nanotechnology. *Review of Scientific Instruments* **78**, 013705 (2007).
218. L. V. Rodríguez-de Marcos, J. I. Larruquert, J. A. Méndez, J. A. Aznárez, Self-consistent optical constants of SiO₂ and Ta₂O₅ films. *Optical Materials Express* **6**, 3622-3637 (2016).
219. C. Xu, W. Gao, Pilling-Bedworth ratio for oxidation of alloys. *Material Research Innovations* **3**, 231-235 (2000).
220. S. J. Garcia-Vergara, P. Skeldon, G. E. Thompson, H. Habazaki, A flow model of porous anodic film growth on aluminium. *Electrochimica Acta* **52**, 681-687 (2006).
221. J. Hirvonen, A. G. Revesz, T. D. Kirkendall, Rutherford backscattering investigation of thermally oxidized tantalum on silicon. *Thin Solid Films* **33**, 315-322 (1976).
222. S. Gates-Rector, T. Blanton, The Powder Diffraction File: a quality materials characterization database. *Powder Diffraction* **34**, 352-360 (2019).
223. V. A. Shvets, V. S. Aliev, D. V. Gritsenko, S. S. Shaimeev, E. V. Fedosenko, S. V. Rykhliiski, V. V. Atuchin, V. A. Gritsenko, V. M. Tapilin, H. Wong, Electronic structure and charge transport properties of amorphous Ta₂O₅ films. *Journal of Non-Crystalline Solids* **354**, 3025-3033 (2008).
224. T. J. Bright, J. I. Watjen, Z. M. Zhang, C. Muratore, A. A. Voevodin, D. I. Koukis, D. B. Tanner, D. J. Arenas, Infrared optical properties of amorphous and nanocrystalline Ta₂O₅ thin films. *Journal of Applied Physics* **114**, 083515 (2013).
225. M. Vos, P. L. Grande, S. K. Nandi, D. K. Venkatachalam, R. G. Elliman, A high-energy electron scattering study of the electronic structure and elemental composition of O-implanted Ta films used for the fabrication of memristor devices. *Journal of Applied Physics* **114**, 073508 (2013).

226. H.-S. Tsai, T.-Y. Yang, M.-T. Chang, L.-J. Chou, Y.-L. Chueh, Ta₂O₅ Nanowires, Nanotubes, and Ta₂O₅/SiO₂ Core-Shelled Structures: From Growth to Material Characterization. *Journal of Nanomaterials* **2014**, 914847 (2014).
227. G. Sethi, M. Olszta, L. Jing, J. Sloppy, M. W. Horn, E. C. Dickey, M. T. Lanagan, in *2007 Annual Report - Conference on Electrical Insulation and Dielectric Phenomena*. (2007), pp. 815-818.
228. T. V. Perevalov, A. V. Shaposhnikov, Ab initio simulation of the electronic structure of Ta₂O₅ crystal modifications. *Journal of Experimental and Theoretical Physics* **116**, 995-1001 (2013).
229. P. K. Jain, K. S. Lee, I. H. El-Sayed, M. A. El-Sayed, Calculated Absorption and Scattering Properties of Gold Nanoparticles of Different Size, Shape, and Composition: Applications in Biological Imaging and Biomedicine. *The Journal of Physical Chemistry B* **110**, 7238-7248 (2006).
230. Y. Luo, X. Liu, X. Tang, Y. Luo, Q. Zeng, X. Deng, S. Ding, Y. Sun, Gold nanoparticles embedded in Ta₂O₅/Ta₃N₅ as active visible-light plasmonic photocatalysts for solar hydrogen evolution. *Journal of Materials Chemistry A* **2**, 14927-14939 (2014).
231. V. Canpean, M. Iosin, S. Astilean, Disentangling SERS signals from two molecular species: A new evidence for the production of p,p'-dimercaptoazobenzene by catalytic coupling reaction of p-aminothiophenol on metallic nanostructures. *Chemical Physics Letters* **500**, 277-282 (2010).
232. Y. Fang, Y. Li, H. Xu, M. Sun, Ascertaining p,p'-Dimercaptoazobenzene Produced from p-Aminothiophenol by Selective Catalytic Coupling Reaction on Silver Nanoparticles. *Langmuir* **26**, 7737-7746 (2010).
233. Y.-F. Huang, M. Zhang, L.-B. Zhao, J.-M. Feng, D.-Y. Wu, B. Ren, Z.-Q. Tian, Activation of Oxygen on Gold and Silver Nanoparticles Assisted by Surface Plasmon Resonances. *Angewandte Chemie International Edition* **53**, 2353-2357 (2014).

234. W. Lin, Y. Cao, P. Wang, M. Sun, Unified Treatment for Plasmon–Exciton Co-driven Reduction and Oxidation Reactions. *Langmuir* **33**, 12102-12107 (2017).
235. Q. Zhang, H. Wang, Mechanistic Insights on Plasmon-Driven Photocatalytic Oxidative Coupling of Thiophenol Derivatives: Evidence for Steady-State Photoactivated Oxygen. *The Journal of Physical Chemistry C* **122**, 5686-5697 (2018).
236. M. L. Brongersma, N. J. Halas, P. Nordlander, Plasmon-induced hot carrier science and technology. *Nature Nanotechnology* **10**, 25-34 (2015).
237. Y. Shiraishi, N. Yasumoto, J. Imai, H. Sakamoto, S. Tanaka, S. Ichikawa, B. Ohtani, T. Hirai, Quantum tunneling injection of hot electrons in Au/TiO₂ plasmonic photocatalysts. *Nanoscale* **9**, 8349-8361 (2017).